Diffusion Tensor Imaging Biomarkers of Brain Development and Disease

by

Evan Darcy Cozzens Calabrese

Department of Biomedical Engineering
Duke University

Date:_____

Approved:

_____
G. Allan Johnson, Supervisor

_____
Chunlei Liu

_____
James Provenzale

_____
Gregg Trahey

_____
Charles Watson

Dissertation submitted in partial fulfillment of the requirements for the degree of Doctor of Philosophy in the Department of Biomedical Engineering in the Graduate School of Duke University

2014

ABSTRACT

Diffusion Tensor Imaging Biomarkers of Brain Development and Disease

by

Evan Darcy Cozzens Calabrese

Department of Biomedical Engineering
Duke University

Date:_____

Approved:

_____
G. Allan Johnson, Supervisor

_____
Chunlei Liu

_____
James Provenzale

_____
Gregg Trahey

_____
Charles Watson

An abstract of a dissertation submitted in partial fulfillment of the requirements for the degree of Doctor of Philosophy in the Department of Biomedical Engineering in the Graduate School of Duke University

2014

Abstract

Understanding the structure of the brain has been a major goal of neuroscience research over the past century, driven in part by the understanding that brain structure closely follows function. Normative brain maps, or atlases, can be used to understand normal brain structure, and to identify structural differences resulting from disease. Recently, diffusion tensor magnetic resonance imaging has emerged as a powerful tool for brain atlasing; however, its utility is hindered by image resolution and signal limitations. These limitations can be overcome by imaging fixed ex-vivo specimens stained with MRI contrast agents, a technique known as diffusion tensor magnetic resonance histology (DT-MRH). DT-MRH represents a unique, quantitative tool for mapping the brain with unprecedented structural detail. This technique has engendered a new generation of 3D, digital brain atlases, capable of representing complex dynamic processes such as neurodevelopment. This dissertation explores the use of DT-MRH for quantitative brain atlasing in an animal model and initial work in the human brain.

Chapter 1 describes the advantages of the DT-MRH technique, and the motivations for generating a quantitative atlas of rat postnatal neurodevelopment. The second chapter covers optimization of the DT-MRH hardware and pulse sequence design for imaging the developing rat brain. Chapter 3 details the acquisition and curation of rat neurodevelopmental atlas data. Chapter 4 describes the creation and implementation of an ontology-based segmentation

scheme for tracking changes in the developing brain. Chapters 5 and 6 pertain to analyses of volumetric changes and diffusion tensor parameter changes throughout rat postnatal neurodevelopment, respectively. Together, the first six chapters demonstrate many of the unique and scientifically valuable features of DT-MRH brain atlases in a popular animal model.

The final two chapters are concerned with translating the DT-MRH technique for use in human and non-human primate brain atlasing. Chapter 7 explores the validity of assumptions imposed by DT-MRH in the primate brain. Specifically, it analyzes computer models and experimental data to determine the extent to which intravoxel diffusion complexity exists in the rhesus macaque brain, a close model for the human brain. Finally, Chapter 8 presents conclusions and future directions for DT-MRH brain atlasing, and includes initial work in creating DT-MRH atlases of the human brain. In conclusion, this work demonstrates the utility of a DT-MRH brain atlasing with an atlas of rat postnatal neurodevelopment, and lays the foundation for creating a DT-MRH atlas of the human brain.

Table of Contents

List of Tables

List of Figures

Acknowledgments

The work presented in this dissertation was performed at the Duke Center for In Vivo Microscopy (CIVM), an NIH/NIBIB Biomedical Technology Resource Center (P41 EB015897). Stipend and tuition support was provided by the Duke Medical Scientist Training Program NIH T32 training grant (T32 GM007171) and the Summerfield Foundation. I would like to give special thanks to several people at the CIVM who made this work possible including Gary Cofer, Yi Qi, Alexandra Badea, Lucy Upchurch, James Cook, Lawrence Hedlund, John Nouls, Tawynna Gordon, Sally Gewalt, Sally Zimney, Matt Sherrier, John Lee, David Lee, and Byung Seok Kwon. I would also like to thank several collaborators from outside the CIVM including Charles Watson, George Paxinos, Erika Gyengesi, James Provenzale, Chunlei Liu, Steven Chen, Theodore Pierce, Joseph Long, Peter Wei, and Dalun Leong. I thank the Duke Department of Biomedical Engineering and my dissertation committee: Chunlei Liu, James Provenzale, Gregg Trahey, and Charles Watson. A very special thanks goes to my dissertation advisor G. Allan Johnson who both inspired this work and made it possible. Finally, I would like to thank my parents Christine Cozzens and Ronald Calabrese for inspiring me to pursue a doctoral degree and supporting me throughout my life.

1. Introduction and Background

1.1. Brain atlasing

Despite centuries of anatomic research, the brain remains arguably the least understood organ in the human body. The remarkable anatomic complexity of the brain manifests at both the macrostructural and microstructural (i.e. cellular) level. Mapping the architecture of the brain has been a major goal of neuroscience since its origins, driven in part by the realization that structure is intimately associated with function. This association has been further strengthened by the relatively recent realization that subtle structural changes in the brain are a feature of a wide range of neurological and psychiatric diseases. Normative brain maps, or atlases, have proven invaluable both in understanding normal brain function, and in identifying and localizing subtle changes resulting from disease states. The concept of a brain atlas has been around for centuries, and its form has evolved along with advances in brain visualization techniques. From illustration, to photography, to light microscopy, imaging techniques have always been the driving force behind the newest generation of brain atlases. As technology improves, so to does the quality of information provided by brain atlases, and their potential for revealing the structural basis of brain function and disease. Exploring and evaluating the role of new imaging techniques for brain atlasing is essential for advancing the field and improving our understanding of the brain.

1.2. Magnetic resonance histology

Since its inception in the 1970's in the laboratories of Dr. Paul Lauterbur and Dr. Peter Mansfield, magnetic resonance imaging (MRI) has revolutionized both clinical and research radiology, particularly with regard to neurological examinations. MRI provides uniquely flexible soft tissue contrast, which is ideal for creating detailed brain maps. MRI also has very high theoretical resolution, and it was recognized very early on that MRI could be used to study microscopic features; the closing line of Dr. Lauterbur's seminal paper on MRI states, "Zeumatographic [MRI] techniques should find many useful applications in studies of the internal structures, states, and compositions of microscopic objects" (Lauterbur, 1973). Unfortunately, after over 40 years of advances, microscopic MRI remains impractical in-vivo in humans due to signal and scan-time limitations. Many of these limitations can be overcome by imaging fixed ex-vivo specimens—a technique known as magnetic resonance histology (MRH) (Johnson et al., 1993).

MRH is a microscopic MR imaging technique that is, in many ways, complementary with conventional light microscopy based histology. Although typically lower resolution than conventional histology (10's of microns vs ~1 micron), MRH has several important advantages as a brain mapping technology (Johnson et al., 2002b). MRH is non-destructive and non-distorting to the tissue being imaged. Brain specimens can be imaged in-situ in the skull to preserve native spatial relationships, and repeat studies, including subsequent conventional histology, can be performed on the same specimen. MRH is three-

dimensional (3D), isotropic, and inherently digital. 3D image volumes can be rotated and re-sliced in any arbitrary plane without significant loss in resolution. This allows precise alignment of several different image volumes to create a single population average. Finally, MRH provides a variety of unique proton contrasts, each of which reveals different anatomical features. Multiple different contrasts can be elaborated from the exact same section of tissue simply by changing acquisition parameters. Further, many proton contrasts are quantitative in nature, allowing statistical comparisons between specimens. The ability to generate unique, quantitative, soft tissue image contrast is perhaps the most important aspect of MRH, and is the fundamental basis of the work presented here.

1.3. Diffusion tensor magnetic resonance histology

One quantitative MRI contrast of particular interest is diffusion contrast, which probes the Brownian motion of water molecules in tissue. Diffusion MRI can be used to measure tissue diffusion in any arbitrary direction. If diffusion is measured in six or more non-colinear directions, the data can be fit to a rank-2 covariance tensor, which allows estimation of both the magnitude and direction of greatest diffusion in each pixel. This powerful imaging technique, referred to as diffusion tensor imaging (DTI), yields a variety of quantitative derived images, each with unique contrast based on water diffusion properties. DTI-derived contrasts are unlike any contrasts available in conventional histology because they reflect actual physical phenomena occurring in the tissue during imaging.

DTI is particularly useful in neurological studies because water diffusivity is significantly higher along axonal tracts than perpendicular to them, thus white matter diffusion is highly directional or *anisotropic*. By following pathways of high diffusion anisotropy, it is possible to create 3D maps of white matter connections in the brain, a technique known as diffusion tractography. Over the past two decades, DTI and tractography have been used to map tissue microstructure in the human brain, in both health and disease states. Unfortunately, adapting DTI for high-resolution brain atlasing is difficult because it has inherently low signal-to-noise ratio (SNR) and long scan times.

The combination of DTI with MRH, henceforth referred to as DT-MRH, allows extremely high-resolution and high-SNR diffusion imaging through tissue staining to enhance MR signal, high-sensitivity radiofrequency coils, and long scan times that would be impractical in-vivo. DT-MRH combines the best aspects of both techniques: the high-resolution, 3D, digital nature of MRH and the quantitative diffusion-based contrasts and tractography of DTI. Several features of DT-MRH make it particularly appealing for brain atlasing. For example, the high spatial resolution and multiple DTI derived image contrasts allow detailed brain substructure delineation; quantitative diffusion contrast provides local metrics of tissue microstructural features; and tractography offers a 3D view of white matter architecture.

1.4. Diffusion tensor magnetic resonance histology brain atlases

To date, DT-MRH has been most extensively used for small animal brain imaging, particularly rats and mice. Not only are such specimens technically easier to scan with DT-MRH, they are also among the most widely used model systems in brain research. Rodent brain atlases have proven invaluable in localizing lesions is disease models, and helping to distinguish normal anatomy from pathology. Notable examples of DT-MRH brain atlases exist for the mouse (Jiang and Johnson, 2011) and the rat (Veraart et al., 2011; Johnson et al., 2012). These atlases showcase several innovative features of DT-MRH brain atlases including: 1) the ability to get accurate 3D structure volumes, 2) the use of quantitative DTI-derived contrast to infer microstructural features, and 3) the capacity to explore population variability using non-linear image registration. Perhaps more importantly, these atlases are representative of a gradual evolution from qualitative, histology-based, printed volumes to quantitative, searchable, digital entities. While DT-MRH brain atlases certainly have not replaced conventional histology atlases, they do provide different, and complementary information.

DT-MRH atlases of adult rodent brains, while innovative, have only scratched the surface of what this technology can accomplish. One of the most interesting aspects of diffusion contrast is that it changes with the underlying tissue microstructural changes that occur during brain development and disease states. The ability to track these microstructural changes, along with local

changes in brain morphometry, make DT-MRH atlases of brain development particularly attractive.

1.5. Atlases of mammalian brain development

Virtually all mammals undergo significant postnatal brain growth and differentiation (Clancy et al., 2007), yet surprisingly little is known about this period of neurodevelopment. Rodent models, and in particular the rat, represent a valuable tool for studying disorders of mammalian brain development. Importantly, both mice and rats undergo a relatively large portion of neurodevelopment in the postnatal period, including the majority of cerebellar growth and differentiation. In humans, similar developmental processes typically occur in the third trimester of gestation (Tiemeier et al., 2010; White and Sillitoe, 2012). For this reason, rodent postnatal neurodevelopment can serve as a model for human neurodevelopment from late gestation through adolescence. A number of perinatal vascular insults (perinatal hypoxia, cerebral palsy), toxic insults (fetal alcohol exposure, antidepressant exposure), and traumatic insults (shaken baby syndrome) are known to produce similar white matter injury in the perinatal period in both humans and rodent models (Bonnier et al., 2004; Wang et al., 2009; O'Leary-Moore et al., 2011; Simpson et al., 2011). In order to effectively characterize aberrant postnatal neurodevelopment resulting from such insults, one needs both a well-defined “normal” model and a set of quantitative tools for assessing differences between exposed subjects and controls.

Developmental brain atlases can provide unique insight into the normal course of neurodevelopment, and allow researchers to distinguish normative developmental change from pathologic changes. The importance of a developmental atlas of the rat brain has been recognized for some time, and several notable examples have been published. Two well known histology atlases are the Sherwood and Timiras 1970 “A Stereotaxic Atlas of the Developing Rat Brain” (Sherwood and Timiras, 1970) and the Ashwell and Paxinos 2008 “Atlas of the Developing Rat Nervous System” (Ashwell and Paxinos, 2008). These atlases are primarily focused on prenatal development. The Sherwood-Timiras atlas includes three postnatal time points (p10, p21, and p39), and the Ashwell-Paxinos atlas only one (p0). More recently, Ramachandra and Subramanian published their 2011 “Atlas of the Neonatal Rat Brain” (Ramachandra and Subramanian, 2011), which features three postnatal time points (p1, p7, and p14). In contrast to the relative wealth of conventional histology atlases, to our knowledge there is currently no comparable DT-MRH-based atlas of the developing rat brain. There are, however, at least three examples in the mouse including previous work from our laboratory (Zhang et al., 2005; Petiet et al., 2008; Chuang et al., 2011). These atlases further highlight the need for a complementary DT-MRH atlas of the developing rat brain with an emphasis on developing a quantitative database of normal neurodevelopment.

1.6. DT-MRH biomarkers of brain structure and development

The first six chapters of this dissertation outline the acquisition, analysis and use of a DT-MRH atlas of rat postnatal neurodevelopment. The specific aim of this project was to create a quantitative archive and database of normative postnatal neurodevelopment that can be easily and quantitatively compared with neurodevelopmental disease models. Even in the absence of relevant disease models, the atlas provides unique insight into the normal trajectory of postnatal neurodevelopment, which may be useful for identifying key developmental periods for different brain regions. Here we describe several important insights into postnatal neurodevelopment gleaned from this unique dataset, including a detailed analysis of both volumetric changes, and changes in quantitative diffusion tensor parameters.

The synthesis of the DT-MRH atlas of rat postnatal neurodevelopment took place in several phases, each represented by a chapter of this manuscript. The first (current) chapter describes the motivation for and aims of this project. The second chapter covers optimization of the DT-MRH hardware and pulse sequence design for imaging the developing rat brain. Chapter 3 details the acquisition and curation of atlas data. Chapter 4 describes the creation and implementation of an ontology-based segmentation scheme for tracking changes in the developing brain. Chapters 5 and 6 pertain to analyses of volumetric changes and diffusion tensor parameter changes throughout postnatal neurodevelopment, respectively. Together, the first six chapters demonstrate

many of the unique and scientifically valuable features of DT-MRH brain atlases in a popular animal model.

One of the major goals of this dissertation was to explore the use and practicality of DT-MRH as a new brain mapping technology. Although the majority of the work presented here pertains to small animals, DT-MRH is in theory scalable to larger, more complex brains, including the human brain. A DT-MRH atlas of the human brain would be an invaluable tool for the neuroscience community, particularly in the era of the human connectome project. Unfortunately, diffusion contrast can be misleading in complex brains because multiple different diffusion pathways may be present in the same voxel. The seventh chapter of this dissertation describes both computer simulations and empirical testing of the degree of intravoxel diffusion inhomogeneity and its effect on diffusion tractography in the primate brain. This chapter represents initial work in translating DT-MRH brain atlasing to more complex mammalian brains including humans and non-human primates. Finally, preliminary work in the human brain is presented in Chapter 8, along with a discussion of future goals in DT-MRH brain atlasing.

2. Optimization of DT-MRH for the rat brain

2.1. Introduction and background

2.1.1. Diffusion weighted MRI and diffusion tensor imaging

In MRI, diffusion weighting is achieved by spatially encoding water protons with phase using a magnetic gradient pulse, waiting some period of time referred to as the "mixing period" and then attempting to reverse the spatially encoded phase gradient with a second gradient pulse. Any water protons that change position due to diffusion during the mixing period will not be rephased, resulting in a signal loss that is related to the apparent diffusion coefficient (ADC) of the tissue through the following exponential relationship:

$$S_D = Se^{-b \bullet ADC}$$

where S_D is the diffusion weighted signal, S is the non-diffusion weighted signal, and b is the b-value—a constant that describes the degree of diffusion weighting imposed by the MRI pulse sequence. The b-value depends on the magnetic gradient pulse shape, amplitude, duration (δ) and spacing (Δ) and has units of s/mm^2, the reciprocal of diffusion coefficient units. If b-value is known, then the ADC of tissue along a given gradient direction can be extracted from a single diffusion weighted image and a single non-diffusion weighted image by rearranging the previous equation. If diffusion is measured along a number of different gradient directions (six at the minimum) it is possible to estimate a single, rank-2 tensor that describes the diffusion magnitude and primary diffusion

direction within each image voxel. This technique, referred to as diffusion tensor imaging (DTI) allows quantitative exploration of sub-voxel diffusion barriers. High-resolution, high-SNR DTI is difficult to achieve because 1) a minimum of six diffusion weighted images and one non-diffusion weighted image must be acquired, 2) diffusion weighting inherently reduces image signal, and 3) diffusion weighted pulse sequences are demanding of MRI hardware because of the large magnetic gradients required for diffusion encoding.

2.1.2. Barriers to high-spatial resolution MRI

One of the most important aspects of any brain atlas is its spatial resolution. High spatial resolution allows identification of small brain structures, precise measurements of structure volume, and minimizes error cause by partial volume averaging. In theory, MRI resolution is limited only by magnetic gradient strength; however, in practice, resolution is limited by signal-to-noise ratio (SNR). For subjects of a given size a number of factors contribute to an approximately exponential loss in SNR as resolution increases. First, holding all other parameters constant, increasing the acquisition matrix size to increase resolution results in a longer readout gradient duration, and consequently, a longer echo time (TE). TE affects MRI signal through the following exponential relationship:

$$S = S_0 e^{-TE / T2}$$

where S is the measured signal amplitude, S_0 is the maximum possible signal, and T2 is the spin-spin relaxation time constant. The effect of TE becomes much

more prominent when TE is long relative T2. Voxel volume is also a factor, and has a direct, linear relationship with SNR such that if resolution is doubled in all three spatial dimensions, voxel volume, and therefore signal, decreases by a factor of eight. Increasing matrix size also increases total signal acquisition time, which increases SNR slightly, but this effect is far outweighed by signal reduction factors.

SNR is also affected by a number of other factors including, but not limited to, pulse sequence design, radiofrequency (RF) coil sensitivity, magnetic field strength (B_0), magnetic field homogeneity, and image reconstruction. In order to maximize spatial resolution for the atlas of rat postnatal neurodevelopment, it was necessary to maximize SNR by optimizing every modifiable factor. We have attempted to increase SNR and resolution by optimizing diffusion pulse sequence design, specimen preparation and RF coil design.

2.2. Methods and Results

2.2.1. Diffusion pulse sequence design

Proper pulse sequence selection is essential for accurate diffusion tensor data and high quality images. The diffusion imaging experiments presented in this work were acquired with a 3D, Cartesian, spin-echo pulse sequence. This pulse sequence was chosen for several reasons; 1) 3D RF excitation is faster than slice-selective excitation, allowing shorter echo times to be achieved; 2) 3D pulse sequences provide increased signal by measuring from the entire specimen at once; 3) Cartesian spin-echo pulse sequences are much less prone

to image distortions and artifacts than non-Cartesian and/or gradient-echo pulse sequences; and 4) reconstruction of Cartesian MRI data is straightforward, even for large the large data matrices that are common in DT-MRH.

Diffusion weighting was achieved with a pair of unipolar, half-sine diffusion gradient waveforms on either side of the 180-degree RF pulse. Half-sine diffusion gradients produce significantly lower b-values than comparable trapezoidal gradients; however they are much less prone to eddy current-induced image distortions owing to their more gradual rise in amplitude. In short, half-sine diffusion gradients were chosen to reduce image artifacts at the cost of reduced diffusion-weighting relative to gradient amplitude and duration.

Diffusion tensor data for the adult rat brain were collected on a 7 Tesla small animal imaging system equipped with 650 mT/m gradient coils using diffusion-sensitization along each of six non-colinear diffusion gradient vectors: [1, 1, 0], [1, 0, 1], [0, 1, 1], [-1, 1, 0], [1, 0, -1], and [0, -1, 1]. This gradient scheme allows robust estimation of the diffusion tensor with the minimum number of measurement directions and provides faster diffusion preparation by employing two orthogonal diffusion gradients at the same time, resulting in a $\sqrt{2}$ increase in the net diffusion-sensitization vector amplitude (Jiang and Johnson, 2011). Using this gradient scheme we were able to achieve a b-value of b = 1492 s/mm^2 with an echo time of 16.2 ms in the adult rat brain. We attempted to minimize repetition time (TR) to allow faster imaging; however, gradient duty-cycle limitations dictated a minimum TR of 100 ms. The final pulse sequence had TR = 100 ms, TE = 16.2 ms, diffusion-gradient width δ = 3 ms, diffusion-gradient

separation Δ = 8.5 ms, and diffusion-gradient amplitude = 600 mT/m. Figure 1 shows a standard MR pulse sequence diagram of the diffusion sequence used throughout this dissertation.

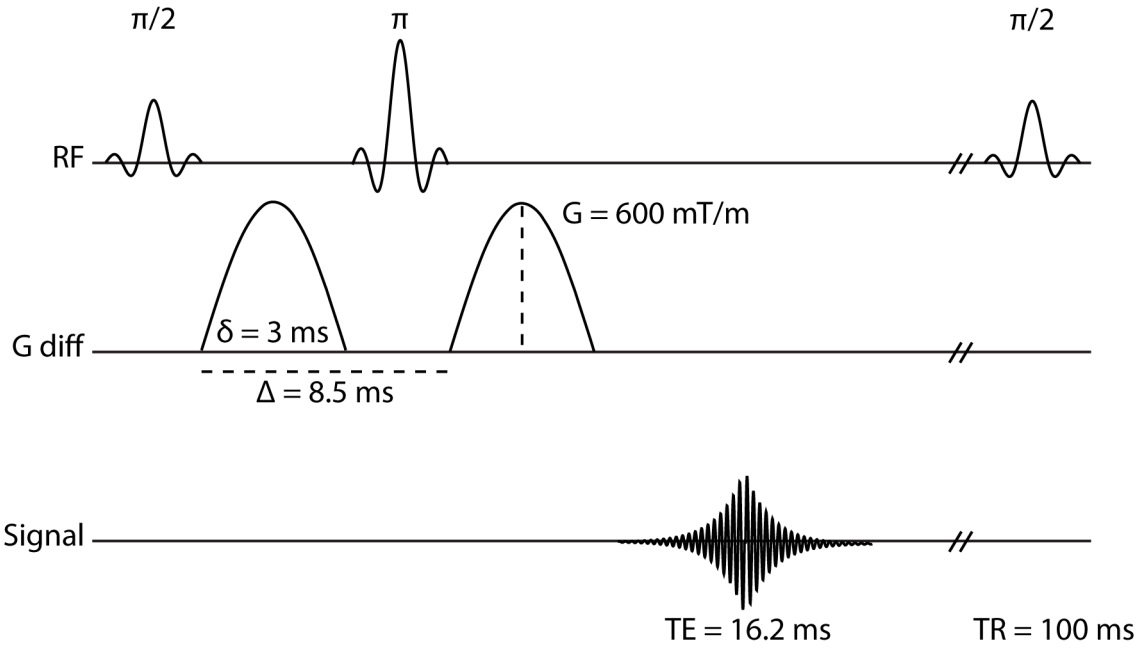

Figure 1 – A pulse sequence diagram of the diffusion sequence used throughout this dissertation. RF = radiofrequency; G diff = diffusion gradient; signal = measured MR signal.

2.2.2. Optimization of H1 relaxivity for DT-MRH of the rat brain

One of the major advantages of imaging ex-vivo specimens is that magnetic relaxivity can be altered using MRI contrast agents to an extent that would be impossible or impractical in-vivo. Fine control of tissue T1 and T2 relaxation allows rapid image acquisition (short TR) without sacrificing signal. The short repetition period is essential for collecting the large data matrices required for high-resolution MRH. The simplest way to shorten acquisition time is to reduce TR; however this approach also reduces signal by preventing complete

T1 relaxation between 90-degree pulses. For a spin echo pulse sequence, steady state signal is described by the following equation:

$$S = M_0(1 - e^{-TR/T1})(e^{-TE/T2})$$

where S is the measured signal and M_0 is the total magnetization of the subject, proportional to proton density and magnetic field strength, B_0. The first exponential term reveals the effects of shortening TR relative to T1 relaxation time. For example, the average T1 relaxation time of the unstained rat brain is 1-2 seconds, which would lead to a 90-95% reduction of signal from T1 effects alone if a TR of 100 ms was used.

By introducing gadolinium-based contrast agents into the brain parenchyma, it is possible to dramatically reduce T1 relaxation time. Using the above equation it is possible to calculate the optimal T1 and T2 relaxation times for a given TR and TE. Given the values from our pulse sequence (TR = 100 ms and TE = 16.2 ms) and assuming that T2 is roughly 1/4 of T1 (which is empirically true in the rat brain), we find that the optimal T1/T2 combination is T1 = 107 ms and T2 = 27 ms. Previous work in our laboratory has shown that such relaxivity values are achievable at 7 Tesla by soaking the fixed brain in a 5 mM solution of gadolinium chelate in phosphate buffered saline for 5-7 days prior to imaging (Johnson et al., 2002b). We confirmed these results and ensured consistent relaxivity reductions at various time points during rat postnatal neurodevelopment. A representative T1 map from a gadolinium stained postnatal

day 12 rat brain is shown in Figure 2. The average T1 relaxation time across the entire brain was approximately 110 ms.

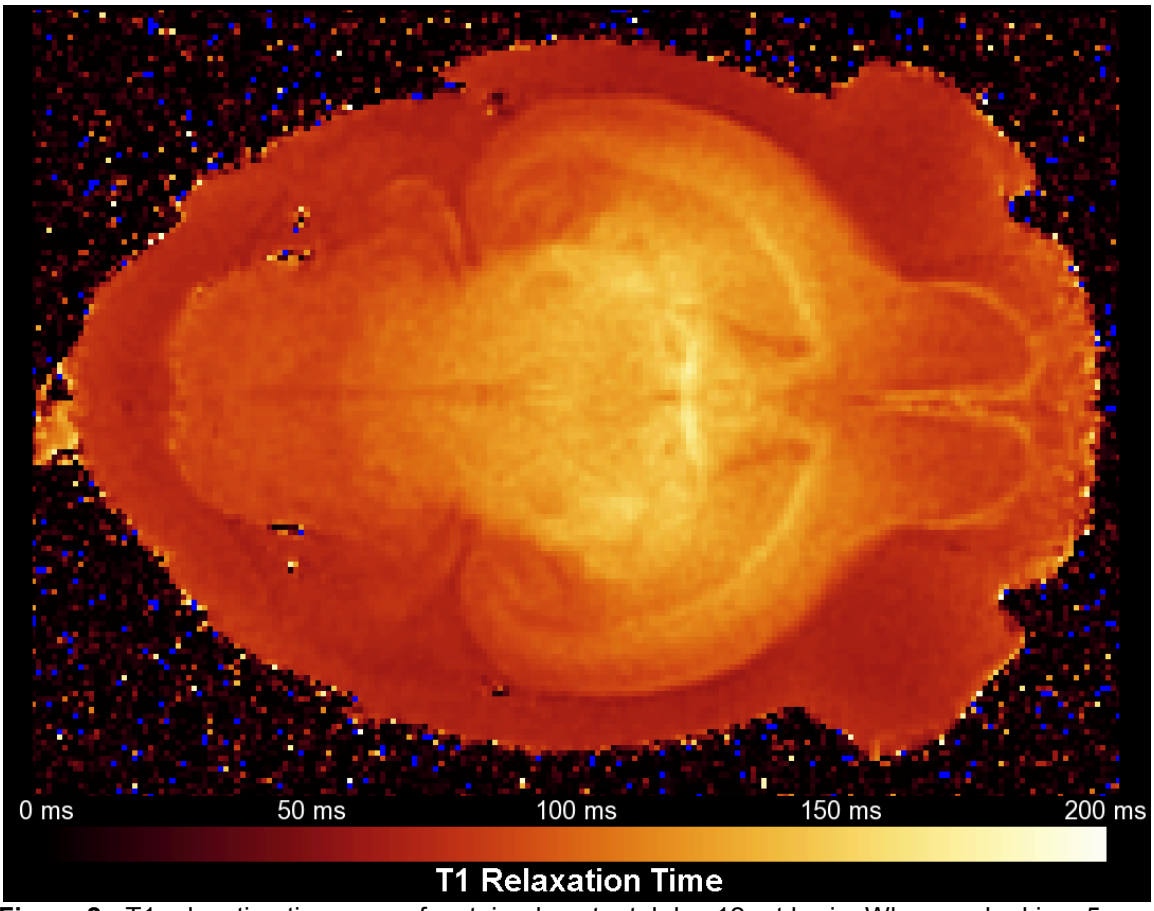

Figure 2 - T1 relaxation time map of a stained postnatal day 12 rat brain. When soaked in a 5 mM solution of gadolinium chelate for 5-7 days, the T1 of the brain parenchyma is approximately 80-130 ms.

2.2.3. High-sensitivity RF coil design

Careful RF coil design is essential for achieving high-resolution, high-SNR images with MRH. Improper RF coil engineering can be a major source of signal loss and can cause image artifacts due to inhomogeneous coil sensitivity across the field of view. Single-loop solenoid RF coils are simple, reliable, and can produce very homogeneous RF transmit fields (Hoult and Richards, 1976). The

main reason that solenoid RF coils are not widely used is that they must be positioned perpendicular to the main magnetic field, B_0, which is often impractical for in-vivo imaging, but not for MRH. The sensitivity of a solenoid RF coil depends on a number of factors, the most important of which are surface conductivity and internal volume (Hoult and Richards, 1976; Hoult and Lauterbur, 1979; Edelstein et al., 1986). The higher the surface conductivity the more current (and therefore signal) is produced for a given spin excitation. Internal volume affects RF coil sensitivity in a number of ways. First, thermal noise contamination is integrated across the entire internal volume of the RF coil, so larger internal volumes will have more thermal noise and lower SNR. Second, the closer the spin excitation is to the surface of the coil the higher the resulting signal will be. Finally, the conduction path length of the solenoid is directly related to resistive losses, and shorter path lengths (i.e. smaller coils) lead to improved SNR.

For the above reasons, we attempted to make the smallest internal volume RF coils possible to accommodate the different stages of rat postnatal neurodevelopment. We also attempted to use the highest conductivity material available that would remain stable throughout the time and temperature changes that are typical for a high-resolution MRH acquisition. We chose 99.9% pure silver because of its relatively low reactivity, high conductivity, and low thermal expansion coefficient. Coils were constructed from 50 μm thick rolled silver sheets. We fabricated three different sized coils to cover the range of brain sizes included in our study, each with a different internal diameter (ID): 20 mm ID for

birth–postnatal day 8, 25 mm ID for postnatal day 12–24, and 30 mm ID for postnatal day 40–80. In each case, the length of the solenoid was chosen to be approximately 1.5 times the internal diameter to produce a homogeneous RF transmit field. All three RF coils are shown in Figure 3 with a ruler for scale comparison.

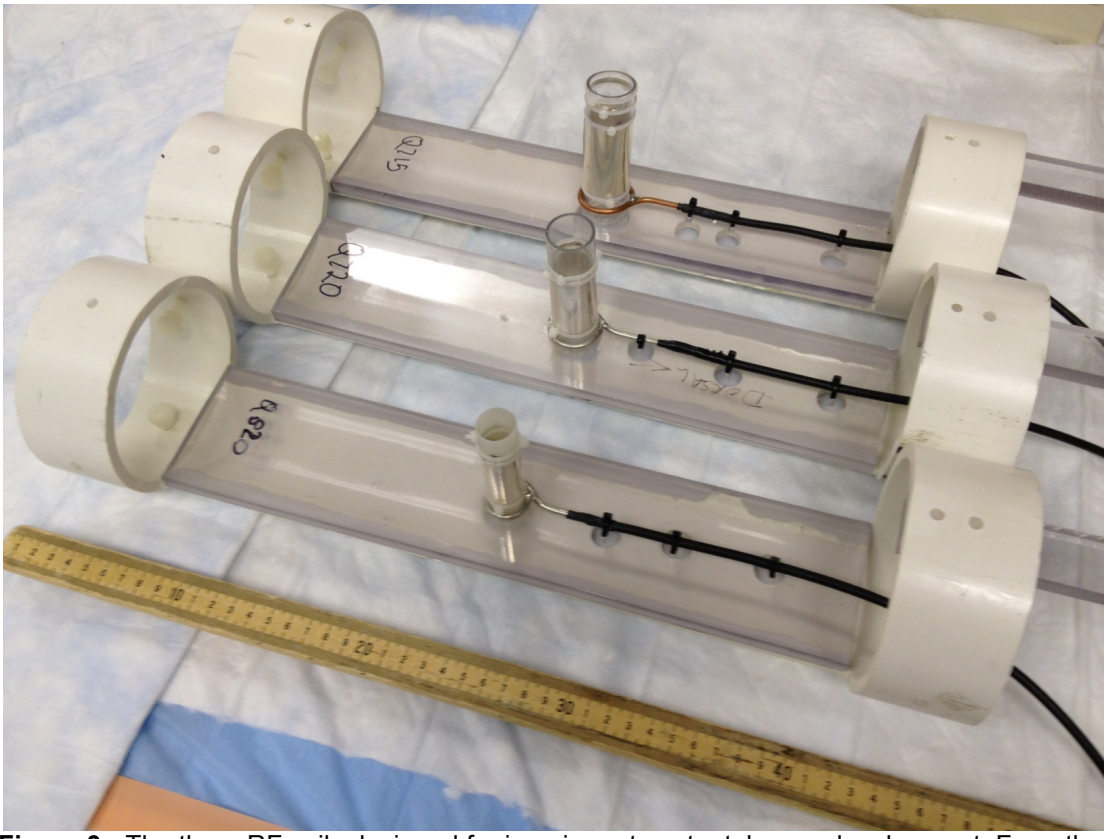

Figure 3 - The three RF coils designed for imaging rat postnatal neurodevelopment. From the top of the figure: 30 mm ID coil, 25 mm ID coil, 20 mm ID coil, centimeter ruler.

We quantified the sensitivity of each RF coil by measuring its Q-factor—a parameter that describes how under-damped an RF resonator is by comparing its bandwidth relative to its center frequency. In general, the higher the Q-factor, the more sensitive the RF coil and the narrower its bandwidth. In theory, image SNR scales with the square root of the RF coil Q-factor. The Q-factor is

numerically equivalent to the resonant frequency divided by the -3 dB bandwidth (Edelstein et al., 1986). A typical copper MRH coil for a 7T imaging system has a Q-factor for 400-500. The silver coils designed for this study had Q-factors of 820, 720, and 715 for the 20 mm ID, 25 mm ID, and 30 mm ID coils respectively.

2.3. Discussion

Together, the pulse sequence design, specimen preparation, and RF coil modifications described above dramatically improved SNR, and therefore resolution, of DT-MRH experiments on the developing rat brain. With a minimum acceptable SNR threshold of 30, these modifications allow 50 μm isotropic diffusion-weighted images a b=1492 mm^2/s and 25 μm isotropic gradient recalled echo anatomic images. These represent the highest-resolution DT-MRH images of the whole rat brain ever reported. The increased spatial accuracy provided by these high-resolution images combined with the quantitative measurements of diffusion afforded by DT-MRH have extraordinary potential to reveal the complex spatiotemporal changes that occur during postnatal neurodevelopment in unprecedented detail. Further, the approaches detailed in this chapter have widespread applicability to MRH experiments in other MRI systems, in other species, and in other organ systems with only minor modifications. For example, the rolled silver RF coil technology is already being used for mouse brain, kidney, and heart MRH in our laboratory. These improvements add to the long list of technologies that make DT-MRH both possible and practical in a large variety of model systems.

3. Acquisition of DT-MRH data throughout rat postnatal neurodevelopment

The work presented in this chapter was published in two different articles in NeuroImage, one in 2012 (Johnson et al., 2012) and one in 2013 (Calabrese et al., 2013).

3.1. Introduction and Background

Here, we present the first MRH-based atlas of the developing rat brain. Our atlas incorporates the best features of preceding MRH-based atlases, and introduces several new features designed to increase its utility as a quantitative database for neurodevelopmental research. The atlas includes both DT-MRH and conventional anatomic MRH data at the highest spatial resolution yet reported for the whole rat brain (50 μm isotropic and 25 μm isotropic respectively). These image voxels are 8,000-64,000 times smaller than routine clinical image voxels. The atlas comprehensively covers postnatal neurodevelopment with nine postnatal time points chosen to accurately sample the full scope of postnatal volume changes in the rat brain. Each time point comprises data from five different specimens and includes eight distinct image contrasts, five of which are quantitative in nature. Population averages have been created for every image contrast at each time point to allow enhanced visualization and voxelwise analyses of variation.

3.2. Methods

3.2.1. Experimental animals

All experiments and procedures were done with the approval of the Duke University Institutional Animal Care and Use Committee. To ensure accurate sampling of postnatal brain growth, we selected nine time points temporally spaced to allow a fixed percentage increase in brain volume between samples based on previously published rat brain growth curves. The nine time points selected for the atlas were p0, p2, p4, p8, p12, p18, p24, p40, and p80 (where “p” indicates postnatal day). Five male, Wistar rats were selected for imaging at each time point. All animals were from litters of 10-12 pups (average = 11) and had a body weight within one standard deviation of mean weight for age based on the growth curve provided by the supplier (*Charles River Wistar Rat Page*, 2013).

3.2.2. Specimen preparation

Animals were perfusion-fixed using the active staining technique (Johnson et al., 2002b). Perfusion fixation was achieved using a 10% solution of Neutral Buffered Formalin (NBF) containing 10% (50 mM) Gadoteridol. After perfusion fixation, rat heads were removed and immersed in 10% NBF for 24 hours. Finally, fixed rat heads were transferred to a 0.1 M solution of Phosphate Buffered Saline containing 1% (5 mM) Gadoteridol at 4° C for 5-7 days. Prior to imaging, specimens were placed in custom-made, MRI-compatible tubes and immersed in fomblin liquid fluorocarbon for susceptibility matching and to prevent

specimen dehydration. All imaging experiments were performed with the brain in the neurocranium to preserve tissue integrity and native spatial relationships.

3.2.3. Image acquisition

Imaging was performed on a 7 Tesla small animal MRI system (Magnex Scientific, Yarnton, Oxford, UK) equipped with 650 mT/m Resonance Research gradient coils (Resonance Research, Inc., Billerica, MA, USA), and controlled with a General Electric Signa console (GE Medical Systems, Milwaukee, WI, USA). RF transmission and reception was achieved using a series of custom solenoid coils ranging from 15 mm diameter × 30 mm long to 30 mm diameter × 50 mm long. T2*-weighted gradient recalled echo (GRE) images were acquired using a 3D sequence (TR = 50 ms, TE = 8.3 ms, NEX = 2, α=60°). The acquisition matrix ranged from 1024 × 512 × 512 to 1600 × 800 × 800 and the field of view (FOV) ranged from 25.6 × 12.8 × 12.8 mm to 40 × 20 × 20 mm. Matrix size was chosen so that the Nyquist isotropic spatial resolution was 25 μm in all cases.

Diffusion-weighted images were acquired using a spin-echo pulse sequence (TR = 100 ms, TE = 16.2 ms, NEX = 1). Diffusion preparation was accomplished using a modified Tanner-Stejskal diffusion-encoding scheme (Stejskal and Tanner, 1965) with a pair of unipolar, half-sine diffusion gradient waveforms (width δ = 3 ms, separation Δ = 8.5 ms, gradient amplitude = 600 mT/m). One b0 image and 6 high b-value images (b=1492 s/mm^2) were acquired with diffusion sensitization along each of six non-colinear diffusion gradient

vectors: [1, 1, 0], [1, 0, 1], [0, 1, 1], [-1, 1, 0], [1, 0, -1], and [0, -1, 1]. In this paper, the b0 image is referred to as “T2-weighted” because the long TR and TE of the acquisition relative to the T1 and T2 of the specimen, respectively, result in strong T2-weighting. The acquisition matrix ranged from 512 × 256 × 256 to 800 × 400 × 400 and FOV ranged from 25.6 × 12.8 × 12.8 mm to 40 × 20 × 20 mm. The Nyquist isotropic spatial resolution was 50 μm for all diffusion-weighted images. All images were derived from fully sampled k-space data with no zero-filling.

3.2.4. Diffusion tensor image processing

Diffusion data were processed with a custom image-processing pipeline comprised of freely available software packages including Perl (http://www.perl.org), ANTs (http://www.picsl.upenn.edu/ANTS/), and Diffusion Toolkit (http://www.trackvis.org). This automated pipeline was created to ensure that all data were processed in the same way, and to reduce the potential for user error. First, diffusion-weighted image volumes were spatially normalized to the b0 volume using the ANTs rigid registration to correct for the linear portion of eddy current distortions. Next, diffusion tensor estimation, and calculation of tensor-derived data sets were performed using Diffusion Toolkit. Finally, data were organized into a consistent file architecture and archived in NIfTI format (http://nifti.nimh.nih.gov) in an on-site Oracle database (Johnson et al., 2007).

3.2.5. Image registration and averaging

Inter-specimen registration of MR data was accomplished with the ANTs software package (Avants et al., 2008; 2011). Skull-stripped (Badea et al., 2007b) GRE and DWI images from each set of specimens (5 per time point) were aligned using an affine registration, followed by an iterative, viscous fluid model, non-linear registration. We employed a Minimum Deformation Template (MDT) strategy, which uses pairwise, non-linear image registrations to construct an average template requiring the minimum amount of deformation from each of the starting points (Kochunov et al., 2001). The similarity metric used for registration was cross-correlation computed for a kernel radius of 4 voxels. We used a multi-resolution scheme, and did a maximum of 4000 iterations at a down-sampling factor of three, 4000 iterations at a down-sampling factor of two, and 250 iterations at full resolution. We used the greedy symmetric normalization (SyN) model with a gradient step of 0.5 and a Gaussian regularization with $\sigma = 3$ for the similarity gradient, and $\sigma = 1$ for the deformation field. The algorithm converged at each step of the registration, usually with fewer than 500 iterations. The resultant transformations were applied directly to scalar images to create population averages.

3.2.6. Tensor averaging and tractography

To create population average tensor volumes we used a log-Euclidean transformation strategy (Arsigny et al., 2006). In short, the transformation is applied to the matrix logarithm of the tensor, and then the matrix exponent of the

result is taken to create the transformed tensor. FACT tractography (Mori et al., 1999) was performed on each individual and each average tensor volume using a fractional anisotropy threshold of 0.25 and an angle threshold of 45 degrees.

3.2.7. Alignment of image data to histologic atlases

We chose to align our data to conventional histology atlases for two reasons. First, we wanted a reliable method to identify different brain regions and ensure that borders visible on MRI corresponded with true cytological borders; second, we wanted to incorporate our work in to the large body of existing neuroanatomical research on the rat brain. By doing so, we hope to facilitate intermodal research in future studies on rat neuroanatomy. MRH data were aligned towards two conventional histology atlases—the p80 data were aligned to the Paxinos and Watson adult rat atlas (Paxinos and Watson, 2007), and the p0 data were aligned to the Ashwell and Paxinos p0 rat atlas (Ashwell and Paxinos, 2008). The isotropic MR data were manually reoriented to match the coronal sectioning plans outlined in the introduction section of the two atlases. We then manually compared at least six coronal MR planes (three rostral and three caudal) with spatially unique structures near both the dorsal and ventral surfaces of the brain. Based on the observed error, we then reoriented the original MR data to more closely match the histology atlas and, once again, compared six coronal MR planes. We proceeded in this fashion until we could no longer decrease error by reorienting the MR data. MR data for time points other than p0 and p80 were automatically oriented using a rigid affine registration.

Early time point data (i.e. p2, p4, p8, and p12) were registered to the aligned p0 data, while late time point data (i.e. p18, p24, and p40) were registered to the aligned p80 data.

3.3. Results

3.3.1. Atlas orientation

Figure 4 illustrates the orientation scheme for the atlas. Late time point data (i.e. p18 and older) were oriented to be consistent with the Paxinos and Watson adult rat atlas (column A) (Paxinos and Watson, 2007), while early time point data (i.e. p12 and younger) were oriented to be consistent with the Ashwell and Paxions neonatal rat atlas (column B) (Ashwell and Paxinos, 2008). The sectioning diagram from the respective histology atlas is included at the top of each column for reference.

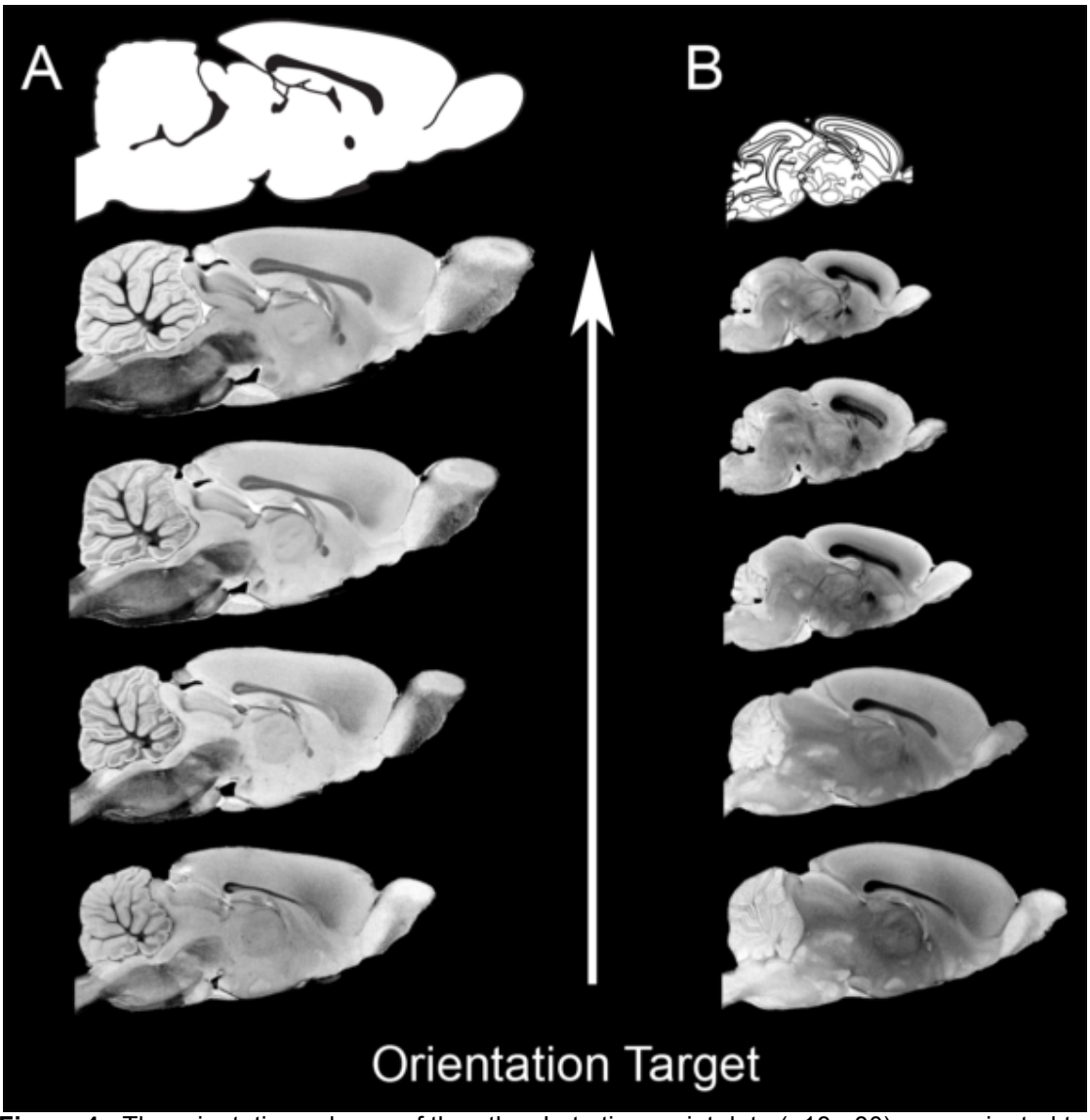

Figure 4 - The orientation scheme of the atlas. Late time point data (p18-p80) were oriented to the Paxinos and Watson adult rat brain atlas (Column A). Early time point data (p0-p12) were oriented to the Ashwell and Paxinos p0 rat brain atlas. The sectioning diagrams from the respective histology atlases are shown at the top of each column.

3.3.2. Alignment of p0 image data to the Ashwell and Paxinos histology atlas

As described in the Methods section, the p0 MRH volumes were aligned to the p0 images in the Ashwell and Paxinos (2008) histology atlas using iterative manual rotation followed by comparisons of six coronal planes. An example of a coronal comparison is presented in Figure 5. In the dorsal portion of Figure 5, the

letter A marks the rostral-most crossing of the ventral hippocampal commissure (vhc), which is not present in adjacent histology sections. B denotes the posterior limb of the anterior commissure (acp), which makes its first contact with the external capsule (ec) in this section. Rostral to this plane, the acp and ec are not in contact with each other and caudally they cannot be distinguished as two separate structures. Finally, C marks the rostral-most crossing of the anterior commissure (ac), which has a distinctive oval shape across the midline that is not present in more rostral sections. The Ashwell and Paxinos atlas does not provide rostral/caudal coordinates, so we could not directly compare histologic coordinates to MR coordinates. However, the histology sectioning interval was 200 μm, so we can compare inter-slice distance on MR and histologic sections as a metric for alignment of the two datasets. These data are presented in Table 1. The mean discrepancy between MR coordinates and histologic coordinates was 1.06 mm, which is comparable to similar attempts at aligning MRI volumes with histology (Johnson et al., 2012).

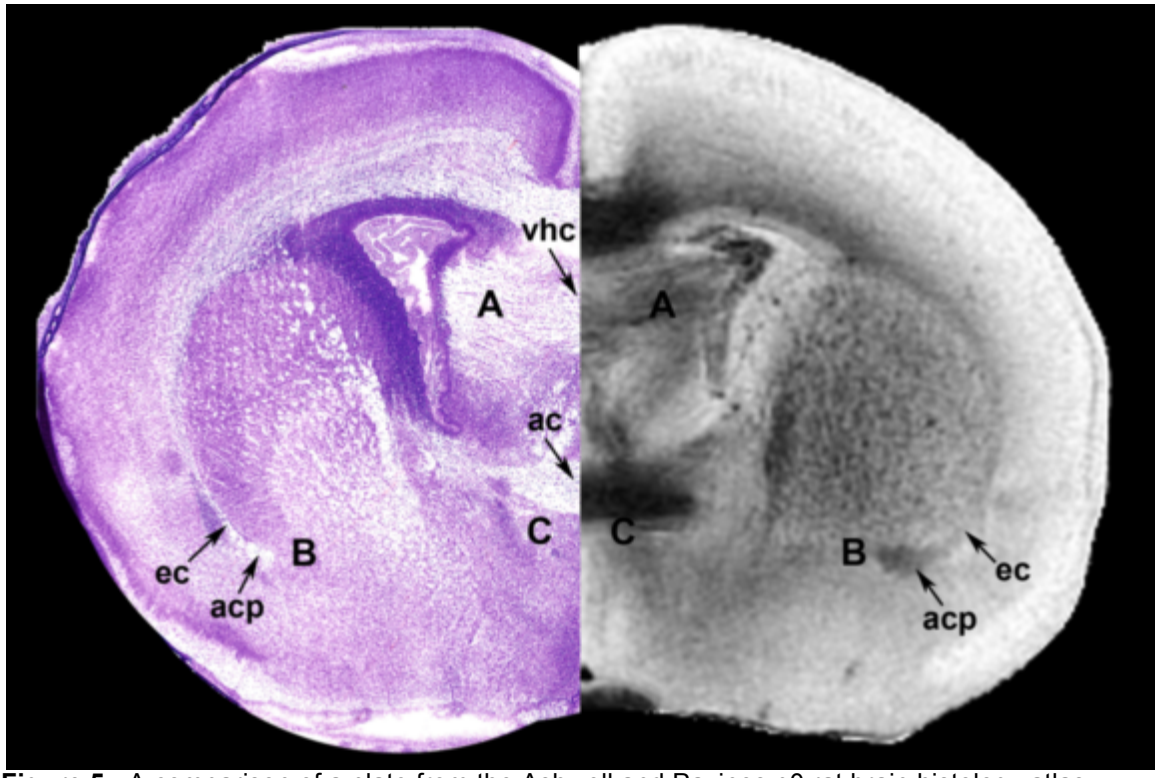

Figure 5 - A comparison of a plate from the Ashwell and Paxinos p0 rat brain histology atlas (Ashwell and Paxinos, 2008) (left) with the oriented p0 GRE data (right). The displayed section is at the level of the caudal crossing of the anterior commissure. Letter A marks the ventral hippocampal commissure (vhc). B marks the intersection of the posterior limb of the anterior commissure (acp) with the external capsule (ec). C marks the caudal extent of the crossing of the anterior commissure.

Table 1 - Comparison of interstice distance between corresponding coronal planes in the p0 rat brain as measured by MRI and the Ashwell and Paxinos p0 rat histology atlas (Ashwell and Paxinos, 2008) .

Histology Plate #s	MR Slice #s	Histology Interslice Dist. (mm)	MR Interslice Dist. (mm)	Discrepancy (mm)
217-228	536-485	2.2	1.275	0.925
228-235	485-442	1.4	1.075	0.325
235-245	442-403	2	0.975	1.025
245-251	403-381	1.2	0.55	0.65
251-279	381-251	5.6	3.25	2.35
Mean Discrepancy (mm)				**1.06**

3.3.3. Alignment of p80 image data to the Paxinos and Watson histology atlas

To ensure that the adult (p80) MR data sets were oriented as closely as possible to that of the Paxinos and Watson atlas, we identified landmarks in a series of coronal slices and compared their rostrocaudal position with the same structures pictured in the Paxinos and Watson atlas. The comparisons are shown in Table 2. The mean discrepancy in 21 comparisons was 0.27 mm, which is within the range of discrepancy that exists when landmarks in the Paxinos and Watson atlas were compared in different planes. The alignment of the MRH and Paxinos and Watson atlas can be most easily appreciated in Figure 6, which shows MR slices (left) adjacent to histology slices from the Paxinos and Watson atlas (right) with relevant anatomic landmarks showing alignment accuracy.

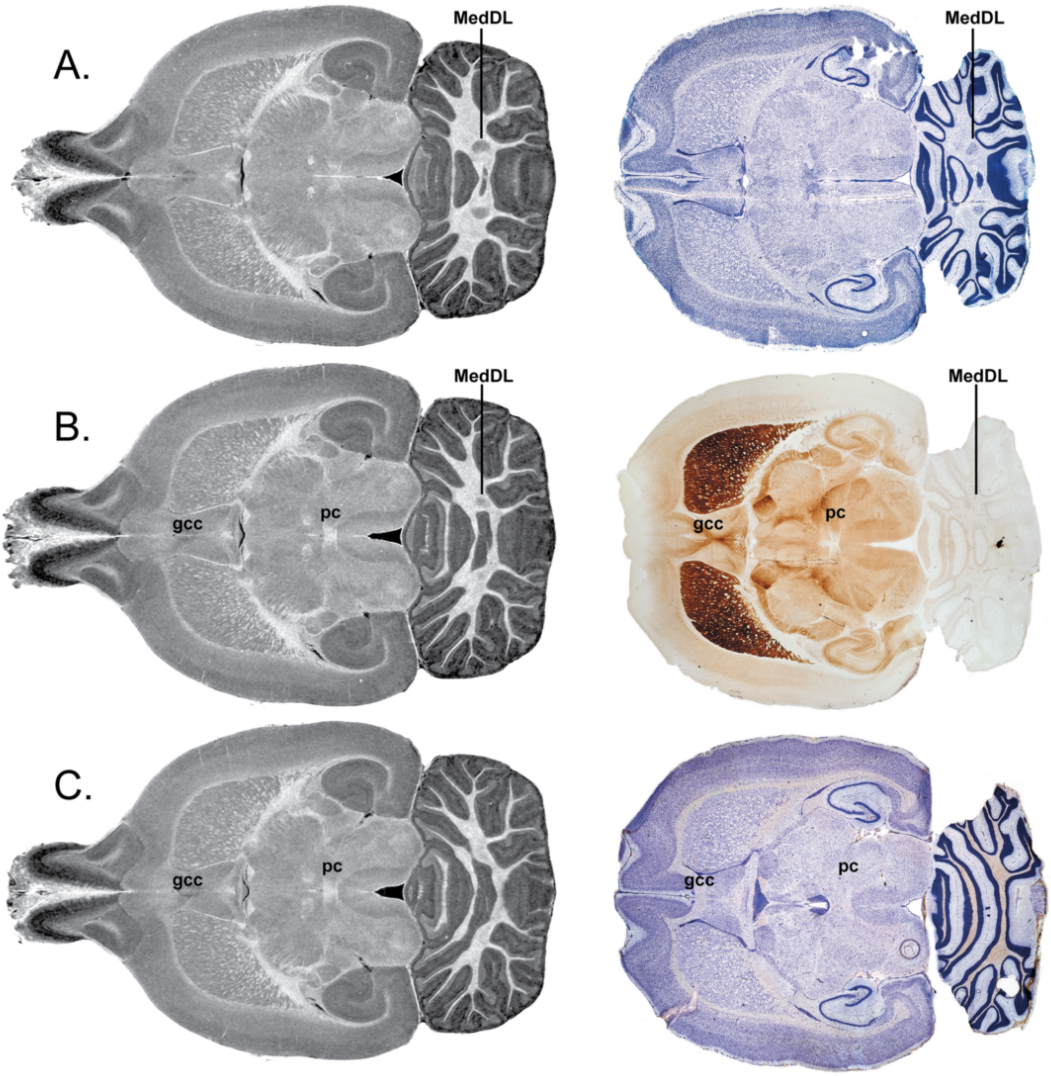

Figure 6 - Three adjacent horizontal slices from the Paxinos and Watson atlas and the corresponding GRE images demonstrating the alignment of MR data to histology. MR contrast has been inverted to better match histology contrast. Row A corresponds to Paxinos and Watson atlas Figure 198 (interaural 4.68). In this plane, the medial cerebellar nucleus (MedDL) is visible posteriorly, but the crossing of the posterior commissure (pc) and the genu of the corpus callosum (gcc) are not yet visible anteriorly. Row B corresponds to Paxinos and Watson Figure 199 (interaural 4.90 mm), the section immediately dorsal to Row A. The three major landmarks that define this horizontal slice are the ventralmost aspect of the gcc, the ventralmost aspect of the pc, and the dorsalmost aspect of MedDL. Row C corresponds to Paxinos and Watson Figure 200 (interaural 5.26), the section immediately dorsal to Row B. In this horizontal plane, MedDL is no longer visible, while the gcc and pc remain in plane. The corresponding MR images closely match the landmarks seen in the histology sections.

Table 2 - The rostrocaudal position of 21 landmarks in the Paxinos-Watson atlas (relative to the interaural zero) compared with their rostrocaudal position (in mm) in the MR coronal slices. In the far-right column, the discrepancy is listed in each case. The mean discrepancy was 0.27 mm.

Structure	AP atlas coordinate	Slice number	Slice AP coordinate	Discrepancy
emergence of 7n	-1.08	548	-1.075	0.005
rostral AmbC	-3.00	467	-3.20	0.20
caudal IOPr	-4.56	407	-4.70	0.14
caudal IOM	-6.00	343	-6.30	0.30
rostral pyr decussation	-5.65	332	-6.50	0.85
xscp caudal	1.08	634	0.975	0.03
4N center	1.68	657	1.55	0.13
RMC caudal	2.40	689	2.35	0.05
rcc caudal	3.72	738	3.57	0.15
fr ventral end	3.84	740	3.65	0.19
caudal mam. bodies	3.60	741	3.65	0.05
fr emerges Hb	5.40	802	5.18	0.02
caudal VMH	5.65	829	5.90	0.35
hippocampus rostral end	7.28	866	6.77	0.61
sox middle	7.56	916	8.05	0.41
rostral LOT	8.28	892	7.50	0.78
rostral to ac	9.00	955	9.00	0.00
rostral end of CPu	11.76	1050	11.37	0.39
ventral taenia tecta - middle	13.20	1125	13.25	0.05
frontal pole	15.12	1171	14.4	0.72
caudal GlA	14.64	1160	14.1	0.54

3.3.4. Atlas dimensionality

The final atlas is truly multidimensional, being comprised of the three spatial dimensions, the fourth dimension of time (neurodevelopment) and a fifth dimension of image contrast. Figure 7 attempts to capture the high level of dimensionality of the atlas. On the left side of the figure, T2-weighted horizontal slices through the genu of the corpus callosum are shown for each of the nine atlas time points, increasing from postnatal day zero (p0) at the top to postnatal day 80 (p80) at the bottom. Figure 7A shows a three-plane view of the p0 gradient recalled echo volume, illustrating that each time point features isotropic data comprising the three spatial dimensions of the atlas. Figure 7B displays the average whole-brain tractography set from the p18 time point. Tractography segments are colored based on orientation of the primary eigenvector following standard coloring convention (red= left/right; green = rostral/caudal; blue = dorsal/ventral). Each atlas time point has five individual tractography volumes and a sixth, average tractography volume derived from the average tensor. Figure 7C demonstrates the MR contrast dimension of the atlas by displaying the seven other image contrasts (excluding T2-weighted) that exist for each time point. The abbreviations used for the different contrasts are listed in Table 3.

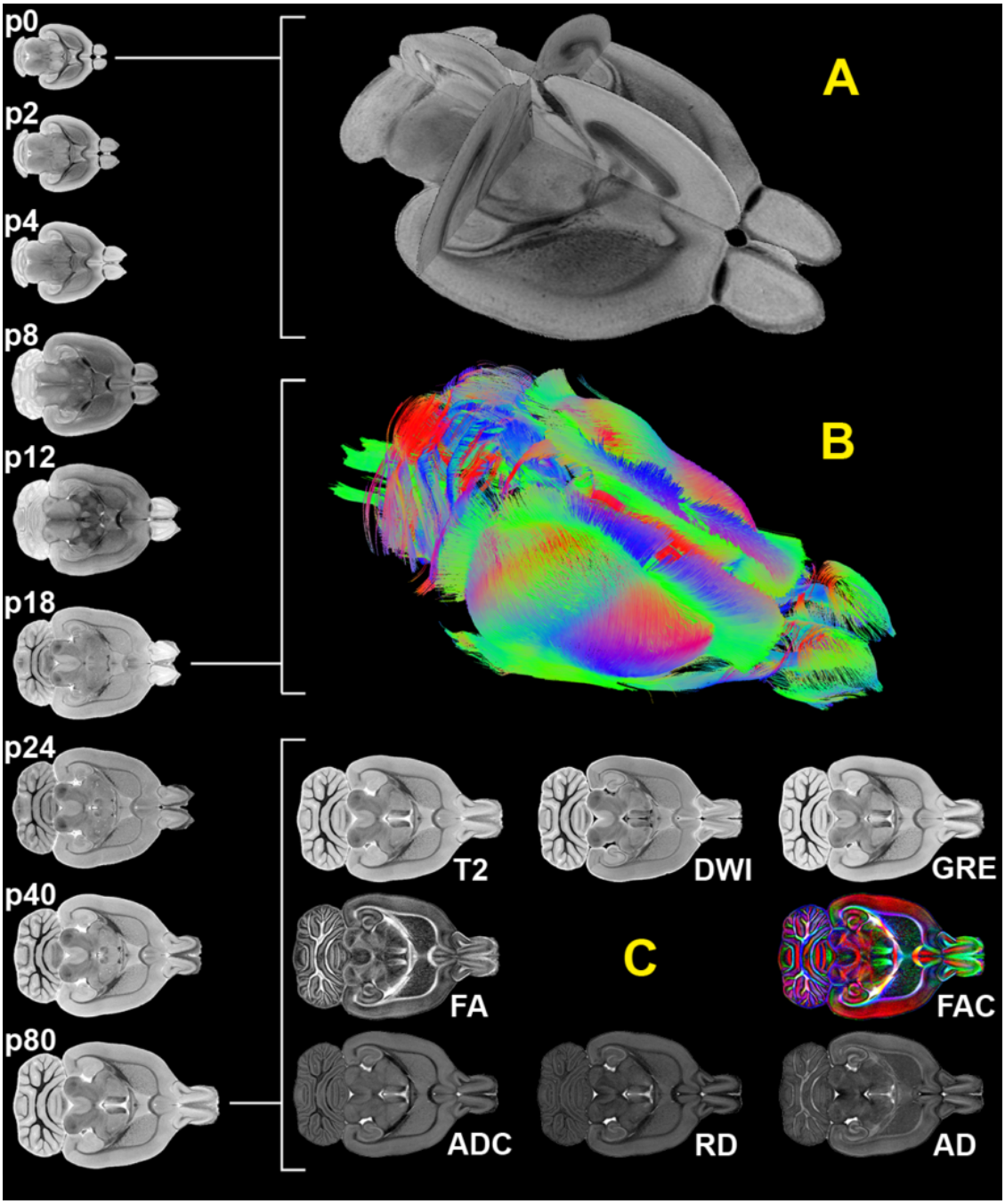

Figure 7 - The multidimensionality of the atlas. Horizontal, T2-weighted images through the genu of the corpus callosum for each atlas time point are shown to scale on the left of the figure. A highlights the three spatial dimensions of the atlas with a three-plane view of the p0 average GRE. B shows whole-brain tractography from the p18 average tensor. Each time point has associated tensor and tractography volumes. C demonstrates the eight image contrasts included in the atlas. A single horizontal slice from the p80 average dataset is shown for each contrast.

Table 3 - Abbreviations and descriptions of the eight different atlas contrasts. ‡ indicates a quantitative contrast (i.e. voxel values represent a meaningful physical quantity).

Abbreviation	Contrast	Description
ADC‡	Apparent diffusion coefficient	Magnitude of water diffusion in mm^2/s
AD‡	Axial diffusivity	Magnitude of water diffusion along primary eigenvector of the tensor in mm^2/s
DWI	Mean diffusion weighted image	Average of the 6 diffusion weighted images
FA‡	Fractional anisotropy	A normalized ratio of eigenvalue differences to the apparent diffusion coefficient
FAC‡	Fractional anisotropy color map	The above colored based on fiber orientation
GRE	Gradient recalled echo	T2*-weighted gradient echo
RD‡	Radial diffusivity	The mean of the secondary and tertiary eigenvalues of the tensor in mm^2/s
T2	T2-weighted contrast	T2-weighted spin echo

4. Creating an ontology-based segmentation scheme for tracking postnatal changes in the developing rodent brain

The work presented in this chapter was published in NeuroImage in 2012 (Calabrese et al., 2012).

4.1. Introduction and background

Using DT-MRH to quantify postnatal neurodevelopmental changes presents a unique set of problems (Johnson et al., 2002a; 2007; Badea et al., 2007a; Petiet et al., 2008; Chuang et al., 2011). Typically, comparisons between quantitative image sets are done using whole-brain, voxel-wise, or region of interest (ROI)-based approaches (Giuliani et al., 2005). Large postnatal changes in brain shape and volume make whole-brain and voxel-wise approaches problematic, leaving the ROI-based approach the most straightforward type of comparison. Unfortunately, manual segmentation is difficult and time consuming, and because of this, previous attempts to track postnatal imaging biomarkers have focused on only a handful of major brain regions (Zhang et al., 2005; Chuang et al., 2011). Further, the chosen segments are often based on what is convenient and not necessarily on biology.

To appropriately characterize postnatal brain changes, one must consider the developmental origins of different parts of the brain. For example, it does not make sense to track developmental changes in the collection of deep motor nuclei known commonly as the “basal ganglia,” when in fact this functionally

defined group contains descendants of at least three distinct major embryonic subdivisions—the striatum (arising from the subpallial telencephalon), the subthalamic nucleus (arising from the basal hypothalamus), and the substantia nigra which has components arising from the hindbrain, mesencephalon, and diencephalon (Watson, 2012; Puelles et al., 2012a; 2012b; 2012c). Clearly it would be difficult to sort out whether quantitative developmental changes in the "basal ganglia" were arising from the telencephalon, diencephalon, mesencephalon, hindbrain, or some combination thereof. For this reason, when studying neurodevelopment, researchers must move away from dated classifications of brain regions, and instead classify regions based on a developmentally defined brain ontology.

A developmental brain ontology is a hierarchically organized set of brain regions defined based on their embryonic origins, an excellent example of which is the chick brain ontology (Puelles et al., 2007). A number of attempts have been made to create a mammalian brain ontology in the recent past, the most notable of which include the NeuroNames ontology (Bowden and Martin, 1995), the Brain Architecture Knowledge Management System (BAMS) (Bota and Swanson, 2008), Biomedical Informatics Research Network (BIRN) (Bug et al., 2008), and the Allen Brain Atlas ontology (Dong, 2008). These four ontologies are limited in that they are based on a traditional topological classification of brain components. Another issue is that all of these ontologies, including the chick brain ontology, are based in large part on conventional histology, which allows identification of subtle borders and small nuclei. Because MRH has limited

resolution (10-25 μm) and uses a variety of contrast mechanisms, none of which exactly recapitulates conventional histology stains, the range of structures that can be readily identified in MRH volumes of the mammalian brain is limited. Fortunately, an exhaustive collection of structures is not necessarily desirable for quantifying postnatal neurodevelopment because of the time involved in manual segmentation at several different time points. Large-scale screening and quantification studies require a comprehensive yet tractable segmentation that can be preformed rapidly and reliably throughout postnatal life.

An ideal segmentation scheme for tacking imaging biomarkers throughout postnatal neurodevelopment would be comprehensive, ontologically based, technically realizable, and flexible enough to accommodate further advances in MRH. Here we introduce a developmental ontology and segmentation scheme that attempts to satisfy each of these requirements. The ontology presented here is comprehensive in that it covers the entirety of the mammalian brain. It is ontologically based in that the brain divisions are based on a wide range of developmental neuroscience research including histology, gene marker studies, fate mapping, and in-situ hybridization, which have been compiled in the avian brain ontology of (Puelles et al., 2007). We demonstrate the technical feasibility of this ontologically based segmentation scheme throughout postnatal neurodevelopment by successfully segmenting MRH volumes of the rat brain immediately after birth (postnatal day 0–p0) and at adulthood (postnatal day 80–p80). Finally, we discuss the flexibility of this ontology in accommodating new imaging technologies and brain images of other mammalian species.

4.2. Methods

We based our segmentation scheme on the three major embryonic subdivisions of the brain—the hindbrain, midbrain, and forebrain. Each major subdivision was parcellated into smaller, constituent parts based on the borders that can be rapidly and reliably identified on T2* and diffusion weighted MRI. We focused on relatively large structures that are likely to be useful for quantitation of postnatal changes and omitted some smaller regions that we felt would not contribute significantly to the utility of the segmentation as a screening tool (e.g. the individual lobules of the cerebellum). T2* and diffusion weighted contrasts were chosen because they are both commonly used in MRH studies and they rely on two very different sources of contrast (spin-spin relaxation and diffusivity, respectively). In addition, several previous studies have noted that T2* and diffusion weighted contrasts highlight different, and somewhat complementary brain anatomy (Kovacevic et al., 2005; Ma et al., 2005; Chuang et al., 2011; Johnson et al., 2012). All 3D digital segmentation of MRI volumes was accomplished using Avizo 3D analysis software (Visualization Sciences Group, Burlington, MA, USA).

4.3. Results

4.3.1. Selection of structures for segmenting MRH volumes

We identified 26 developmentally defined structures that collectively represent the entire brain. Importantly, each of these structures is visible in both the early postnatal (p0) and adult (p80) rat brain, allowing a consistent

segmentation scheme to be used throughout postnatal neurodevelopment. A complete hierarchical list of these structures is presented in Table 4. The MAIN ONTOLOGY section presents structures that are clearly derived from one of the three major embryonic subdivisions of the brain: hindbrain, midbrain, and forebrain. The SPECIAL CASES section of Table 4 contains two groups of structures that do not comfortably fit into the main ontology framework. One group includes developmentally diverse structures, which arise from two or more major embryonic subdivisions of the brain, and the other includes major white matter structures, which course through two or more discrete brain regions. Table 5 lists the 26 structures in alphabetical order along with their color code, which will be used to identify these structures throughout this document.

Table 4 - Hierarchical organization of the developmentally defined ontology for segmenting rodent MRH brain volumes. In the MAIN ONTOLOGY section, parent structures are subdivided to constituent parts at each level of the bulleted tree (i.e. axial hindbrain is part of hindbrain).

MAIN ONTOLOGY

- **Hindbrain**
  - Axial Hindbrain
  - Cerebellum
- **Midbrain**
- **Forebrain**
  - Diencephalon
    - Pineal gland
  - Hypothalamus
  - Telencephalon
    - Pallium
      - Hippocampal Formation
      - Isocortex
      - Olfactory Structures
    - Subpallium
      - Amygdala
      - Bed Nucleus of the Stria Terminalis
      - Diagonal Domain
      - Pallidum
      - Preoptic Area
      - Septum
      - Striatum
        - Accumbens Nucleus

SPECIAL CASES

- **Developmentally diverse structures**
  - Pituitary
  - Substantial Nigra
  - Ventricles
- **Major white matter structures**
  - Anterior Commissure
  - Cingulum
  - Corpus Callosum/Deep Cerebral White Matter
  - Fimbria/Fornix
  - Internal Capsule/Cerebral Peduncle/Pyramids
  - Optic Pathways

Table 5 - Color code for brain structures used throughout this document.

Structure	Color
Accumbens nucleus	
Amygdala	
Anterior Commissure	
Axial Hindbrain	
Bed Nucleus of the Stria Terminalis	
Cerebellum	
Cingulum	
Corpus Callosum/Deep Cerebral White Matter	
Diagonal Domain	
Diencephalon	
Fimbria/Fornix	
Hippocampal Formation	
Hypothalamus	
Internal Capsule/Cerebral Peduncle/Pyramids	
Isocortex	
Mesencephalon	
Olfactory Structures	
Optic Pathways	
Pallidum	
Pineal Gland	
Pituitary	
Preoptic Area	
Septum	
Striatum	
Substantial Nigra	
Ventricles	

4.3.2. Segmentation of p0 and p80 rat brain MRH volumes

We manually segmented early postnatal (p0) and adult (p80) rat brain image volumes into the 26 structures listed in Table 5. The segmented images were an average of five different specimens, which were registered together using a minimum deformation template strategy to reduce individual specimen bias. The results of this segmentation are presented in Figure 8 and Figure 9. Figure 8 shows three coronal sections from both the p0 (Figure 8 A-C) and p80 (Figure 8 D-F) rat brain with the segmentation presented as a color overlay.

Corresponding sections (i.e. Figure 8 A and Figure 8 D) are roughly analogous; however, a perfect match is not possible due to significant bending of the neuraxis that occurs during postnatal neurodevelopment in the rat. Figure 8 A and D are sections through the decussation of the anterior commissure, Figure 8 B and E through the rostral portion of the hippocampal formation, and Figure 8 C and F through the caudal portion of the hippocampal formation. Images were scaled to the same size to show detail. A 1-cm reference is provided for scale.

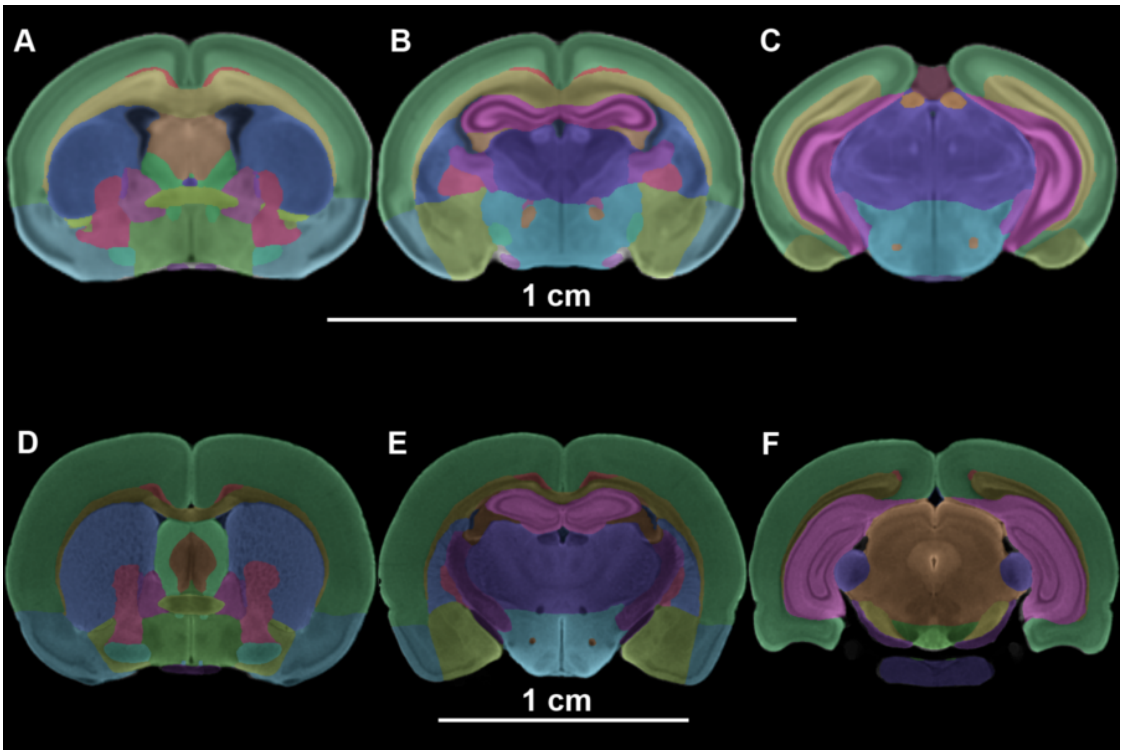

Figure 8 - The complete p0 (A-C) and p80 (D-F) segmentation presented as 2D color-overlays on coronal, isotropic diffusion-weighted images. The colors used are consistent with those shown in **Table 5**. A and D are sections through the decussation of the anterior commissure, B and E through the rostral portion of the hippocampal formation, and C and F through the caudal portion of the hippocampal formation.

Figure 9 shows the p0 and p80 segmentation as rendered 3D surfaces. The isocortex and corpus callosum/deep cerebral white matter complex are displayed in transparency to show underlying structures. Once again, p0 (top) and p80

(bottom) images are scaled to the same size to show detail. Figure 9 A and D are profile views with the olfactory bulb angled to the bottom right of the Figure and the brainstem angled to the top left. Figure 9 B and E are dorsal views and Figure 9 C and F are ventral views, with the olfactory bulb on the right in each case.

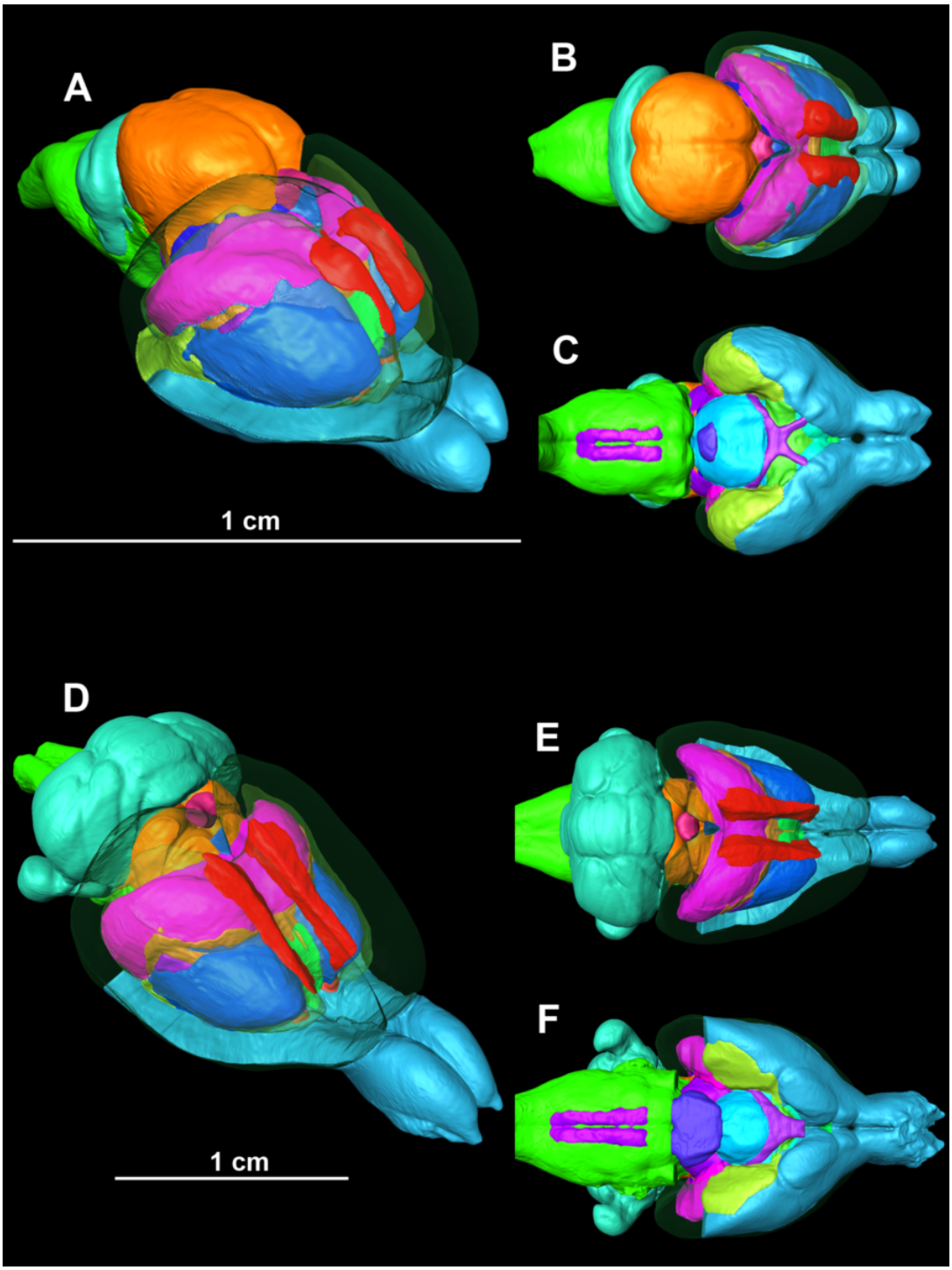

Figure 9 - The complete p0 (A-C) and p80 (D-F) segmentation presented as 3D rendered surfaces. The colors used are consistent with those shown in **Table 5**. A and D are profile views with the olfactory bulb pointed to the bottom right; B and E are dorsal views with the olfactory bulb to the right; and C and F are ventral views with the olfactory bulb to the right.

Figure 10 demonstrates the contrast differences between gradient recalled echo (GRE) images (Figure 10 A) and isotropic diffusion weighted images (DWI) (Figure 10 B) in the p80 rat brain. Both images (Figure 10 A-B) are taken from the same coronal plane at the level of the posterior commissure. The magnified insets show the caudal amygdala and ventral hippocampal formation in the two image contrasts. The most striking anatomical differences between the two contrasts are indicated with arrows and/or structure abbreviations. Abbreviations are consistent with the standard rat brain nomenclature used in the Paxinos and Watson adult rat brain atlas (Paxinos and Watson, 2007).

4.4. Discussion

A number of previous studies have attempted manual, whole brain segmentation of MRI volumes with widely varying results. Even in the relatively small field of rodent brain MRI, a majority of published whole brain segmentation attempts use dramatically different ontologies and nomenclature sets (Kovacevic et al., 2005; Ma et al., 2005; Johnson et al., 2010; Chuang et al., 2011). This problem is compounded in the case of postnatal neurodevelopment where even fewer structures are visible on MRI (Zhang et al., 2005; Chuang et al., 2011). The general lack of consensus on which structures can, and should, be routinely segmented in mammalian brain MRI highlights the need for a robust and relevant ontology designed for this purpose. Such an ontology would not only provide a guideline for future segmentation attempts, but would also allow comparison of results between studies. A unified ontology and nomenclature is essential for

effective communication of brain segmentation results, but its usefulness can be extended by focusing on the developmental origins of the brain (Puelles et al., 2007). Recently there has been growing interest in the importance of postnatal neurodevelopment and in the use of MRI to study neurodevelopmental changes both in normal and disease states (Mori et al., 2001; Knickmeyer et al., 2008; Giedd and Rapoport, 2010). An ideal brain MRI segmentation ontology would, therefore, be consistent and tractable throughout postnatal life, allowing developmentally relevant comparisons of MR biomarkers in brain sub-regions throughout neurodevelopment. It is with this in mind that we have created the developmental ontology presented in Table 4.

4.4.1. The developmental ontology

Several features of this ontology warrant explanation. First, the list of structures that we have selected (see Table 5) is not intended to be exhaustive; any one of the structures in Table 5 could be further subdivided in to several different parts based on a priori anatomic knowledge or comparison with conventional histology (Richards et al., 2011); however this level of detail is impractical for brain-wide quantitation of postnatal development. Our goal was to great a logical, tractable list of structures that could be used to screen for and quantify regional postnatal changes in volume and other MRI metrics. The list in Table 5 was designed to: 1) cover the entire brain volume, 2) use only those structures whose borders are readily apparent using the MRH imaging strategies we have employed, and 3) focus on structures that are of particular interest in

current brain research, particularly neurodevelopmental investigations. The MAIN ONTOLOGY section of Table 4 is a hierarchical list of those brain regions that clearly originate from, and are part of, only one of the three major embryonic subdivisions of the brain: the hindbrain, the midbrain, and the forebrain.

4.4.2. Hindbrain

The hindbrain is divided into the cerebellum and the axial hindbrain. Although many older neuroanatomy texts divide the hindbrain into the metencephalon (consisting of the cerebellum and the pons) and the myelencephalon (consisting of the medulla oblongata), this division is based on the external appearance of the human brain rather than on the developmental origins of the mammalian hindbrain (Watson, 2012). The rostral part of the hindbrain, consisting of the isthmus and rhombomere 1, gives rise to the cerebellum (Puelles et al., 2007). The term “axial hindbrain” refers to the remainder of the hindbrain consisting of rhombomeres 2-11.

4.4.3. Midbrain

The midbrain is not further subdivided for this segmentation. The reason for this is two-fold: 1) the midbrain consists largely of the tectum and tegmentum, the border between which is difficult to identify, particularly in the neonatal rat brain, and 2) the boundary between the two segmental components (mesomeres) (Puelles et al., 2012a) is also difficult to see on rodent MRI.

4.4.4. Forebrain

The forebrain is the most extensively subdivided of the three major embryonic divisions in our ontology for a number of reasons. First, the forebrain is the largest of the three divisions in virtually all vertebrate species (Puelles et al., 2007; Watson et al., 2012). Second, the forebrain is the focus of a majority of research on human neurologic diseases including Alzheimer's disease, Parkinson's disease, schizophrenia, autism, and many others. Finally, the forebrain is quite heterogenous in appearance on MRI, and several major borders are readily apparent. The first major subdivision of the forebrain yields the hypothalamus (including the eye), diencephalon, and telencephalon (Puelles et al., 2007). Many neuroanatomy texts list the hypothalamus as part of the diencephalon; however, recent gene expression studies have provided substantial evidence that these two brain regions are both genetically and developmentally distinct (Puelles and Rubenstein, 2003). The telencephalon is further divided into the pallium and subpallium.

Within the pallium are the major cortical structures including the hippocampal formation (the dentate gyrus, subiculum, and the hippocampus proper—the medial pallium), the olfactory structures (the olfactory bulb, olfactory tubercle, lateral olfactory tract, and the piriform cortex—the ventral pallium), and the lateral and dorsal pallium (the last of which is represented by the neocortex in mammals) (Puelles et al., 2007).

The subpallium is further divided into eight structures, two of which require further explanation. First, the accumbens nucleus, although generally considered

to be part of the striatum, is segmented separately because of its clinically relevant role in addiction and reward circuitry, and because it has quite distinctive borders on diffusion weighted MRI (Kelly et al., 1975; Sturm et al., 2003). Second, the bed nucleus of the stria terminalis is segmented separately because it is developmentally distinct from the adjacent septum and because it is believed to play an important role in fear responses and the development of sex differences in mammals (Hines et al., 1992; Walker et al., 2003).

4.4.5. Special cases

The SPECIAL CASES section of the ontology is reserved for two classes of structures that do not comfortably fit into the main ontology hierarchy: the developmentally diverse structures and the major white matter tracts. The term “developmentally diverse structures” refers to those structures that develop from two or more distinct embryonic domains. This group includes the pituitary gland, which is derived from the hypothalamus and oral ectoderm; the substantia nigra, which has both midbrain and forebrain components; and the ventricles, whose walls are formed by all three major embryonic divisions of the brain (Watson et al., 2012). An additional benefit in listing these structures separately is the unique role that they play in human diseases. For example, the pituitary is involved in a variety of endocrine disorders, the substantia nigra in Parkinson’s disease, and ventricle volume is a surrogate marker for the cortical volume loss seen in Alzheimer’s disease (Silbert et al., 2003).

4.4.6. Major white matter structures

The “major white matter structures” section contains several major white matter tracts that are not completely contained within another structure. These white matter structures are segmented separately because: 1) they may contain projections from multiple different brain regions, 2) they pass through or along multiple different structures, and 3) there is considerable interest in measuring normal and/or pathologic changes in white matter structures throughout neurodevelopment (Mukherjee and McKinstry, 2006; Asato et al., 2010; Chuang et al., 2011). In most cases, the listed white matter structures are a composite of two or more white matter structures as defined by the Paxinos and Watson atlas of the adult rat brain (Paxinos and Watson, 2007). For example, the corpus callosum, external capsule, and deep cerebellar white matter are combined into a single structure, as are the internal capsulae, the cerebral peduncles and the pyramids. This grouping is done because these pathways are actually continuous with each other and separating them would require drawing an arbitrary line based on surrounding landmarks. Such dividing lines could easily be added, but we believe that they do not considerably increase the utility of the resulting label set.

4.4.7. Challenges to segmentation of the developing rodent brain

Despite substantial changes that occur in both the neuraxis and in total brain volume during development, segmentation of the p0 and p80 rat brain using our ontology was remarkably similar. The only major difference that

complicated segmentation was that the p0 brain contains a significant amount of neuroepithelium surrounding the lateral ventricles, which is absent in the adult rat brain. The neuroepithelium contains neural precursor cells that differentiate into the surrounding brain structures during postnatal neurodevelopment (Frederiksen and McKay, 1988). Because of this, we chose to allocate parts of the neuroepithelium to the nearest neighbor. Practically speaking this involves dividing the neuroepithelium between the adjoining striatum and septum based on proximity.

Due in part to the limited spatial resolution and contrast resolution provided by MRH, some brain regions can be quite difficult to reliably segment. One of the most valuable assets to the would-be segmenter is the use of multiple different MR contrasts. Just as conventional neurohistologists rely on multiple tissue stains, such as Nissl, acetyl cholinesterase, and calbindin, so too should the MR histologist rely on multiple "proton stains" such as T2*-weighting and diffusion-weighting (Delnomdedieu et al., 1996). A particular brain structure border may be nearly invisible on one MR contrast, and readily apparent on another. By using multiple MR contrasts for segmentation, one can circumvent many of the contrast limitations of MRH as compared to conventional histology.

The rat amygdala highlights the utility of using multiple MR contrasts for brain segmentation. Figure 10 shows a coronal section of the adult rat brain at the caudal border of the amygdala displayed with T2*-weighted contrast (Figure 10 A) and diffusion-weighted contrast (Figure 10 B). The T2*-weighted image shows excellent white matter contrast, which reveals the full extent of the deep

cerebral white matter (dcw) both laterally and ventrally. Additionally, the optic tract (opt) is visible as it runs between the diencephalon and the dentate gyrus. Despite this exquisite white matter detail, the ventral cortical region of the T2*-weighted image is virtually devoid of image contrast. In comparison, the diffusion-weighted image (Figure 10 B) quite clearly reveals the caudal amygdaloid nuclei: the posteromedial cortical amygdaloid nucleus (PMCo) and the amygdalopiriform transition area (APir). Further, the caudal extent of the piriform cortex can clearly be identified based on the high level of diffusion attenuation present in layer 2 (Pir2). In this example, and in many others, these different image contrasts each contributed unique and essential information for identifying the structures listed in Table 5. Just as no rational histologist would attempt to segment an entire brain based on one tissue stain, we suggest that no accurate whole brain segmentation can be achieved with only a single MR contrast.

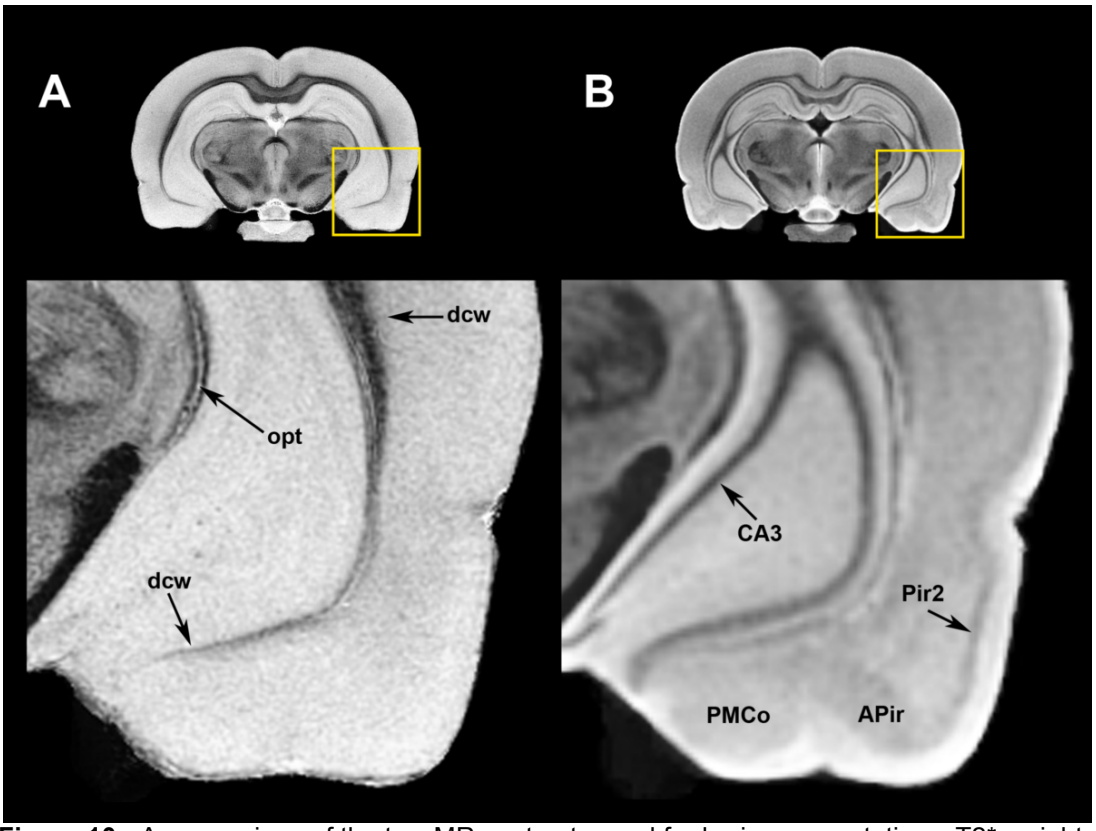

Figure 10 - A comparison of the two MR contrasts used for brain segmentation—T2*-weighted contrast (A) and isotropic diffusion-weighted contrast (B). Magnified insets show a coronal section through the caudal amygdala. The T2*-weighted image shows excellent white matter contrast including the deep cerebral white matter (dcw) and the optic tract (opt). In contrast, the diffusion-weighted image shows excellent contrast in the posteromedial cortical amygdaloid nucleus (PMCo), the amygdalopiriform transition area (APir), and layer 2 of the piriform cortex (Pir2). Also labeled is the CA3 layer of the hippocampus.

5. Analysis of regional volume changes throughout postnatal neurodevelopment

The work presented in this chapter was published in NeuroImage in 2013 (Calabrese et al., 2013).

5.1. Introduction and Background

Virtually all MRI-based brain atlases place a strong emphasis on quantitative measurements of regional brain volume. Accurate, quantitative morphometry is possible with MRH because it is non-destructive, non-distorting, and inherently digital. Regional volume changes are particularly important in the developing brain, and have been the focus of the two existing MRI-based atlases of mouse neurodevelopment (Zhang et al., 2005; Chuang et al., 2011). Although volume is not a direct measure of brain function, it can be used as a surrogate for neuropathology. For example, abnormal morphologic neurodevelopment has been identified in both autism spectrum disorders and schizophrenia (Courchesne et al., 2001; Mehler and Warnke, 2002). Unfortunately, manual segmentation of MRI volumes is tedious and time-consuming, and a majority of previous atlases track volume changes in only a small number of regions. Of the previously mentioned atlases of mouse brain development, Chuang et al. (2011) tracks volume change in three compartments (cortex, cerebellum and hippocampus) and Zhang et al. (2005) in four compartments (cortex, cerebellum, hippocampus and caudate/putamen). Nonetheless, these atlases provide valuable, quantitative information about the normal course of rodent brain

development. A comparable analysis of rat brain neurodevelopment would provide a framework for detecting developmental abnormalities in a variety of diseases that are more easily modeled in the rat.

5.2. Methods

5.2.1. Quantitative volumetric analysis and statistics

To demonstrate the quantitative value of our atlas, we analyzed regional volume changes in the rat brain throughout postnatal neurodevelopment. Volumes were calculated for each of the 26 manually segmented brain regions in each of the 45 atlas specimens (five specimens at each of nine time points). Volumes were calculated by multiplying the number of voxels in a segmented region by the voxel volume (15.6 picoliters for the T2*-weighted image volumes). Regional volumetric data were then imported into JMP Pro 9 statistics software (http://www.jmp.com) for further analysis. For each region, we performed non-linear regression with a Gompertz sigmoidal growth model:

$$f(t) = a \times \exp(-e^{c(b-t)})$$

where *t* is time after birth measured in days (Jolicoeur et al., 1992). Fitting data to this model provides estimates of three parameters: *a* = the expected adult volume in µl, *b* = the abscissa of the inflection point of the growth curve, and *c* = the relative growth rate at the inflexion point. We also tested for statistical differences in regional brain volume between all time points using ANOVA and Tukey's HSD test. Finally, to assess local morphologic variance, we created

mean positional difference (MPD) maps at each time point by taking the mean of the five specimen-to-average warp vector magnitudes (Kovacevic et al., 2005).

5.3. Results

5.3.1. ROI-based volumetric analysis

We measured the volume of each of the 26 brain regions at all nine time points included in the atlas. The complete data table is provided online at http://www.civm.duhs.duke.edu/ratbraindevatlas/. The estimated Gompertz parameters for all 26 structures are presented in Table 5, along with the R^2 values for the regression. Figure 11 shows volume data versus postnatal day for 12 major brain regions plotted alongside the estimated Gompertz growth function. Also shown are the predicted and measured 95% confidence intervals and the R^2 values for the regression.

Figure 12 is intended to be a different way of visualizing the same morphometric data shown in Figure 11. In Figure 12, atlas time points are treated as nominal rather than continuous variables, so the x-axis is not proportional to age. Box and whisker diagrams are included to show the data distribution including the median (box band) the 75^{th} and 25^{th} percentile (top and bottom of box respectively) and the max and min (whiskers). For each brain region, all pairs of mean volumes were compared using Tukey's HSD test to correct for multiple comparisons. The mean comparison circles on the right side of each plot have a diameter equal to the 95% confidence interval of the corresponding data. Two means are statistically different (i.e. $p<0.05$) if the comparison circles do not

overlap, or if the outside angle of their intersection, θ, is less than 90° (see Figure 12 legend).

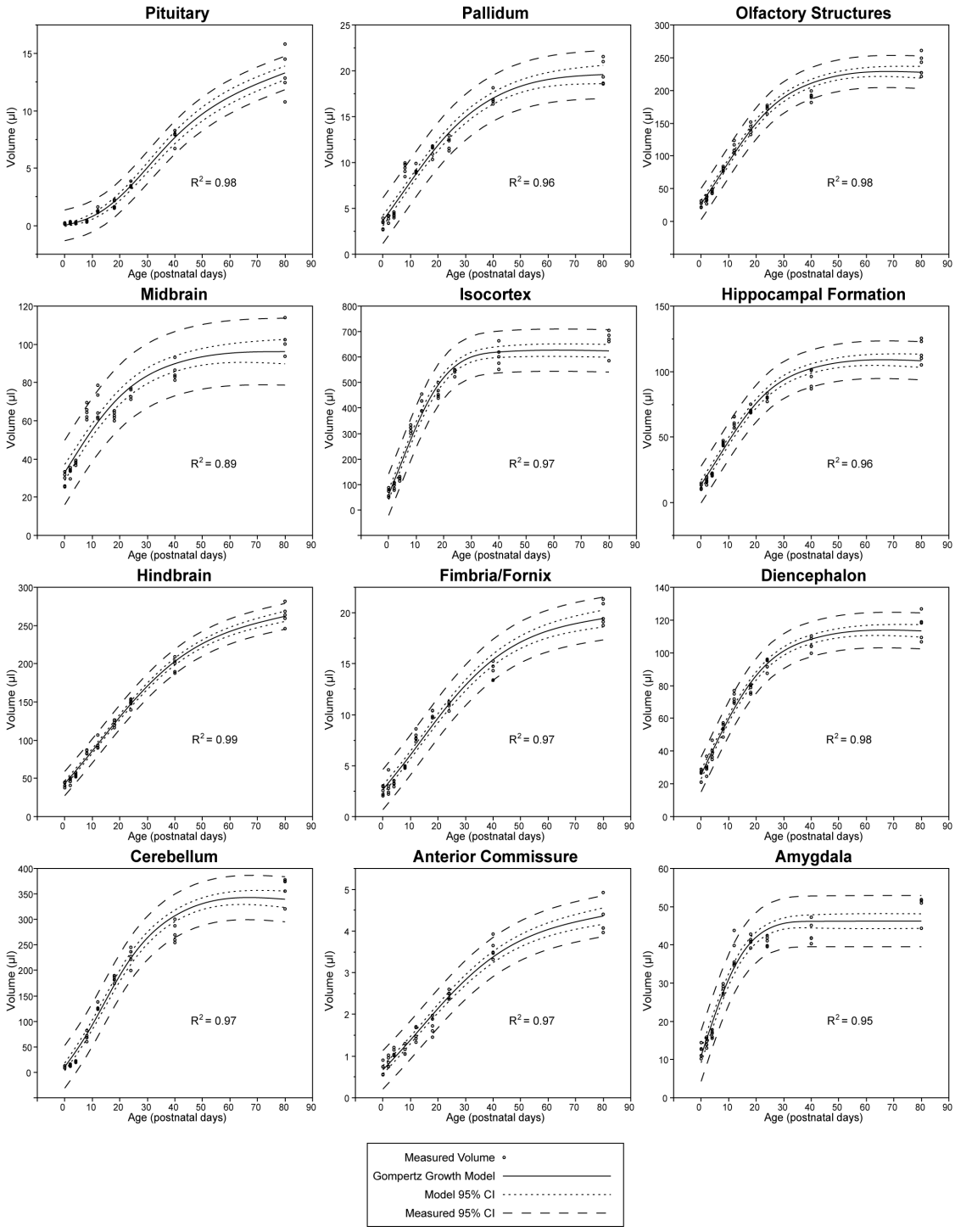

Figure 11 - Gompertz growth models for 12 selected brain regions. For each region we have plotted the raw volume data (open circles) over the estimated model (solid line). Also shown are the 95% confidence intervals for the model (small dashed line) and for the measured data (large dashed line), and the R^2 values for the regression. Estimated Gompertz parameters for all structures are shown in **Table 6**.

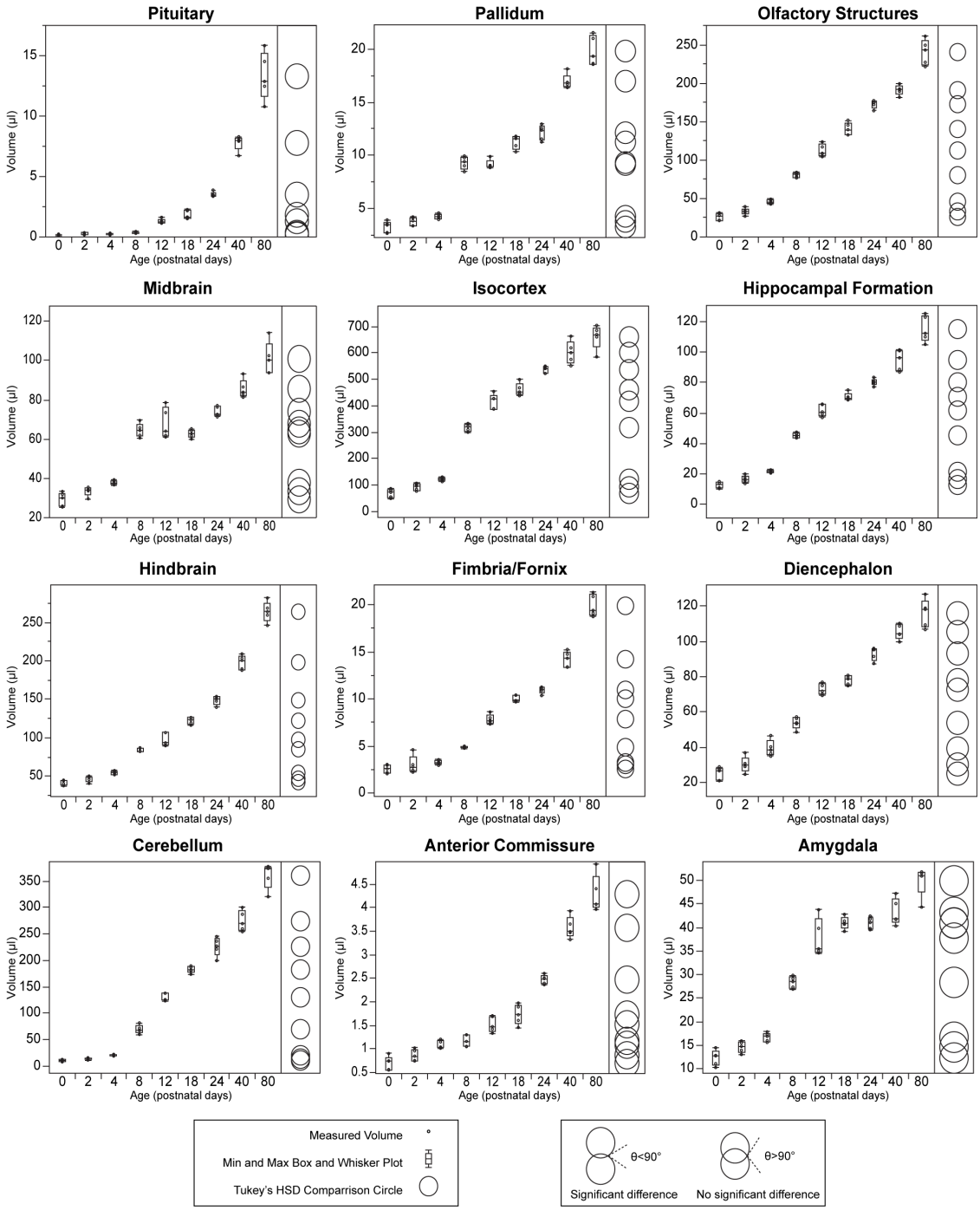

Figure 12 - Comparison of means for 12 selected brain regions. Raw structure volume data are plotted along with min and max box and whisker plots to show data distribution. The comparison circles to the right of each plot were generated with Tukey's HSD comparison of means. Two groups are statistically different if their comparison circles do not overlap, or if the outside angle of their overlap is acute (see legend). Age is used as a nominal variable for these comparisons so the x-axis is not age proportional.

5.3.2. Voxelwise estimates of morphologic variability

Figure 13 provides voxelwise measurements of morphologic variability at each of the nine atlas time points spanning postnatal rat neurodevelopment. For each time point the mean positional difference (MPD) map, generated from the respective warp vector fields, is displayed as a heat-map color overlay on a three-plane view of the average DWI. Color overlays are set to the same scale, which is displayed at the bottom of the figure. Mean MPD across all ages was 129 μm and the maximum observed MPD was 445 μm at p8.

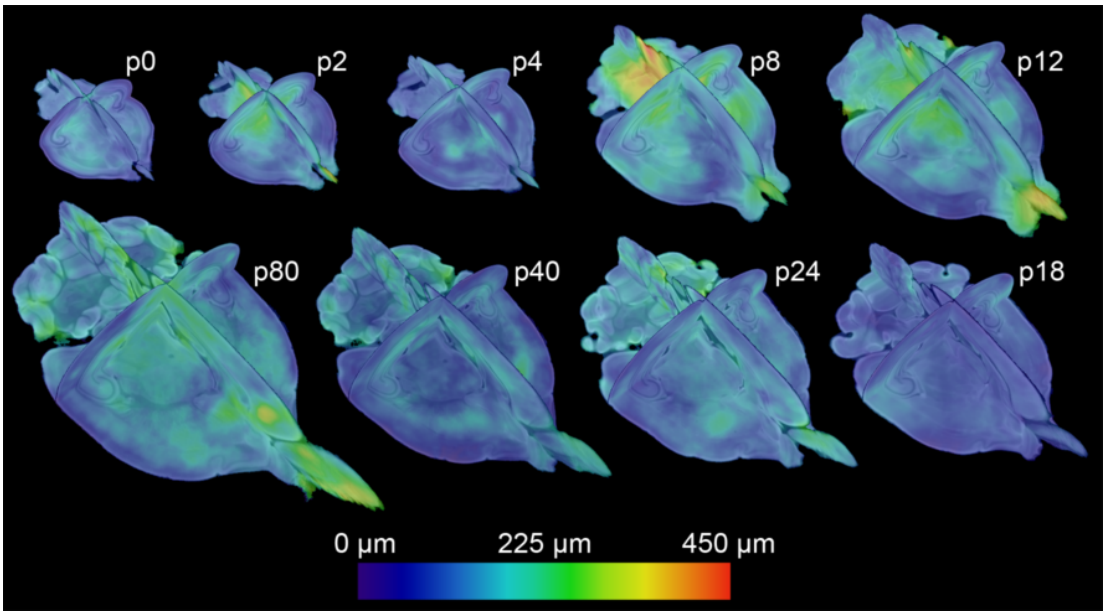

Figure 13 - Mean positional difference (MPD) maps for each time point. Calculated MPD maps are displayed as color overlays on three-plane views of the average DWI for each atlas time point. The MPD scale is consistent across all time points and is shown at the bottom of the figure. The maximum observed MPD was 450 μm.

5.4. Discussion

5.4.1. Quantitative volumetric analysis and statistics

One of the most important advantages of MRH atlasing is the possibility for quantitative morphometry. As part of our quantitative morphometric analysis,

we found that our regional volumetric data was well modeled by a Gompertz sigmoidal growth function. The results of this analysis are presented in Table 6 and Figure 11. All 26 brain regions displayed high coefficients of determination (R^2 values) for the regression; the lowest R^2 value was 0.68 for the bed nucleus of the stria terminalis (BST) and the average value for all structures was 0.93. The estimated growth parameters presented in Table 6 reveal remarkable spatiotemporal heterogeneity in the developing rat brain. The relative growth rate (RGR) (parameter *c*) varies by almost an order of magnitude from 0.018 for the pineal gland to 0.153 for the septum. For some regions, the inflexion point of the growth curve (parameter *b*) occurs within the first few days of postnatal life (i.e. midbrain, septum, hypothalamus, preoptic area), while other regions lag by several weeks (i.e. pituitary, pineal gland, optic pathway). Interestingly, the structures that reach their inflexion point earlier tend to be axial structures involved in basic life support and homeostasis, while those that reach it latest are involved in endocrine and sensory functions that are only necessary after birth (e.g. growth hormone secretion, vision) (Jailer, 1950; Calvo and Boya, 1984). It is important to note that negative values of parameter *b* are not necessarily erroneous, as the growth curve inflection point may have occurred during prenatal development.

Table 6 - Estimates of Gompertz growth parameters for all 26 atlas structures and R^2 values for the regression.

Region	*a*	*b*	*c*	R^2
Cingulum	6.27 µl	9.05 days	0.063	0.94
Midbrain	96.63 µl	1.19 days	0.067	0.89
Substantia Nigra	7.52 µl	10.00 days	0.079	0.97
Anterior Commissure	4.57 µl	13.91 days	0.046	0.97
Hindbrain	275.34 µl	13.56 days	0.045	0.99
Septum	13.38 µl	0.85 days	0.153	0.84
Diagonal Domain	5.70 µl	3.51 days	0.057	0.89
Hypothalamus	38.67 µl	0.40 days	0.100	0.87
Striatum	93.47 µl	6.71 days	0.076	0.96
Diencephalon	113.54 µl	4.71 days	0.085	0.98
Internal Capsule	38.37 µl	14.29 days	0.056	0.99
Hippocampal Formation	108.44 µl	7.95 days	0.088	0.96
Pallidum	19.86 µl	8.67 days	0.060	0.96
Accumbens	15.00 µl	8.81 days	0.059	0.93
Fimbria Fornix	20.13 µl	13.80 days	0.050	0.97
Corpus Callosum	86.52 µl	6.46 days	0.048	0.91
Amygdala	46.23 µl	2.90 days	0.138	0.95
Preoptic Area	9.54 µl	-1.18 days	0.119	0.88
Isocortex	624.32 µl	6.41 days	0.128	0.97
Cerebellum	340.51 µl	13.45 days	0.084	0.97
Olfactory Structures	228.34 µl	9.14 days	0.081	0.98
BNST	3.46 µl	-9.03 days	0.039	0.68
Pituitary	14.35 µl	30.77 days	0.052	0.98
Ventricles	10.54 µl	1.50 days	0.107	0.81
Optic Pathway	6.84 µl	26.39 days	0.036	0.97
Pineal Gland	3.42 µl	44.44 days	0.018	0.88

The growth curves presented in Figure 11 reveal additional spatiotemporal nuances of rat brain development. For example, the volume of cortical structures such as the olfactory cortex, amygdala, hippocampus, and isocortex appear to plateau around p40 while most other structures show at least some growth between p40 and p80. In contrast, white-matter rich structures such as the hindbrain, fimbria/fornix, and anterior commissure exhibit nearly linear growth

throughout postnatal development. These findings are consistent with the theory that late brain development is dominated by increased axonal connections between existing brain regions (Nagy et al., 2004; Toga et al., 2006); however, more studies are needed to establish whether our volume measurements of white-matter structures correlate with increased connectivity.

Interestingly, of structures plotted in Figure 11, only the pituitary shows a significant lag phase at the beginning of the growth curve. This relatively late growth could reflect the fact that placental hormones largely supplant pituitary function during prenatal life (Jailer, 1950). The lack of a lag phase on other growth curves is either because these structures simply do not exhibit significant lag phase growth, or more likely, it occurs during prenatal neurodevelopment. Similar morphometry studies on the prenatal rat brain will be needed to capture the full range of mammalian neurodevelopment.

Direct comparison of our regional volume measurements to previous work based on conventional histology is problematic due to differences in technique. Volumes calculated with conventional histology are prone to error caused by brain extraction, freezing or embedding, sectioning and tissue dehydration during staining. For these reasons, histology-based estimates of regional brain volume tend to underestimate in-vivo volume. For example, C. G. Smith (1933) reported the volume of the p86 male, Wistar rat cortex to be ~400 μL, which is substantially smaller than the p80 isocortex volume reported here (average volume = 661 μL). Similarly, histology-based estimates of hippocampal formation volume collected by S. A. Bayer (1980) are almost 50% lower than the MRH-

based measurements presented here. The majority of previous MRH atlases of the rat brain do not report regional brain volumes (Schwarz et al., 2006; Veraart et al., 2011; Johnson et al., 2012; Nie et al., 2012). Those that do report volume are difficult to compare with the current work because the use different sexes, different image resolution, and different ages/weights for their templates (e.g. Valdés-Hernández et al., 2011).

Figure 12 demonstrates the statistical power of the atlas segmentation. Several factors contribute to the ability to identify a statistically significant volume change between two time points including magnitude of growth, structure variability, and segmentation reproducibility. We have taken several steps to ensure data consistency, such as controlling for litter size and animal body weight. These steps have likely contributed to our ability to detect differences with a relatively modest sample size at each time point (n=5). Higher n's would almost certainly allow more time points to be statistically differentiated, however this is somewhat impractical given the high cost and long scan time required for each specimen. Nonetheless, these data show researchers what they can reasonably expect using similar methods. Some regions, such as the cerebellum and olfactory structures, have statistically significant volume differences at nearly every time point. Several late-developing regions including the anterior commissure and pituitary have indistinguishable volumes in the pre-weaning period (i.e. before postnatal day 20) and relatively large statistical differences in the post-weaning period. It is also important to note that the time-interval between adjacent time points varies from two days (between p0 and p2) to 40

days (between p40 and p80), and statistically significant volume changes must be interpreted with regard to the intervening growth period. We also caution researchers on comparing these results with experimental data from different rat sub-species, as small but significant anatomic differences are known to exist among commonly used laboratory strains (Boss et al., 1987). Our intention is to provide a guide for the volume differences that researchers should expect using similar methodology. We suggest that these results will help design future experiments assessing regional volume differences in disease models.

5.4.2. Voxelwise measurements of variability

Figure 13 reveals relatively constant morphometric variability in the rat brain throughout postnatal development. The average mean positional difference (MPD) across all time points was 129 μm, which is consistent with previous measurements of variability in adult rodent brains (Kovacevic et al., 2005; Badea et al., 2007a). A few regions exhibit somewhat higher variability, notably the midbrain and olfactory bulbs. The high variability of the midbrain, especially in the p2-p12 range, is also reflected in the measured volume distribution displayed in Figure 11 and Figure 12. There are at least two explanations for this increased variability. The first is that it reflects true biologic variability; the midbrain is located at a flexure in the neuraxis and experiences its most rapid growth in the early prenatal period, as evident in Figure 11. The second explanation is related to specimen preparation. Although specimens were imaged in the skull to prevent external deformation, the posterior fontanelle, which sits just above the

midbrain, does not close until after the second week of postnatal life (Moss, 1954). It is certainly possible that external deformation through the open fontanelle could be contributing to midbrain variability. We still believe that these results are meaningful as this type of error is likely to be reproduced in future studies.

6. Analysis of diffusion tensor parameter changes throughout postnatal neurodevelopment

The work presented in this chapter was published in NeuroImage in 2013 (Calabrese and Johnson, 2013).

6.1. Introduction and Background

DT-MRH has exciting potential to characterize and quantify the trajectory of postnatal microstructural changes in the brain, particularly in small animal models like the rat where this technology is relatively easy to implement. This use of DT-MRH comes with an important caveat—water diffusion in the brain is changed by cell death, fixation and ambient temperature, so ex-vivo measurements of diffusion tensor parameters are often different from in-vivo measurements (Sun et al., 2005; 2009). Further, inherent biological control of brain environment (i.e. thermoregulation, osmoregulation) is absent in ex-vivo experiments, which allows wider variability in diffusion measurements. Perhaps for these reasons, previous attempts to measure diffusion tensor parameters in the fixed rodent brains brain have yielded widely varying results (Guilfoyle et al., 2003; Verma et al., 2005; Zhang et al., 2005; 2006; Jiang and Johnson, 2011). Despite these issues, DT-MRH remains a valuable technique for studying and quantifying neurodevelopment in animal models, and well-defined normal values would allow quantitative characterization of abnormal versus normal neuro-microstructural development.

In this study, we used DT-MRH to reveal postnatal tissue microstructural changes in the developing rat brain at what we believe to be the highest spatial resolution yet attained. We have correlated the observed changes in diffusion tensor parameters with known microstructural developmental processes and compared our results to other diffusion-tensor-based studies of rat neurodevelopment. We show that with careful experimental design and data normalization, DT-MRH measurements of mean diffusivity closely resemble the trajectory, but not necessarily the magnitude, of comparable in-vivo measurements. This study establishes a database of normative changes in DT-MRH microstructural metrics that can be used as a reference for detecting and quantifying neuropathology in rat models of human neurodevelopmental disease.

6.2. Methods

6.2.1. Calculation of diffusion tensor scalars

Manually segmented brain regions were used as 3D regions-of-interest (ROIs) for analysis of diffusion tensor parameters. For each region and at each time point, we calculated the mean value of four different tensor derived scalars: mean diffusivity (MD), radial diffusivity (RD), axial diffusivity (AD) and fractional anisotropy (FA). MD is the mean of the three tensor eigenvalues: $(\lambda_1 + \lambda_2 + \lambda_3)/3$. AD is equivalent to λ_1 and RD is the average of the second and third eigenvalues, $(\lambda_2 + \lambda_3)/2$. FA was calculated as:

$$FA = \sqrt{\frac{1}{2}} \frac{\sqrt{(\lambda_1 - \lambda_2)^2 + (\lambda_2 - \lambda_3)^2 + (\lambda_3 - \lambda_1)^2}}{\sqrt{\lambda_1^2 + \lambda_2^2 + \lambda_3^2}}$$

At the reported spatial resolution it is possible for a small fraction of voxels to lie entirely within small air bubbles or fluid filled blood vessels, resulting in outlier measurements that do not represent the actual diffusion parameter of the tissue of interest. To reduce the effect of outliers we discarded the top and bottom 2.5% of voxel intensities within each region before calculating the mean. Data were then imported into JMP Pro 9 statistics software (http://www.jmp.com) for further analysis. ADC, AD and RD values were normalized based on the ADC of the ventricular space. To accomplish this normalization, we manually selected a large region of ventricular space with no visible choroid plexus and measured the average voxel value, which was assumed to represent unhindered diffusion. Each dataset was then normalized by some scalar, such that ventricular diffusion measurement matched the group average ventricular diffusion measurement. This normalization is meant to correct for diffusion measurement error induced by ambient temperature and effective b-value variability, and does not account for differences in tissue fixation. Average datasets for each time point, as well as the complete diffusion tensor scalar database, are provided online at http://www.civm.duhs.duke.edu/2013diffratbrain/.

6.2.2. Transmission electron microscopy

After fixation and MR imaging, a single specimen from each time point was further processed for transmission electron microscopy. In short, brains were

manually extracted from the skull, hemisected along the mid sagittal line, and sliced in the sagittal plane using a vibratome. Para-sagittal slices were then prepared for electron microscopy using a standard four-hour microwave processing protocol (Giberson and Demaree, 1999). Individual resin blocks were prepared for the genu of the corpus callosum, and the outer cingulate cortex of each specimen. Tissue blocks were surveyed to identify the tissue of interest, and a series of electron micrographs were acquired at 50,000x and 100,000x display magnification using a Philips CM12 transmission electron microscope. All electron microscopy work was performed at the Duke University electron microscopy facility (http://pathology.mc.duke.edu/Path/Experimental/EM/EM_Main.aspx).

6.3. Results

6.3.1. White matter regions

Figure 14 shows plots of FA versus postnatal day for six major white matter structures. Data are displayed as outlier style box-and-whisker plots with a line connecting adjacent means. All six white matter regions exhibit a similar FA trajectory during neurodevelopment; FA is generally low at birth (i.e. less than 0.3), reaches a maximum between p24 and p40, and then decreases slightly, although not significantly at p80. In all cases, the most rapid increase in FA occurs between p12 and p18. The anterior commissure and optic pathways had slightly higher mean FA than other white matter structures at the same age, ranging from ~0.3 at p0 to ~0.7 at p40. The distribution of FA measurements was

relatively consistent between time-points; however, the p18 and p80 time-points generally exhibited narrower FA distribution for the six white matter structures shown here.

Diffusivity values for the same six white matter regions are displayed in Figure 15. Axial diffusivity (AD, black), mean diffusivity (MD, dark gray), and radial diffusivity (RD, light gray) are shown on the same plot for each structure as outlier style box-and-whisker plots. As is expected for high FA structures like white matter tracts, AD was much greater than MD and RD. All six white matter regions show a similar trend; diffusivities peak around p12 and then stabilize to a minimum near p40. Once again, variability was generally larger near birth (p0) and lowest around p18. In most cases, RD values experienced a net decrease between p0 and adulthood (p80), whereas AD remained the same or slightly increased during this period (optic pathways for example).

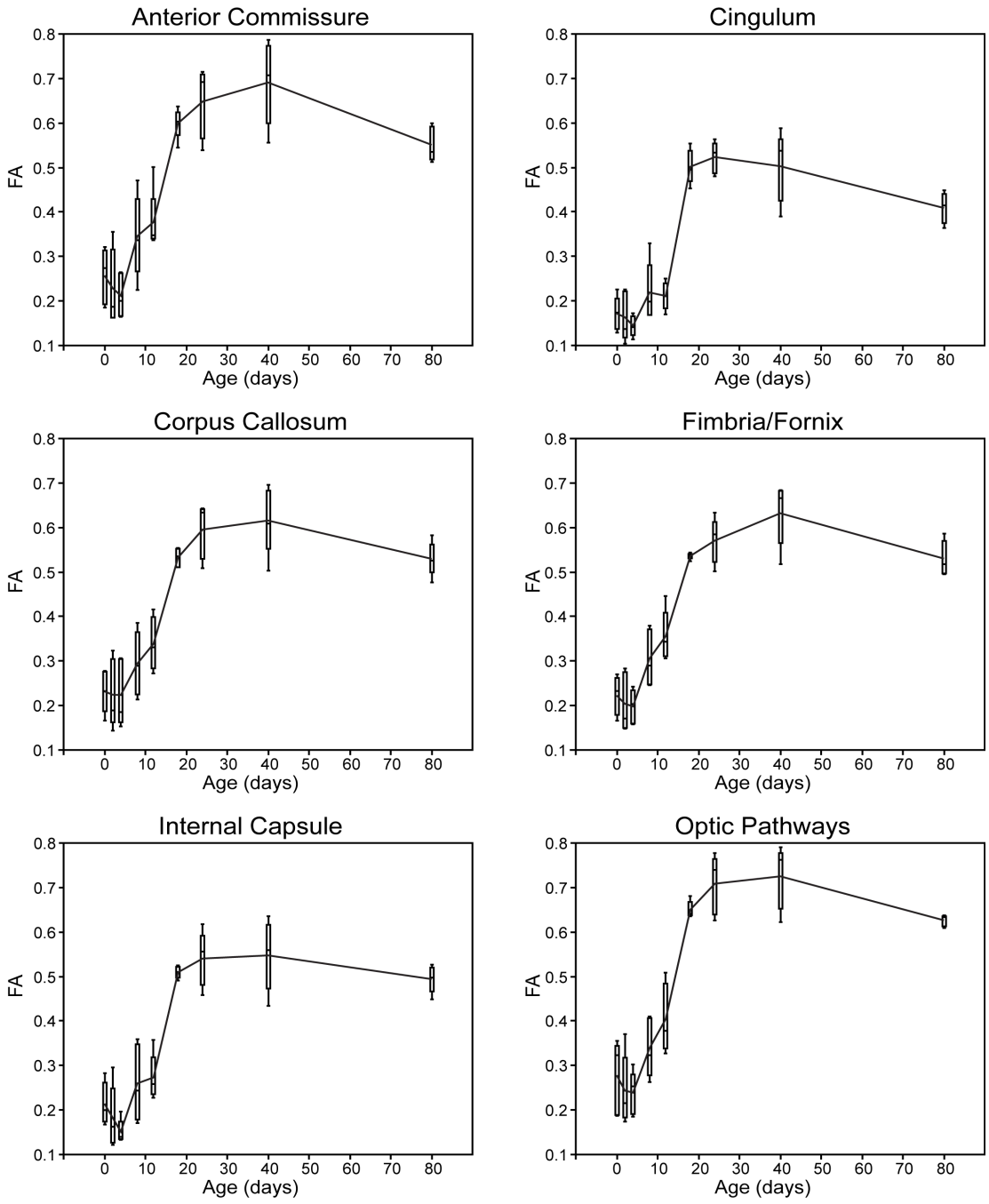

Figure 14 - Plots of fractional anisotropy (FA) versus postnatal day for six major white matter regions in the postnatal developing rat brain. Data are shown as outlier-style box-and-whisker plots with a line connecting adjacent means.

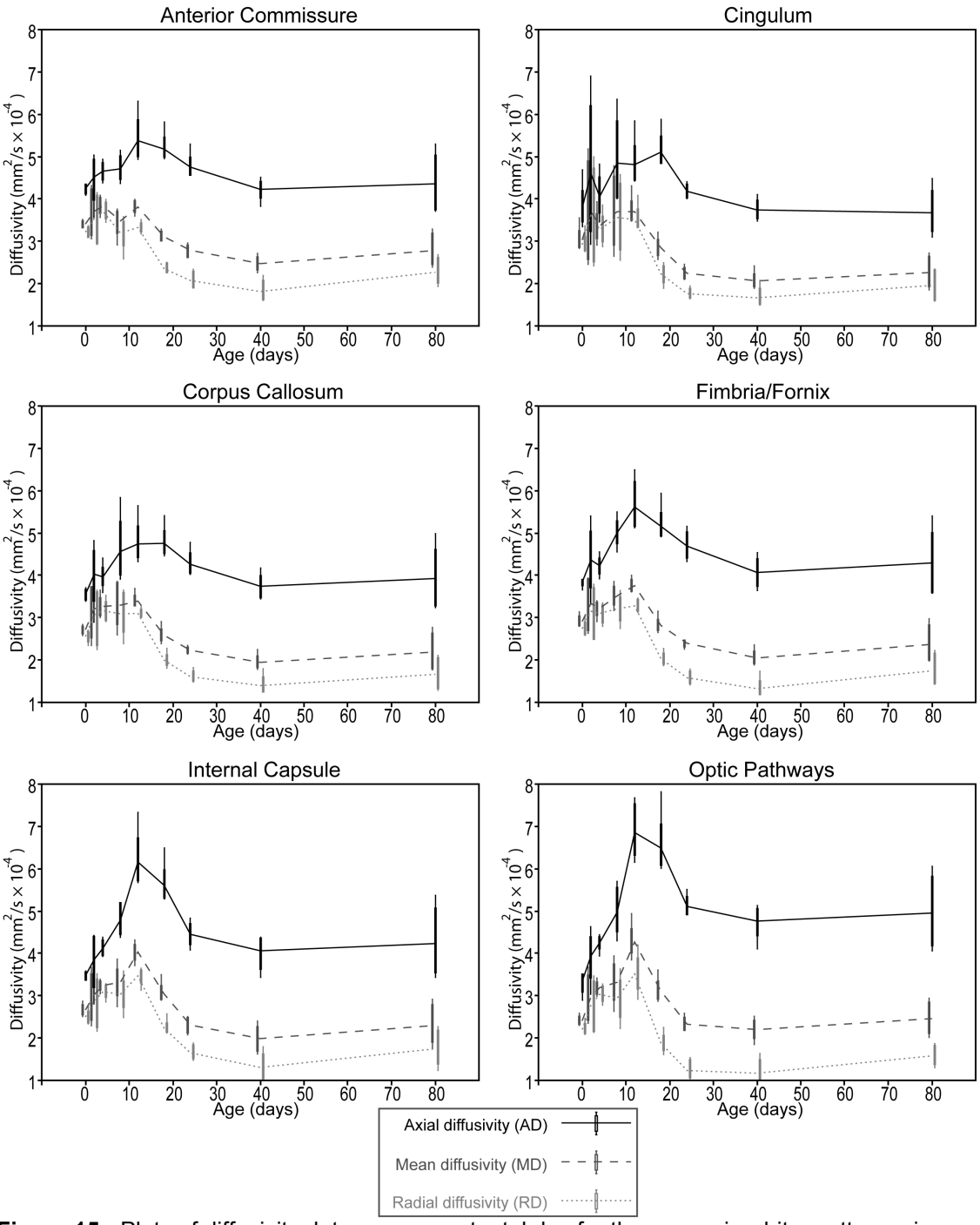

Figure 15 - Plots of diffusivity data versus postnatal day for the same six white matter regions shown in **Figure 14**. Data are shown as outlier-style box-and-whisker plots with a line connecting adjacent means. Each plot includes axial diffusivity (AD, solid black), mean diffusivity (MD, dashed dark gray), and radial diffusivity (RD, dotted light gray).

6.3.2. Gray matter regions

In contrast to the dramatic increases in FA seen in most major white matter structures, a majority of gray matter structures show no significant change in mean FA during postnatal neurodevelopment. The major exception to this trend is the superficial isocortex, which shows a remarkably high FA at birth that rapidly disappears by the 8th postnatal day. Figure 16 shows a comparison of cortical FA in a p0 (A, C, E) and p4 rat brain (B, D, F). Figure 16 A and B are FA images displayed with a heat-map lookup table to highlight differences (color map shown). The displayed slices were taken at roughly the same location in the p0 and p4 cortex, respectively; however, subcortical structures may not be coplanar between these time points due to the normal course of neurodevelopment. These data reveal high FA in the p0 isocortex that is substantially reduced by p4. Interestingly, high birth FA only occurs in the outer half of the isocortex, roughly corresponding to cortical layers I-III. Magnified insets spanning the entire cortical thickness (C and D) are displayed along with vector arrows indicating direction of the primary eigenvector and its magnitude (i.e. the axial diffusivity) at each pixel. Despite the large changes in cortical FA between p0 and p4, the orientation of the primary eigenvector remains relatively unchanged. Figure 16 E and F show the same region of cortex in grayscale along with the 3D tensor ellipsoids corresponding to each pixel. The tensor ellipsoids reveal that FA loss in the outer layers of the isocortex is primarily the result of decreasing axial diffusivity (i.e. a shortened long axis of the tensor ellipsoid).

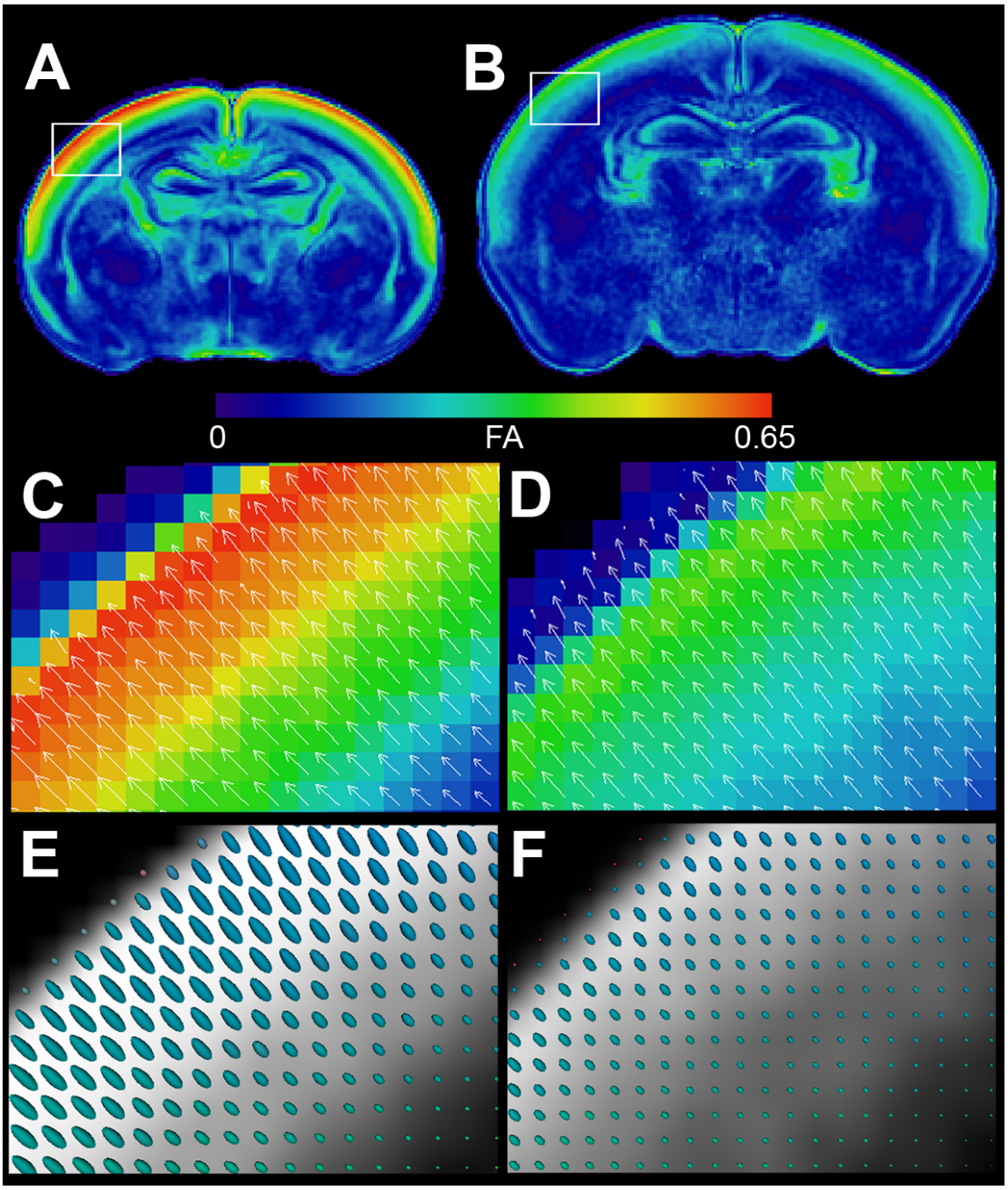

Figure 16 - Fractional anisotropy changes in the neonatal isocortex between p0 (left) and p4 (right). Coronal fractional anisotropy (FA) images through the rostral hippocampal formation from the p0 (A) and p4 (B) rat brain are shown in false color heat-map to highlight differences (scale shown). Magnified insets of the entire cortical thickness are shown with vector arrows indicating direction and magnitude of the primary eigenvector (C–D). The same regions are shown in grayscale along with the 3D tensor ellipsoids corresponding to each voxel (E–F).

We quantify these findings in Figure 17, which shows data collected from a 2D ROI placed in the outer layers of the isocortex at approximately the same location shown in Figure 16 C and D. We compared FA (left), AD, and RD (right) values for all five specimens at p0 and p4. Statistically significant differences were computed using the student's T-test. These data show a decrease in FA between p0 and p4 that is due to a large decrease in AD and a modest increase in RD. All three changes reached statistical significance.

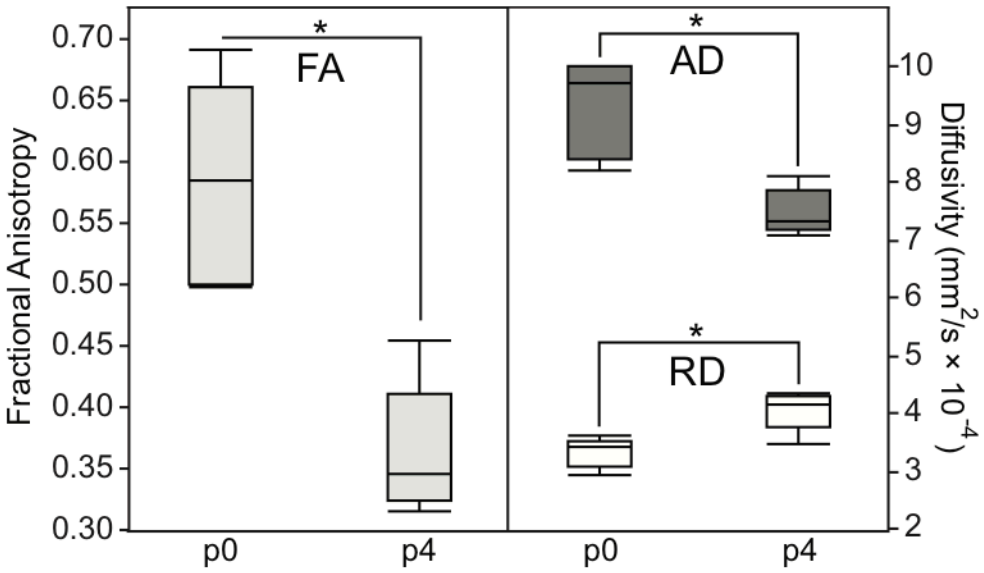

Figure 17 - Diffusion parameter measurements from a 2D region of interest placed in the outer layers of the p0 and p4 isocortex at approximately the same locations shown in **Figure 16** B–C. Fractional anisotropy (FA) is shown (left) next to axial diffusivity (AD) and radial diffusivity (RD) (right). Statistically significant changes in diffusion parameters are denoted with an asterisk.

6.3.3. Transmission electron microscopy

Figure 18 and Figure 19 show electron microscopy results from specimens previously imaged with DT-MRH. Figure 18 compares low-power (top) and high-power (bottom) images of the genu of the corpus callosum at three different postnatal time points: p0 (left), p12 (center), and p24 (right). These three

time points correspond to the beginning, middle, and end, respectively, of the period of most rapid change in callosal diffusion tensor parameters. In each image, representative axons are marked with asterisks. The p0 genu is comprised largely of widely spaced clusters of small, unmyelinated axons. The p12 genu consists of slightly larger diameter axons loosely wrapped in immature myelin lamellae with abundant periaxonal cytoplasm. In contrast, the p24 micrographs show several large diameter axons with thick, highly compact myelin sheaths. Figure 19 is a comparison of electron micrographs taken from the outer layers of the cingulate cortex in the p2 and p4 rat brain. The p2 outer cortex (left) is dominated by a complex network of radially oriented glial cell processes (marked with asterisks). This radial glia network is much less prominent in the p4 outer cortex (left) and is virtually absent in later time points.

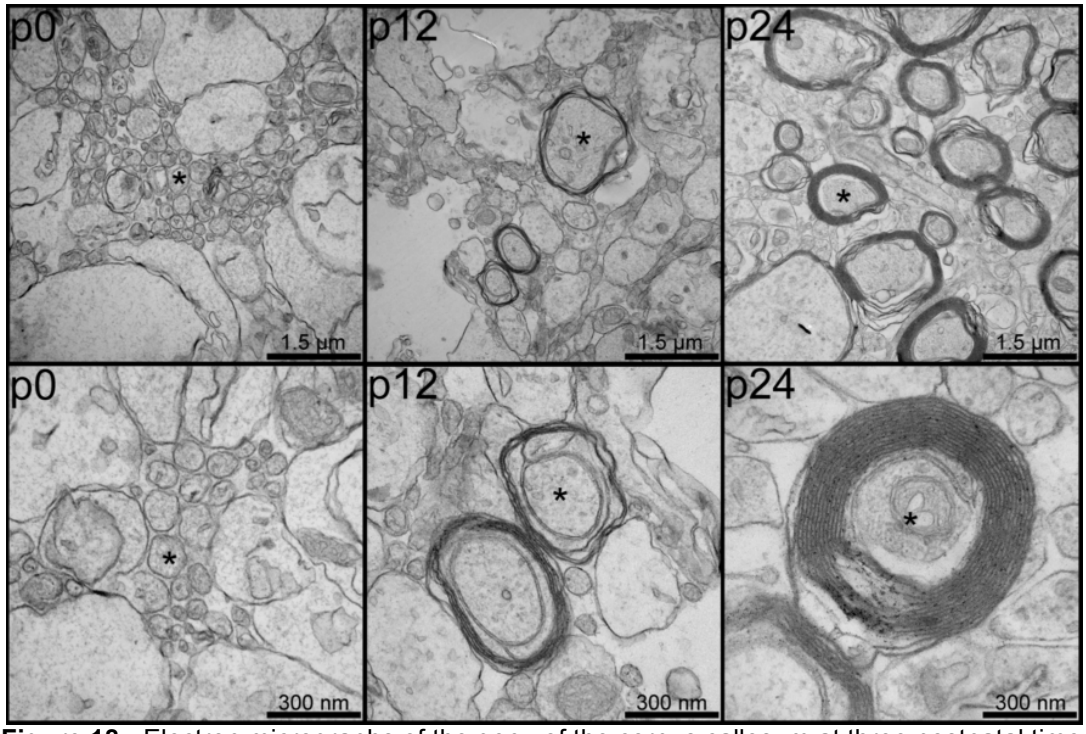

Figure 18 - Electron micrographs of the genu of the corpus callosum at three postnatal time points (p0, left; p12, center; and p24, right) demonstrating postnatal cerebral myelination. Both low power (50,000x magnification, top) and high-power (100,000x magnification, bottom) are shown for each time point. Representative axons are marked with asterisks and scale bars are shown in the bottom right corner of each image.

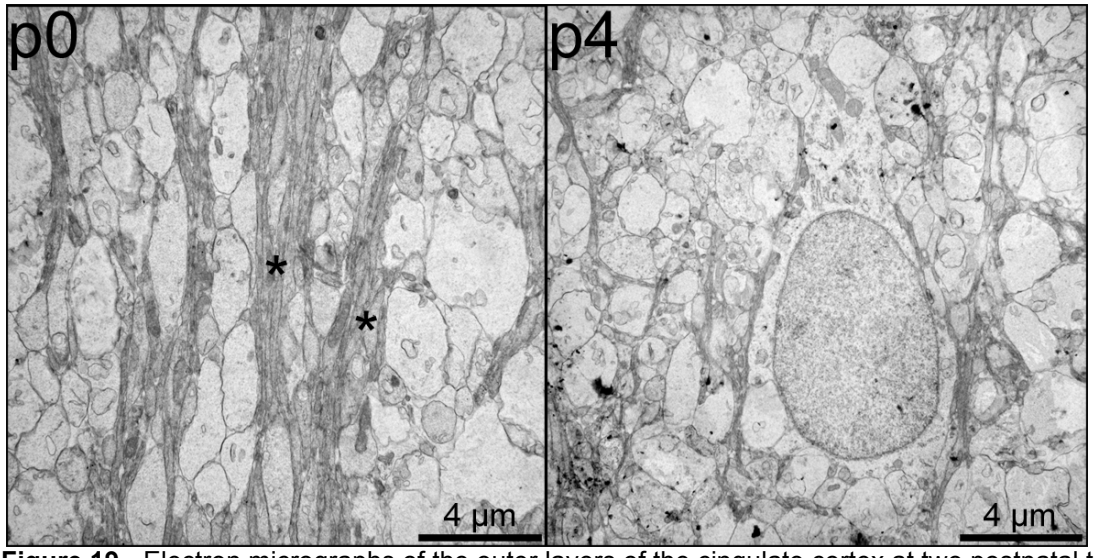

Figure 19 - Electron micrographs of the outer layers of the cingulate cortex at two postnatal time points (p0, left; and p4, center) demonstrating differences in radial glial cell processes. Bundles of radial glial cell processes are marked with asterisks and scale bars are shown in the bottom right corner of each image.

6.4. Discussion

6.4.1. Diffusion tensor changes reveal white matter maturation

A majority of white matter myelination in the rodent brain occurs during the early postnatal period, and the myelination process is virtually complete by the third postnatal week (Foran and Peterson, 1992). FA is a sensitive (though not specific) imaging biomarker for axonal organization and myelin integrity. The diffusion data collected for this study reveal dramatic microstructural changes during early postnatal development that correlate, both spatially and temporally, with known white matter maturation milestones. For example, FA data from six major cerebral white matter regions (Figure 14) follow a trajectory that is consistent with cerebral myelin maturation. Gene transcription and electron microscopy studies have shown that rodent brain myelination starts by the end of the first week of postnatal life and is largely complete by the end of the third postnatal week (Luse, 1956; Field et al., 1969; Foran and Peterson, 1992). Similarly, all six plots of FA versus postnatal day shown in Figure 14 have positive slope between p8 and p24. Further, the most rapid increase in FA occurs between p12 and p18, which is believed to be the period of most rapid myelination in the rodent brain.

One of the major advantages of diffusion tensor measurements over conventional histologic methods for assessing white matter maturation is that they can be easily quantified. The quantitative nature of this FA data allows it to be used for quantifying developmental neuropathology in rodent models. Unfortunately, one of the major shortcomings of FA is the fact that it is

nonspecific, and is at best a surrogate for myelin integrity. FA is in essence a normalized ratio of water diffusion in one direction to its diffusion the two orthogonal directions (Basser and Pierpaoli, 1996). Many microstructural features can lead to increasing diffusion anisotropy in white matter including; 1) decreased RD from myelination, myelin compaction or the compaction of many axons into a nerve fascicle; 2) increased AD from a reduction in axonal swelling or an increase in inter-axon extracellular space; or 3) a combination of decreased RD and increased AD (Basser, 1995; Mukherjee et al., 2008). Careful analysis of the diffusivity values used to calculate FA, including AD, MD, and RD can reveal further details about underlying tissue changes.

Measurement of diffusion via DT-MRH is inherently problematic because fixation alters tissue diffusivity (Sun et al., 2009). Fortunately, if performed carefully, perfusion fixation produces a spatially and temporally consistent reduction in tissue diffusion that appears to be proportional to in-vivo diffusivity, thus reducing diffusion magnitude but not directionality or proportionality (Sun et al., 2005). Another concern is that ex-vivo tissue does not have any inherent thermoregulation or osmoregulation, which can lead to a spuriously wide inter-specimen data distribution due to subtle changes in perfusate osmolality or magnet bore temperature. This effect can be corrected for by normalizing to a substance of known diffusivity, such as a diffusion phantom, or if image resolution permits, to the ventricular fluid as was done for this study.

Figure 15 shows normalized diffusivity data plotted against age in postnatal days for the same six white matter structures as Figure 14. One of the

most striking similarities in these plots is the increase in all three diffusivity parameters that occurs around p12 in all six structures. Interestingly, this diffusivity increase coincides temporally with the start of a rapid increase in FA. Several previous in-vivo studies of rodent white matter diffusivity have shown a similar increase in white matter diffusivity during the second postnatal week followed by a decline and stabilization after the third postnatal week (Chahboune et al., 2007; Larvaron et al., 2007; Bockhorst et al., 2008). Specifically, Bockhorst et al. (2008) showed a similar trend in the corpus callosum and internal capsule, Chahbourne et al. (2007) in the corpus callosum and cingulum and Larvaron et al. (2007) in the corpus callosum and anterior commissure. All three groups reported in-vivo MD change in the corpus callosum from ~0.8×10^{-3} mm^2/s to ~0.5×10^{-3} mm^2/s during the course of postnatal neurodevelopment, representing a ~37% decrease with age. Our ex-vivo results show corpus callosum MD change from $0.35\pm0.02\times10^{-3}$ mm^2/s to $0.23\pm0.04\times10^{-3}$ mm^2/s, or a 34% decrease during this period. These results indicate that normalized DT-MRH measurements of diffusivity closely match the trajectory and proportionality of comparable in-vivo measurements, though not necessarily the magnitude.

Together, the estimates of white matter diffusion parameters shown in Figure 14 and Figure 15 reveal complex changes in underlying tissue microstructure. The data show a large, but transient, increase in diffusivity around p12 followed by a rapid increase in FA between p12 and adulthood. These diffusivity trends correlate well with previously published microstructural observations in developing white matter (Field et al., 1969) and with the electron

microscopy findings presented in Figure 18. Axons in the p0 corpus callosum (Figure 18, left) are predominantly unmyelinated, presumably contributing to the low FA observed in p0 DT-MRH data. The p12 corpus callosum (Figure 18, center) has many myelinated axons; however, the myelin lamellae are immature and have large areas of periaxonal cytoplasm. This excess of periaxonal cytoplasm, where diffusion is relatively unhindered, may be the cause of increasing white matter diffusivity values in the context of rapid cerebral myelination. In contrast, axons in the p24 corpus callosum (Figure 18, right) are tightly ensheathed in mature myelin lamellae with very little periaxonal cytoplasm, resulting in relatively low diffusivity and high FA. These data suggest that both the degree of myelination, and the compactness of the myelin layers contribute to diffusion tensor changes during normal neurodevelopment. Despite their lack of specificity, it is clear that diffusion parameters like FA and RD are sensitive, quantitative biomarkers for the range of microstructural changes that occur during normal white matter development.

6.4.2. Diffusion tensor changes in the developing cerebral cortex

As previously explained, diffusion tensor parameters are not specific for white matter integrity, but rather reflect tissue microstructural organization. In fact, dramatic diffusion tensor changes occur in the developing cerebral cortex as shown in Figure 16 and Figure 17. At birth, the outer layers of the rat isocortex have a remarkably high FA—even higher than major cerebral white matter structures (e.g. Figure 16 A). Interestingly this high cortical anisotropy rapidly

decreases and is virtually absent by p8. This rapid change in cortical microstructure is characterized by decreasing diffusion anisotropy in the presence of an unchanged primary eigenvector (Figure 16 C-F). The statistical analysis presented in Figure 17 points to a decrease in AD and a proportionally smaller increase in RD as the cause of this early postnatal, cortical anisotropy loss. These diffusion changes in the presence of an unchanged primary eigenvector suggest the loss of a radially organized diffusion pathway in the outer cortex during early postnatal life.

It is likely that several different microstructural processes contribute to the observed FA changes in the developing rat cortex. For example, a number of white matter pathways radiate outwards towards the cortical surface; however, they tend to become more organized, rather than less organized during neurodevelopment (Wise and Jones, 1976; Allendoerfer and Shatz, 1994). In addition, the radial migration of cortical neurons and the later development of cortical interneurons (Noctor et al., 2004) could conceivably alter diffusion properties along the cortical column. Perhaps the major contributor to the observed changes is the disruption of a radially organized network of glial cells that is known to occur during early cortical development (Chanas-Sacre et al., 2000). This highly ordered scaffolding of glial cell processes, often referred to as “radial glia,” provides a pathway for migration of neurons and neuronal precursor cells what will eventually become the six layers of the cerebral cortex (Rakic, 1972). Because of its important organizational role in the developing cortex, damage to the radial glia, as a result of perinatal asphyxia for example, can lead

to severe cortical malformation and neurologic disability (Marín-Padilla, 1996). The presence of radial glial cell processes on transmission electron micrographs correlated well with FA changes in the developing neonatal isocortex; we observed an abundance of radial glial cell processes in the p0 outer cortex (Figure 19, left), which was substantially reduced in the p4 outer cortex (Figure 19, right). The ability to quantify spatial and temporal changes in cortical microstructure has exciting potential to advance our understanding of diseases that may be the result of perinatal cortical insults such as hypoxic ischemic encephalopathy or cerebral palsy. For example, perinatal hypoxic ischemic injury has been shown to significantly reduce FA and alter the radial organization of the primary eigenvector in the neonatal rat cerebral cortex (Sizonenko et al., 2007).

These data emphasize that DT-MRH data can be used to quantify microstructural changes in both white matter and gray matter structures. In total, the diffusion parameter database generated from this study comprises 26 distinct brain regions, most of which are at least partially composed of gray matter. In each case, the postnatal trajectory of diffusion tensor changes has the potential to reveal some nuance of brain microstructural development, although an in-depth analysis of each region is beyond the scope of the current study. The entire diffusion parameter database is included in the online supplement (http://www.civm.duhs.duke.edu/2013diffratbrain/) for further analyses.

7. Investigating the tradeoffs between spatial resolution and diffusion sampling for brain mapping with diffusion tractography: Time well spent?

The work presented in this chapter was submitted for publication in Human Brain mapping in 2014.

7.1. Introduction and background

Although DT-MRH has been most widely used for studying small animal models, it is possible to use the technique to study larger and more complex mammalian brains, including those of primates. Aside from the technical challenges of scanning larger specimens at high spatial-resolution, there is also considerable concern about the validity of diffusion modeling in brains with complex white matter architecture. Specifically, the diffusion tensor model assumes a single diffusion pathway per image voxel, which is not valid in the case of intravoxel fiber crossing, kissing or bending. Such complex fiber geometries are more likely to be present in more complex mammalian brains, like those of non-human primates. If not accounted for, these geometries can present major problems for generating anatomically accurate tractography maps. A deeper understanding of this problem is necessary before DT-MRH can be reliably used to map white matter connections in larger and more complex mammalian brains.

Mapping white matter connections in the brain has been a major goal of neuroscientists over the last century. Interest in the so-called “connectome” has

peaked recently with the realization that aberrant brain connectivity is involved in a variety of neurologic and psychiatric diseases (Sundaram et al., 2008; Lo et al., 2010; Skudlarski et al., 2010). In the past, a variety of techniques have been used to map white matter pathways in the human brain, including gross brain dissections, myelin-stained histology (e.g., silver staining, Luxol fast blue), and, more recently, anterograde/retrograde tracer studies and autoradiography (Schmahmann and Pandya, 2009). Rather than replacing its predecessor, each of these techniques has contributed a valuable new perspective to our overall understanding of white matter architecture in the brain. Despite their many merits, one major shortcoming of previous techniques is that they are all inherently destructive to the tissue and do not allow direct visualization of 3D spatial relationships.

Diffusion tractography, one of the newest additions to the white matter mapping initiative, has the potential to non-invasively and non-destructively map the entire connectome at once (Mori et al., 1999); however, this technique, like its predecessors, is not without limitations. Diffusion tractography is susceptible to many types of error that can call its anatomic validity into question (Lazar and Alexander, 2003). Particularly concerning is the fact that there are many different diffusion tractography imaging protocols, each of which yields different results. Despite these shortcomings, diffusion tractography is being employed more routinely in clinical practice (Berman et al., 2004; Yu et al., 2005), and is already changing our understanding of white matter architecture in the brain (Wedeen et al., 2012). It is clear that there is something to be gained from diffusion

tractography, but further exploration of the consequences of selecting different diffusion acquisition strategies is needed.

The accuracy of any diffusion tractography method depends on its ability to estimate underlying axonal orientation from discrete measurements of tissue diffusion made with MRI. A major limitation of diffusion tractography is that it is impractical to completely measure the 3D diffusion properties of the brain, so some limited measurement must be used. Diffusion MRI measures tissue diffusion in the spatial domain (i.e., at each image voxel) and in the diffusion domain (often referred to as q-space) (Callaghan et al., 1988). Increased spatial sampling is achieved with higher resolution imaging, and increased q-space sampling is achieved by measuring more diffusion angles, and/or more b-values. Both spatial sampling and diffusion sampling consume acquisition time, so realizable diffusion experiments must strike a compromise between the two.

Fortunately, high spatial sampling *and* high q-space sampling are usually not required for reconstructing accurate fiber tracks, and there is often a tradeoff between the two (Jahanshad et al., 2010; Zhan et al., 2012a; 2012b). Increased spatial sampling can *reduce* intravoxel fiber complexity, while increased q-space sampling can *resolve* intravoxel fiber complexity (Tuch et al., 2002; Kim et al., 2006). At very high (theoretical) resolution, where each voxel contains only a single coherent bundle of axons, fiber orientation can be estimated with the diffusion tensor (DTI) model, which fits as few as seven q-space measurements to single rank-2 tensor. In this theoretical case, DTI yields equivalent results to more complex q-space sampling schemes (Basser, 2002; Yamamoto et al.,

2007). Larger (and more realistic) imaging voxels are likely to contain some degree of fiber complexity. Complex intravoxel architecture, such as fiber crossing can be resolved with increased q-space sampling. Depending on the sampling pattern, additional q-space data can be fit to higher order diffusion models as in spherical harmonic deconvolution, or can be used for model-free estimation methods like diffusion spectrum imaging (DSI). Importantly, some intravoxel fiber architectures, like interdigitating crossing, can only be resolved with higher q-space sampling, and others like bending or kissing fibers can only be resolved with higher spatial resolution (Basser et al., 2000; Tuch et al., 2003). The degree to which these complex geometries exist in the human brain is still debated (Catani et al., 2012; Wedeen et al., 2012; Jeurissen et al., 2013).

The tradeoff between simplifying intravoxel fiber architecture with image resolution, and resolving it with q-space sampling presents an interesting problem: if the goal is anatomically accurate tractography, is it better to spend scan time on increased spatial resolution or increased q-space sampling? Further, in the range of currently feasible imaging voxels and q-space sampling schemes, is there some optimal combination for producing accurate tractography in the human brain? These questions are particularly relevant for brain mapping initiatives, such as the various connectome projects, where advanced imaging protocols are commonly used, and anatomic accuracy is essential (Sporns et al., 2005). In this study, we explore these questions with a combination of computer simulations and *ex vivo* imaging of the nonhuman primate brain. The rhesus macaque brain can serve as a close model of the human brain, particularly with

regard to white matter architecture and complexity. The rhesus brain also has a large body of autoradiography-based structural connectivity data that are simply impractical to acquire in human subjects. In this study, we use this wealth of autoradiographic data to analyze the anatomic accuracy and consistency of tractography results from six time-matched diffusion imaging protocols, varying the balance between spatial resolution and q-space sampling.

7.2. Methods

7.2.1. Diffusion tractography simulations

Computer simulations were carried out in MATLAB to interrogate the effects of varying spatial and angular resolution diffusion imaging on tractography. We generated two 1 cm × 1 cm digital fiber phantoms, a circularly curved fiber phantom with thickness 0.5 cm (radius 0.5 cm - 1 cm) and an intravoxel crossing fiber phantom consisting of the same circular curve and a 3.5 mm thick diagonal crossing bundle (crossing angle 60° - 90°). Noiseless diffusion weighted image sets were simulated for each of five different gradient schemes (12 – 120 directions) at 1 μm resolution using a multiple gaussian diffusion model as described in previous work (Barmpoutis et al., 2009). Images were then downsampled to reflect varying isotropic acquisition resolutions (0.5 mm – 0.1 mm) and corrupted with Rician noise to yield a b0 signal-to-noise ratio (SNR) of 30 in all cases. Diffusion dataset reconstruction and tracking were performed as described later in this section.

7.2.2. Brain specimens

Two fixed rhesus macaque brains were obtained from the Wisconsin National Primate Research Center at the University of Wisconsin-Madison. The brain specimens were from adult animals that were euthanized humanely by veterinary staff for non-neurological reasons. Following necropsy and tissue extraction by a trained pathologist, the brains were immersed in 10% neutral buffered formalin doped with 1% (5 mM) gadoteridol (ProHance, Bracco Diagnostics, Milan, Italy). Three weeks prior to imaging, specimens were transferred to a 0.1 M solution of phosphate buffered saline doped with 0.5% (2.5 mM) gadoteridol. Immediately prior to imaging, specimens were placed in custom-made MRI-compatible tubes and immersed in Galden low viscosity perfluoropolyether for susceptibility matching and to prevent specimen dehydration (Solvay Plastics, Brussels, Belgium).

7.2.3. MR imaging

Imaging was performed on a 7 Tesla small animal MRI system (Magnex Scientific, Yarnton, Oxford, UK) equipped with 650 mT/m Resonance Research gradient coils (Resonance Research, Inc., Billerica, MA, USA), and controlled with an Agilent Direct Drive console (Agilent Technologies, Santa Clara, CA). RF transmission and reception were achieved with a 65 mm inner-diameter quadrature RF coil (M2M Imaging, Cleveland, OH). Brain specimens were imaged using each of six time-matched q-space sampling schemes. Each scheme was realized with a 3D spin-echo pulse sequence. Repetition time was

held constant at 100 ms to ensure that regardless of the acquisition protocol, a single line of 3D k-space was acquired per TR. Diffusion preparation was accomplished using a pair of unipolar, half-sine diffusion gradient waveforms. The range of acquisition parameters included spatial resolution from 0.13 mm to 0.6 mm isotropic, angular sampling from 12 to 257 directions, and b-value sampling from one to 22 b-values. One b0 volume was collected for each protocol. Scan time was held constant at 60 hours ± 5%. The details of each acquisition strategy are provided in Table 7. For the two DSI schemes, b-values were evenly spaced between a minimum of 2,000 s/mm^2 and a maximum of 10,000 s/mm^2. Complete diffusion datasets and gradient tables from all six protocols are available in the online supplementary material (http://http://www.civm.duhs.duke.edu/2013_macaque_tractography/). In addition to diffusion datasets, a single high-resolution (50 μm isotropic) anatomic image volume was acquired using a 3D gradient echo pulse sequence (TR/TE = 50 ms/7.2 ms).

7.2.4. Diffusion data reconstruction and tractography

Diffusion data were reconstructed in Diffusion Toolkit (http://trackvis.org) using the most appropriate algorithm for the chosen q-space sampling scheme. The twelve direction scheme (DTI-12) was reconstructed using a single-tensor least-squares estimation (Basser and Pierpaoli, 1996). The 30, 60 and 120 direction schemes (QBI-30, QBI-60 and QBI-120 respectively) were reconstructed with Q-ball spherical harmonic deconvolution (Hess et al., 2006;

Descoteaux et al., 2007). The two multi-b-value schemes, DSI-127 and DSI-257, were reconstructed using the DSI Fourier transform approach (Wedeen et al., 2005).

Whole-brain diffusion tractography was carried out in Diffusion Toolkit (http://trackvis.org) using the FACT (for DTI) or FACT-like (for Q-ball and DSI) tracking algorithm (Mori et al., 1999). Tracking parameters included an intravoxel turning angle threshold of < 30° and a length threshold of > 5 mm. We chose not to use a fractional anisotropy threshold to facilitate tractography comparisons across different reconstruction methods. Tracks were spline filtered using a one-voxel step length to smooth tracts and eliminate improbable tract geometry.

7.2.5. Primate brain track segmentation

We conducted tractography on four “simple” and four “complex” fiber pathways in the primate brain. Simple fiber pathways included the anterior commissure (AC), the cingulum bundle (CB), the corticospinal tracts (CT), and the optic tracts (OT). These pathways have relatively simple anatomy with minimal fiber crossings, and are commonly assessed in diffusion tractography studies. Complex pathways included the extreme capsule (EmC), the inferior longitudinal fasciculus (ILF), the middle longitudinal fasciculus (MdLF), and the uncinate fasciculus (UF). These long cortical association pathways have a more complex anatomy with frequent fiber crossings and are known to be difficult to reconstruct with tractography (Schmahmann et al., 2007). Segmentation was

achieved by placing a single ROI disc in the anatomic center of the fiber pathway and accepting only tracks passing through the disc at angles less than 30°. In some cases obvious stray fibers were manually removed.

7.2.6. Tract-based comparisons with known anatomy

Unfortunately there is no universally accepted anatomic “gold standard” for mapping axonal projections in the primate brain, particularly in 3D. This lack of a “gold standard” highlights both the difficulty in validating diffusion tractography, and the scientific need to do so. There is, however, a large collection of autoradiographic connectivity data on the primate brain (Schmahmann and Pandya, 2009). Autoradiographic connectivity data are not ideal for comparison because they lack a 3D picture of white matter structure; however, they do provide true axonal connectivity. We preformed qualitative comparisons between known anatomy, as defined by autoradiography, and the six diffusion tractography datasets generated for this study. Tract similarity was evaluated based on length, course, and branching pattern.

7.2.7. Quantitative comparisons between tractography datasets

In addition to qualitative comparisons with known anatomy, we also performed quantitative comparisons between tractography datasets. Maximum, and average track length, as well as total track volume, were recorded for each dataset. Differences between tractography datasets were further evaluated using track density images (TDIs). TDIs were generated for each tractography dataset at 130 μm isotropic resolution and were normalized to the unsigned 8-bit range to

allow direct comparison between protocols. For each white matter pathway included in the analysis, a mean TDI was generated by averaging TDIs from all six acquisition protocols. Individual TDIs were then compared to the average using normalized cross correlation. This comparison did not assess anatomic accuracy directly, but rather assessed consistency between different tractography datasets.

7.3. Results

7.3.1. Tractography simulations

We first used tractography simulations (Figure 20 and Figure 21) to determine the effects of varying angular and spatial resolution on diffusion tractography. Simulated fiber tracts are colored on the basis of the angle of the line defined by the two endpoints of each track relative to vertical, where green specifies 0° and red specifies 90°. Both phantoms were designed such that the line connecting the endpoints of all fibers was at a 45° angle relative to vertical; thus, all correct tracks should appear yellow (equal parts red and green in RGB color space). Note that track density merely reflects spatial resolution because the tracking algorithm seeds the center of each voxel.

The curve phantom (Figure 20) represents a relatively simple tractography target. There are two major tractography errors evident in these simulations. First, low spatial resolution datasets (left side of figure) yielded several short and prematurely terminating tracks near the edges of the fiber bundle. These errors are likely the result of partial volume averaging, as they are present in all angular

sampling schemes and are diminished at higher spatial resolution. Second, the combination of high spatial and low angular resolution (i.e., bottom right of figure) caused virtually all tracks to terminate prematurely. Increasing angular resolution, or decreasing spatial resolution, yielded a lower proportion of prematurely terminating tracks. This effect is likely the result of minor errors in the primary fiber orientation that accumulate as the propagating tractography streamline passes through multiple voxels (Lazar and Alexander, 2003).

The crossing phantom (Figure 21) shows a similar pattern of premature fiber termination on the edges of fiber bundles, particularly in lower spatial resolution datasets. The fiber crossing was relatively well resolved in all datasets except the 12 and 30-angle datasets. The 30-angle datasets had only minor errors that caused tracks to prematurely terminate within the crossing region. These errors were more apparent at higher spatial resolutions, presumably because there are simply more voxels within the crossing region at higher resolution. The 12-angle dataset suffered from both premature termination and erroneous turning in the crossing region, and these errors were present at all spatial resolutions. It is important to note that the 12-angle datasets were reconstructed as a tensor, so resolving more than a single fiber population per voxel is not possible. Nonetheless, the 12-angle sampling scheme was included in the crossing phantom analysis for completeness and to demonstrate the type of errors that occur when tensor reconstruction is used on complex fiber geometry.

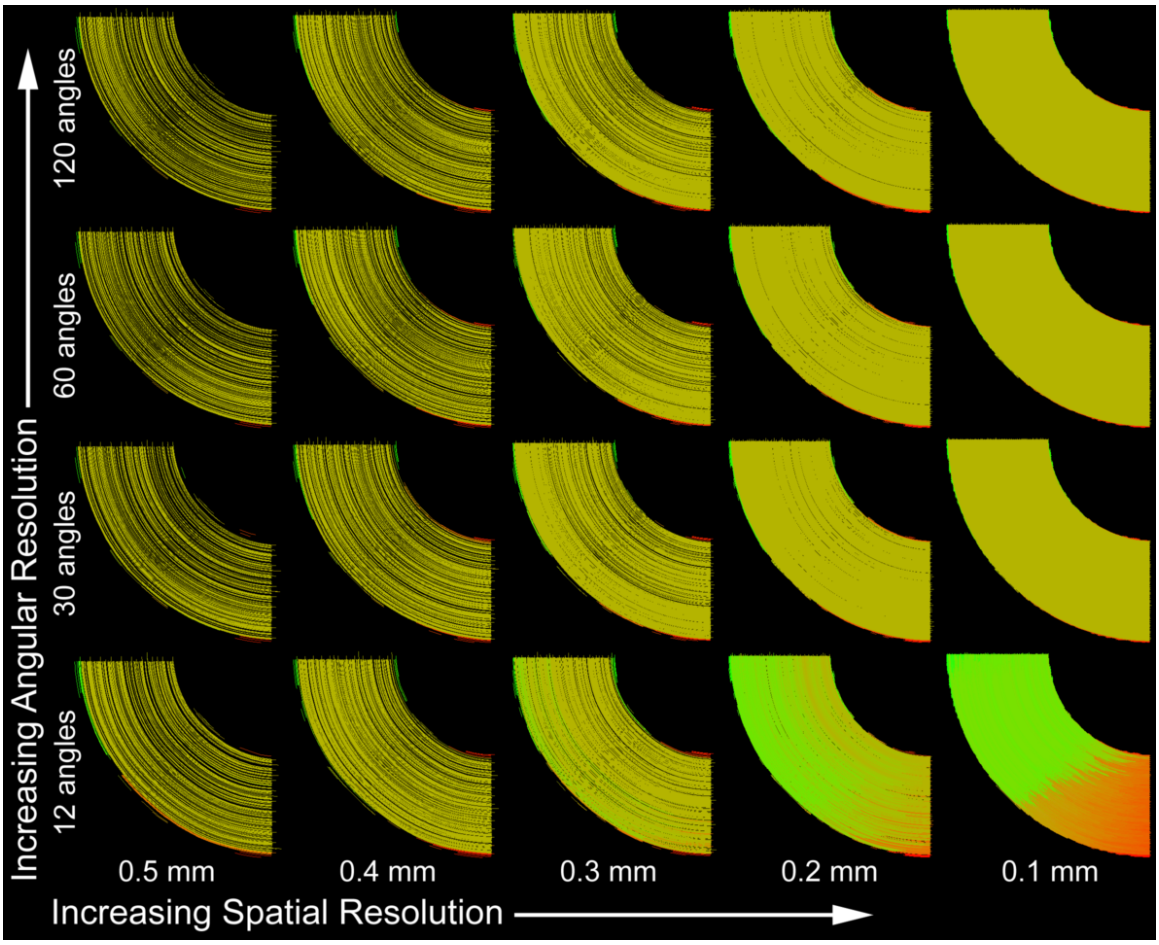

Figure 20 - Curved fiber phantom tractography simulations showing the effects of varying angular and spatial resolution. Each track is colored based on the angle of the line connecting its endpoints relative to vertical, with red = 90° and green = 0°. The phantom was designed such that the line connecting the endpoints of each fiber is at 45° relative to vertical, thus correct tracks appear yellow (equal parts red and green in RGB color space).

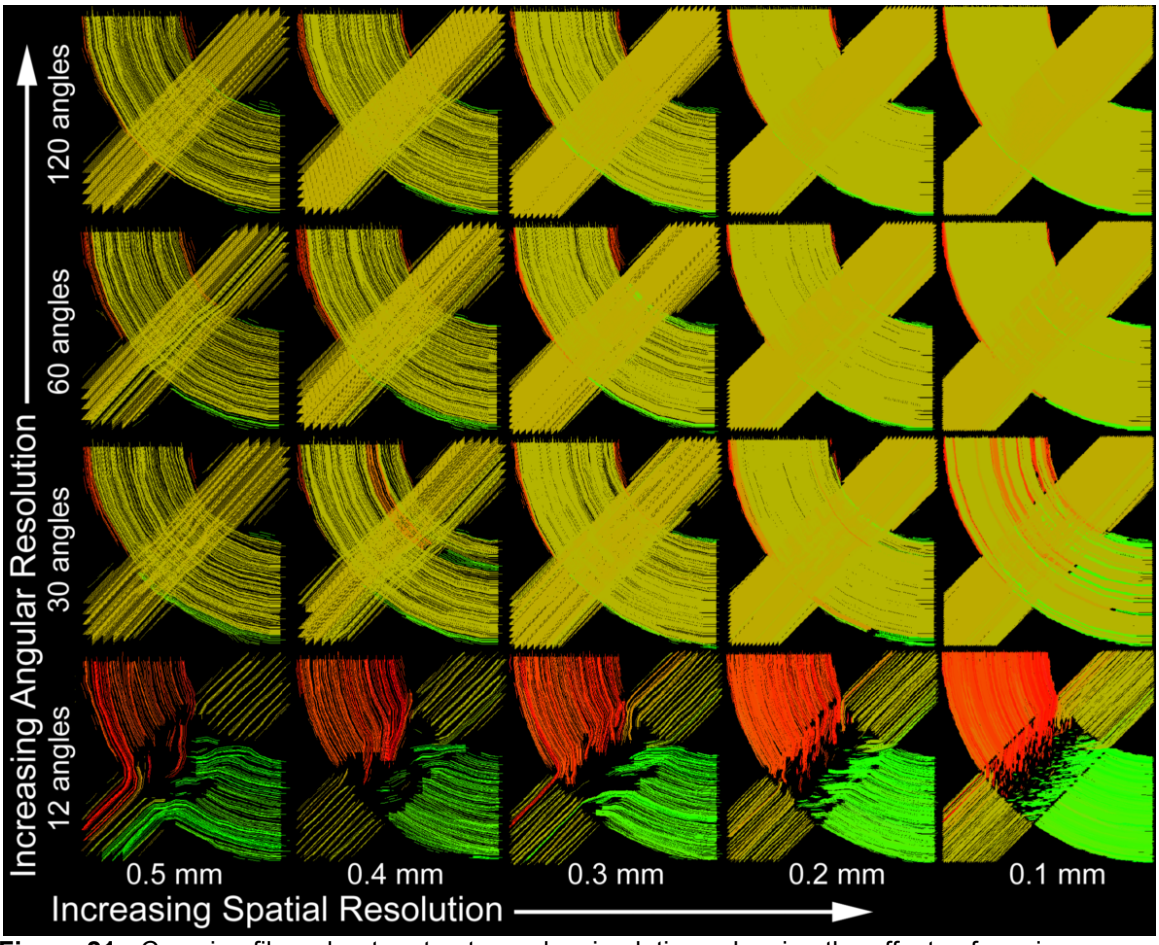

Figure 21 - Crossing fiber phantom tractography simulations showing the effects of varying angular and spatial resolution. Crossing angle varies from 60° to 90° within the phantom. Each track is colored based on the angle of the line connecting its endpoints relative to vertical, with red = 90° and green = 0°. The phantom was designed such that the line connecting the endpoints of each fiber is at 45° relative to vertical, thus correct tracks appear yellow (equal parts red and green in RGB color space).

7.3.2. Ex-vivo primate brain imaging schemes

The six time-matched q-space sampling schemes used for this *ex vivo* macaque tractography analysis are described more completely in Table 7 and Figure 22. Table 7 lists all of the relevant acquisition parameters for each protocol as well as the SNR for the b0 and maximum diffusion weighted image (bmax). SNR was measured in a single cortical region-of-interest (ROI). In all cases, SNR was in excess of general recommendations for the respective q-

space sampling scheme (Tuch, 2004; Wedeen et al., 2005; Hess et al., 2006; Descoteaux et al., 2007; Farrell et al., 2007). Figure 22 highlights the sampling differences between protocols in both the spatial and q-space domains. Higher spatial resolution was achieved at the cost of decreased q-space sampling and vice versa such that the scan time remained constant between protocols. Partial volume effects at gray matter and white matter borders are readily apparent in the lower spatial resolution schemes and are virtually absent in the higher resolution DTI-12 scheme. Additionally, there are minor variations in the image contrast due to echo time differences between the different protocols.

Table 7 - Acquisition details for the six diffusion imaging protocols used in this study.

Name	DTI-12	QBI-30	QBI-60	QBI-120	DSI-124	DSI-257
# Directions	12	30	60	120	124	257
# b-values	1	1	1	1	13	22
Isotropic res. (mm)	0.13	0.2	0.3	0.4	0.4	0.6
Max b-value (s/mm^2)	1,500	4,000	4,000	4,000	10,000	10,000
δ (ms)	4	4.7	4.7	4.7	44.9	44.9
Δ (ms)	14	26	26	26	5.2	5.2
TE (ms)	21.9	32.1	32.1	32.1	51.4	51.4
Acquisition matrix	590×444×394	384×288×256	256×192×176	192×144×128	192×144×128	128×96×88
b0 SNR	62	60	96	131	65	127
bmax SNR	48	38	50	58	17	30

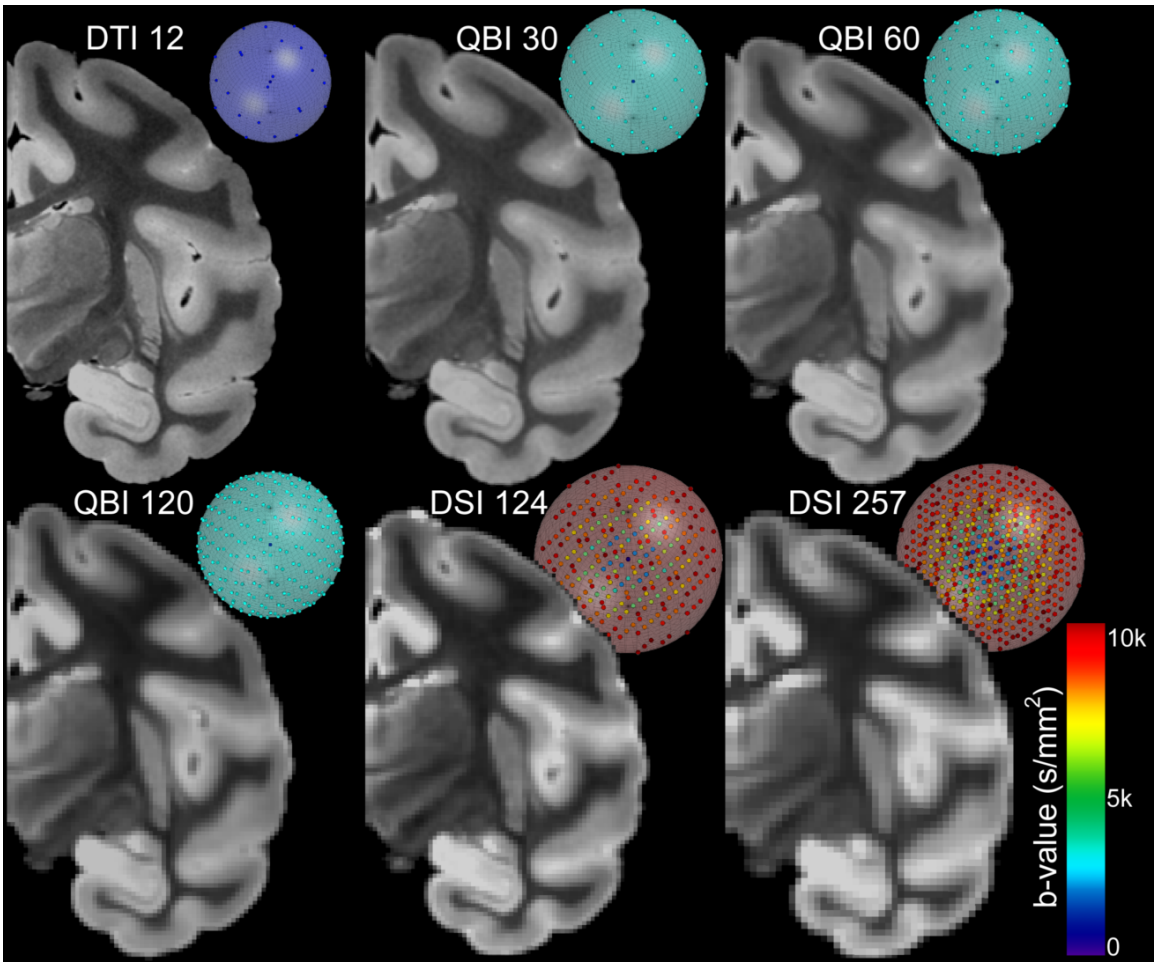

Figure 22 - Visualization of spatial sampling and q-space sampling in each of the six time-matched diffusion MRI protocols used in this study. For each protocol, the left half of a single coronal slice from the b0 image is shown along with a diagram of the q-space sampling scheme. The color (see legend) and radius of each q-space diagram indicates b-value, and each point represents a single measurement in q-space.

7.3.3. Ex-vivo primate tractography results

The following sections and corresponding figures (Figure 23 - Figure 30) present a comparison of tractography results from the time-matched diffusion sampling protocols described in Table 7. In each case, directionally colored tractography images from all six protocols are displayed side by side along with a single slice from the corresponding b0 image. Slice location is indicated in the top left corner of each figure with a plane intersecting a 3D surface rendering of the

macaque brain. The relevant diagrams from an autoradiography-based fiber pathway atlas are included for anatomic reference (Schmahmann and Pandya, 2009). Autoradiography diagrams were not available for AC, CT, and OT, so high-resolution anatomic images are displayed instead. Additional views of all tracks are included as supplementary material (http://http://www.civm.duhs.duke.edu/2013_macaque_tractography/).

7.3.4. Simple fiber pathways

1) Anterior commissure (AC, Figure 23)

The AC is a compact bundle of fibers that, along with the corpus callosum, is a major pathway for interhemispheric connections. The AC crosses the midline immediately rostral to the fornix and superior to the basal forebrain. The large posterior limbs of the AC connect the bilateral superior and inferior temporal lobes. The considerably smaller anterior limbs form a U-shaped bundle that extends rostrally connecting various olfactory structures. The anterior and posterior limbs of the AC can be clearly seen in the magnified inset of the anatomic image presented in the bottom left panel of Figure 23. Tractography in this relatively simple fiber pathway was fairly consistent across all acquisition protocols. The major difference between protocols was the thickness of the posterior limbs and presence or absence of the anterior limbs. Higher spatial resolution datasets (DTI-12, QBI-30, QBI-60) had thicker posterior limbs and more well defined anterior limbs. In contrast, lower resolution datasets with higher q-space sampling had thinner posterior limbs and small or absent anterior

limbs. Overall higher spatial resolution datasets were more representative of known anatomy.

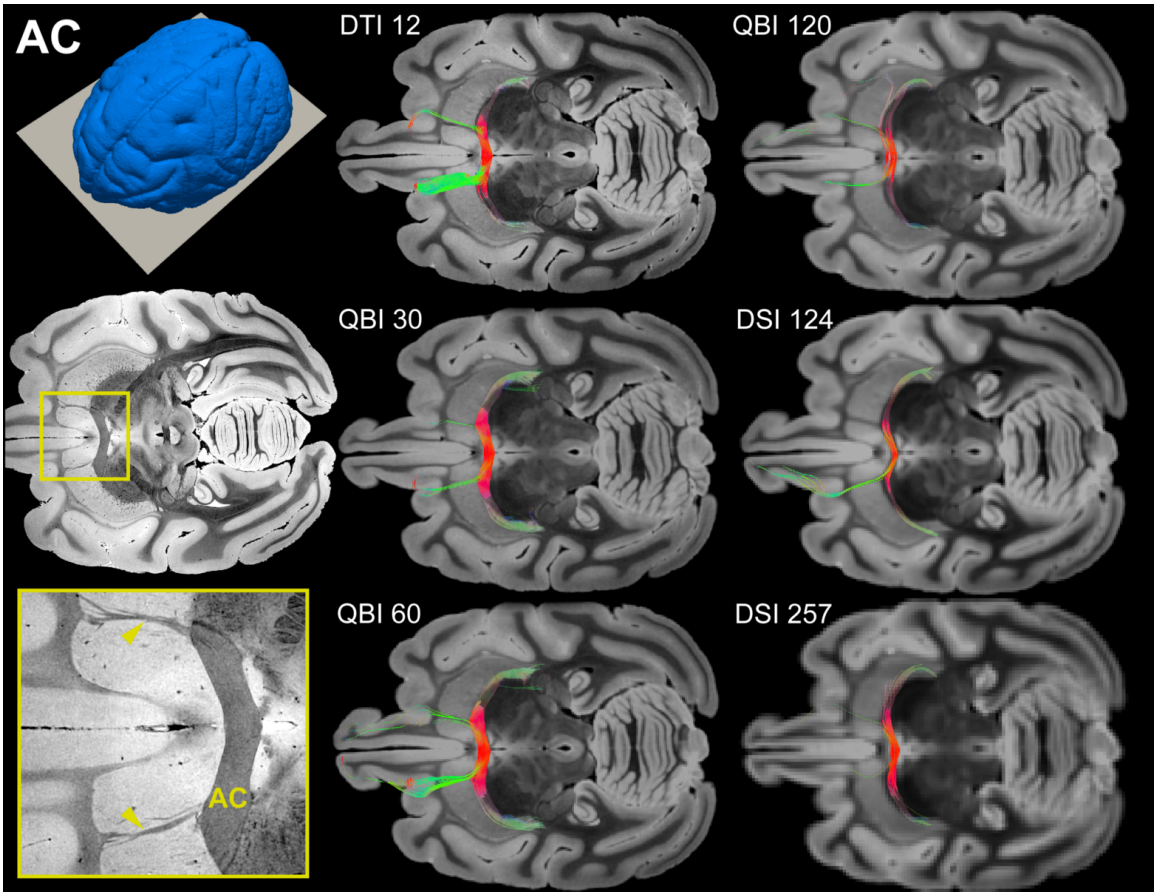

Figure 23 - Anterior commissure (AC) tractography results. Directionally colored tractography results from each of the six time-match diffusion imaging protocols are shown on top of a single axial slice from the corresponding b0 image. Slice location is shown in the top left of the figure on a blue surface rendering of the brain. The corresponding axial slice from the high-resolution anatomic image volume is displayed on the left side of the figure, along with a magnified inset showing the anatomy of the AC. The small anterior limbs of the AC are indicated with arrowheads.

2) Cingulum bundle (CB, Figure 24)

The CB courses rostro-caudally immediately dorsal to the corpus callosum and connects the orbital frontal, prefrontal, cingulate, parietal, and temporal cortices. All six tractography datasets were able to reconstruct nearly the full rostro-caudal extent of the CB, but the branching pattern differed substantially

between datasets. The rostral-most branches to the prefrontal and orbital frontal cortices were more correctly represented by QBI-120 and DSI-124 and were largely absent from other datasets. Although DTI-12 appears to have a prefrontal branch, these tracks curve dorsally and medially and may be largely erroneous. Many of the tractography datasets picked up dorsally oriented cingulate cortex U-fibers along the major limb of the CB to varying degrees. DTI-12 picked up the most U-fibers while DSI-256 had none. All six datasets tracked the small dorsal branch connecting the caudal parietal cortex (area Opt); however DTI-12 and QBI-30 had several erratic stray fibers emerging from this branch. The major caudal branch connecting retrosplenial areas 29 and 30 was present in all datasets, but the larger branch, which extends ventrally into the temporal lobe, was absent from all six datasets.

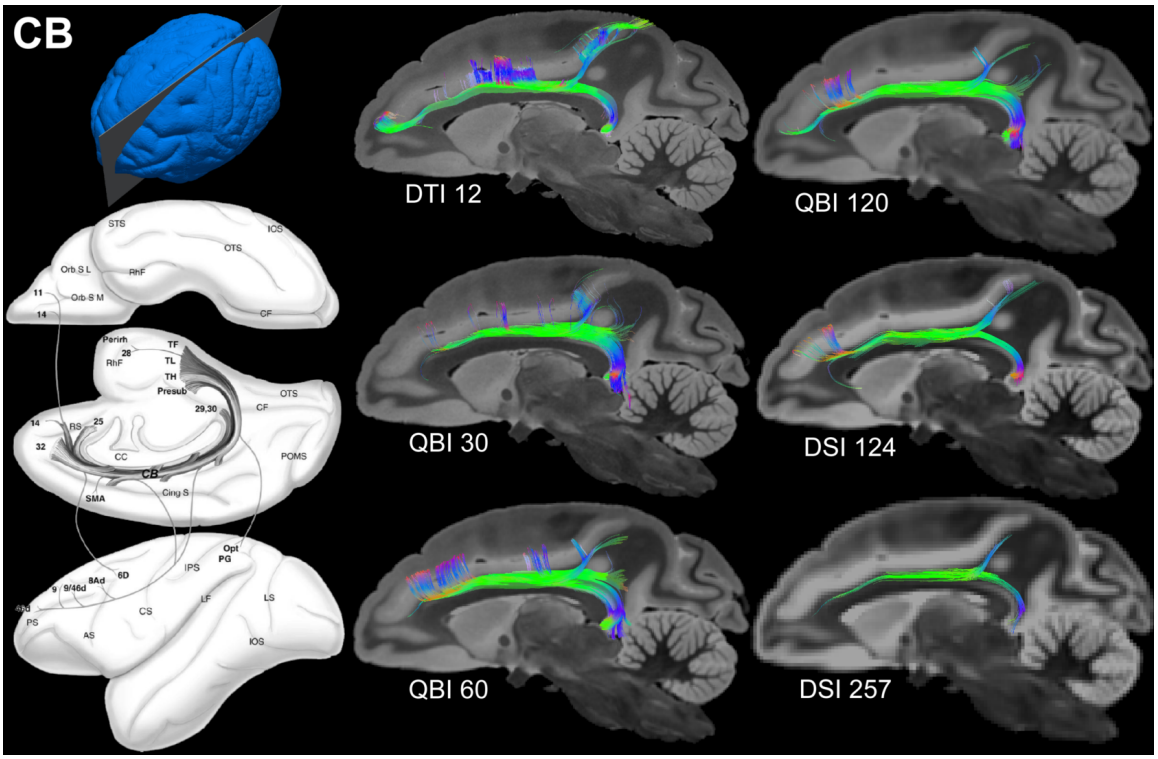

Figure 24 - Cingulum bundle (CB) tractography results. Directionally colored tractography results from each of the six time-match diffusion imaging protocols are shown on top of a single sagittal slice from the corresponding b0 image. Slice location is shown in the top left of the figure on a blue surface rendering of the brain. The relevant diagram from the Schmahmann and Pandya autoradiography-based fiber pathway atlas is included on the left side of the figure.

3) Corticospinal tracts (CT, Figure 25)

The CT are formed by axons from upper motor neurons in the primary motor cortex. These fibers course caudally and ventrally from the motor cortex, through the internal capsulae, the cerebral peduncles, and the pyramids before decussating and terminating in the spinal cord. The internal capsule portion of the CT is shown in high-resolution anatomic image in the bottom left panel of Figure 25. The subcortical portion of the CT was well represented by all six tractography datasets, but cortical tracks varied considerably. Although CT fibers originate from the length of the primary motor cortex, only the superior-most fibers were reconstructed in tractography datasets. Interestingly, bilateral cortical

tracks were only correctly represented in the high spatial resolution DTI-12 and QBI-30 datasets. Lower resolution datasets with higher q-space sampling had unilateral or completely absent cortical tracks.

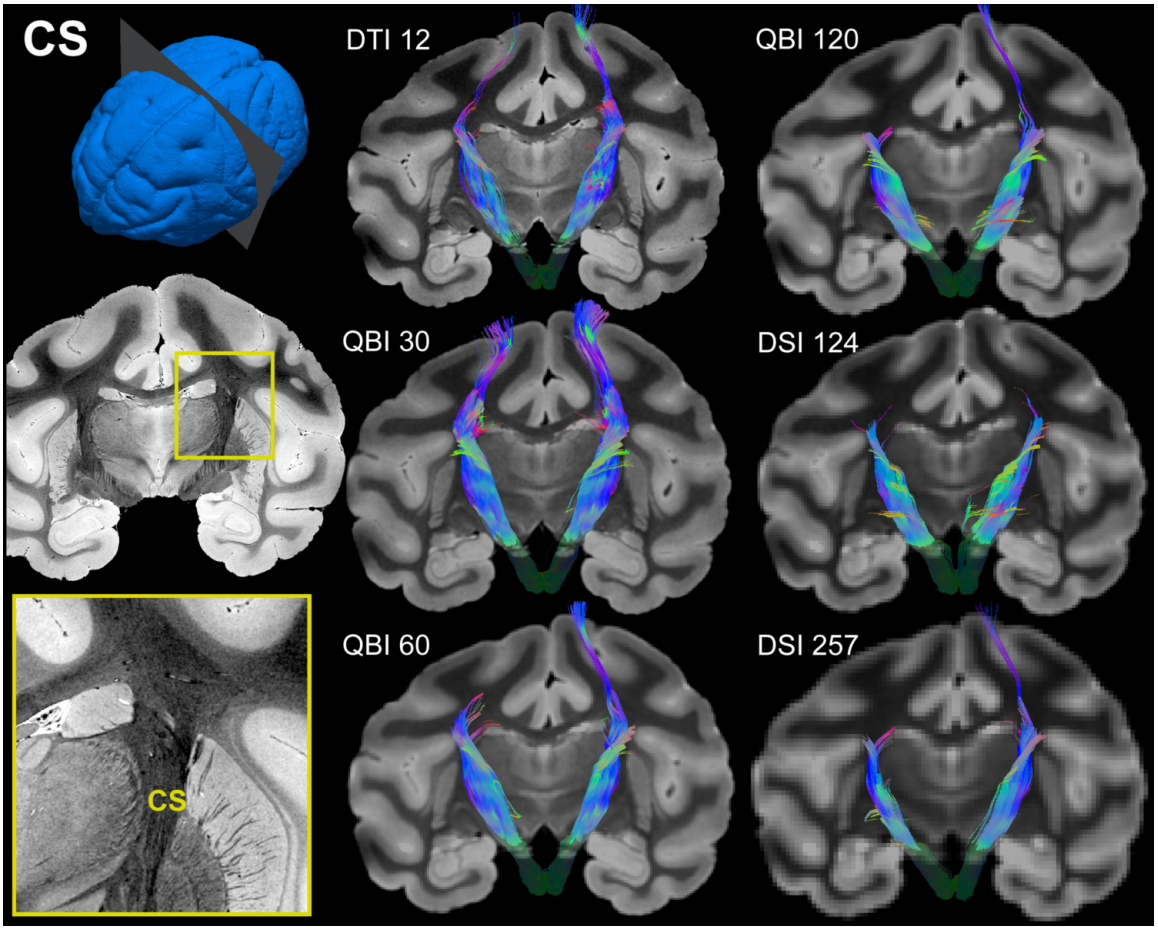

Figure 25 - Corticospinal tract (CT) tractography results. Directionally colored tractography results from each of the six time-match diffusion imaging protocols are shown on top of a single coronal slice from the corresponding b0 image. Slice location is shown in the top left of the figure on a blue surface rendering of the brain. The corresponding coronal slice from the high-resolution anatomic image volume is displayed on the left side of the figure, along with a magnified inset showing the anatomy of the CT.

4) Optic tracts (OT, Figure 26)

The OT forms the middle portion of the visual system and courses between the optic chiasm and the lateral geniculate nucleus (LGN). The LGN sits just rostral to the hippocampal formation at the lateral side of the thalamus as

shown in the high-resolution anatomic image (Figure 26, bottom left). Tractography of the OT was very consistent across all six acquisition protocols. All six datasets correctly connected the LGN and represented midline crossings in the optic chiasm. The DTI-12 dataset had slightly more stray tracks than other datasets but still closely represented known anatomy. Overall differences between protocols were minimal for the OT and no dataset was significantly better than the others.

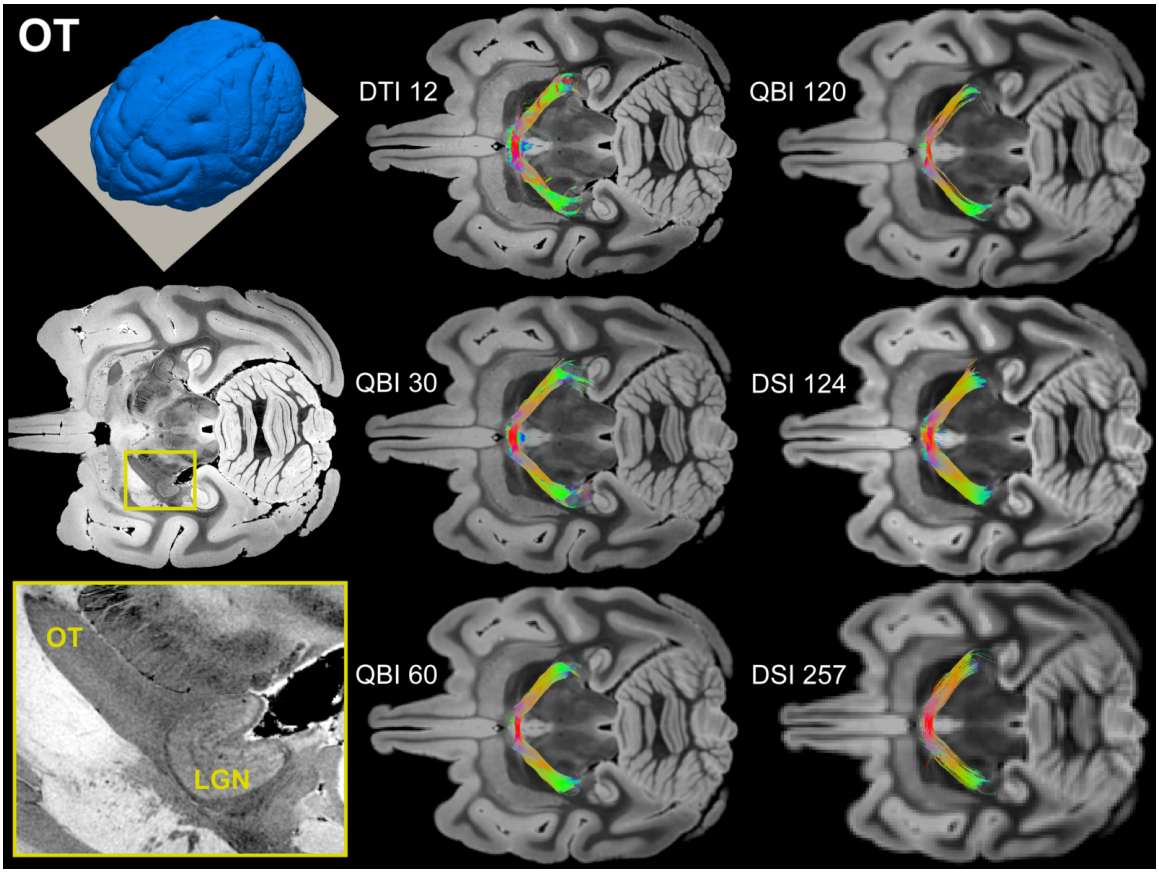

Figure 26 - Optic tract (OT) tractography results. Directionally colored tractography results from each of the six time-match diffusion imaging protocols are shown on top of a single axial slice from the corresponding b0 image. Slice location is shown in the top left of the figure on a blue surface rendering of the brain. The corresponding axial slice from the high-resolution anatomic image volume is displayed on the left side of the figure, along with a magnified inset showing the OT terminating in the lateral geniculate nucleus (LGN).

7.3.5. Complex fiber pathways

1) Middle longitudinal fasciculus (MdLF, Figure 27)

The MdLF forms the major white matter component of the superior temporal gyrus and courses between the caudal inferior parietal lobule and the superior temporal sulcus. All six protocols were able to approximate nearly the full extent of the pathway; however, DTI-12 and DSI-257 were slightly shorter than the other four datasets. This difference is reflected in the mean length measurements in Table 8, which shows that DTI-12 and DSI-257 are several millimeters shorter than other datasets. The degree of stray tracks appeared to decrease with increasing q-space sampling, with DTI-12 having the most stray fibers, and DSI-257 having almost none. The branching pattern at the ventral terminus of the MdLF was well represented by the three QBI protocols and DSI-124, but was less apparent in DTI-12 and DSI-257. No single dataset clearly stood out as the most similar to known anatomy, but QBI-60, QBI-120 and DSI-124 each had very similar length, course, and branching patterns with relatively few stray fibers.

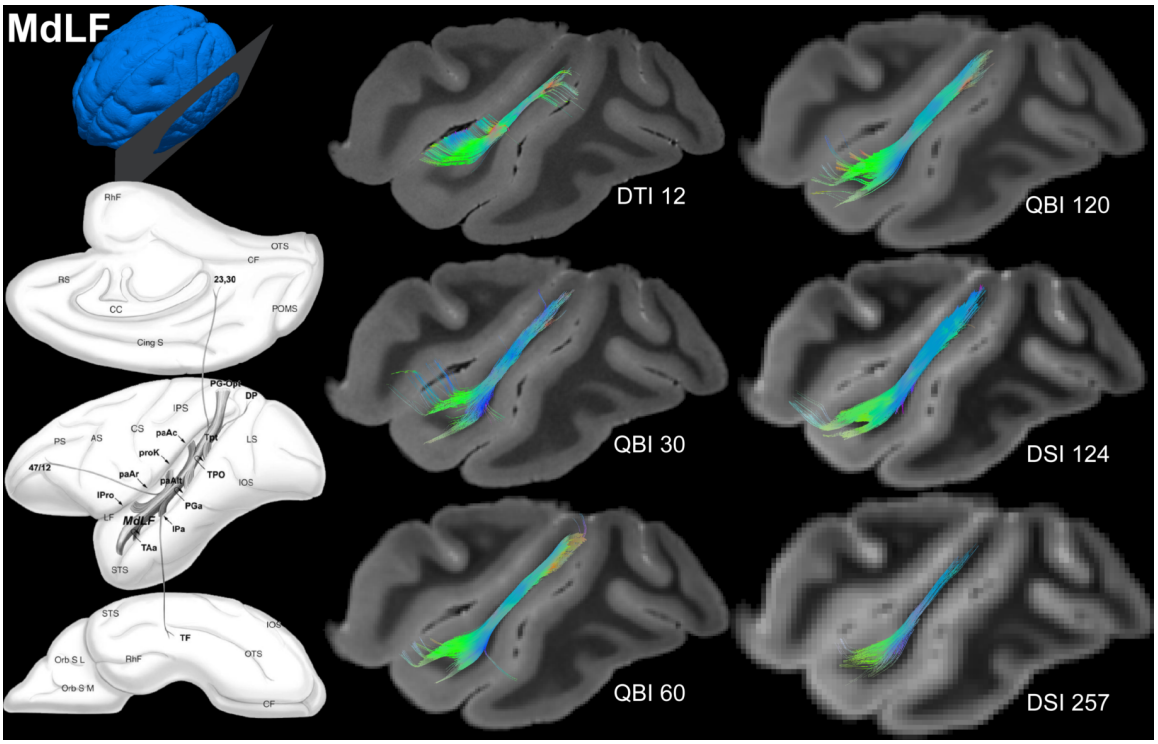

Figure 27 - Middle longitudinal fasciculus (MdLF) tractography results. Directionally colored tractography results from each of the six time-match diffusion imaging protocols are shown on top of a single sagittal slice from the corresponding b0 image. Slice location is shown in the top left of the figure on a blue surface rendering of the brain. The relevant diagram from the Schmahmann and Pandya autoradiography-based fiber pathway atlas is included on the left side of the figure.

2) Inferior longitudinal fasciculus (ILF, Figure 28)

The ILF is a particularly long association pathway that connects the temporal lobe with the occipital lobe, caudal parietal cortex, and caudal cingulate gyrus. Despite its length, tractography was relatively successful at reconstructing the ILF. The ventral limb, which courses through the temporal lobe white matter, was accurately reconstructed by all diffusion protocols except DTI-12, where the ventral tracks followed a tortuous path, eventually straying rostrally into the superior temporal gyrus. The dorsal branches connecting the parieto-occipital area (POa), caudal parietal cortex (area Opt) and dorsal prelunate area (DP) were missing in the DSI protocols, but were present to varying degrees in the

three QBI protocols. Interestingly, all six protocols correctly reconstructed the small branch of the ILF that extends into the ventral preoccipital areas (i.e., V4V and V3V). Overall the three QBI datasets appeared closest to the known anatomy with the major difference between datasets being the dorsal branching pattern.

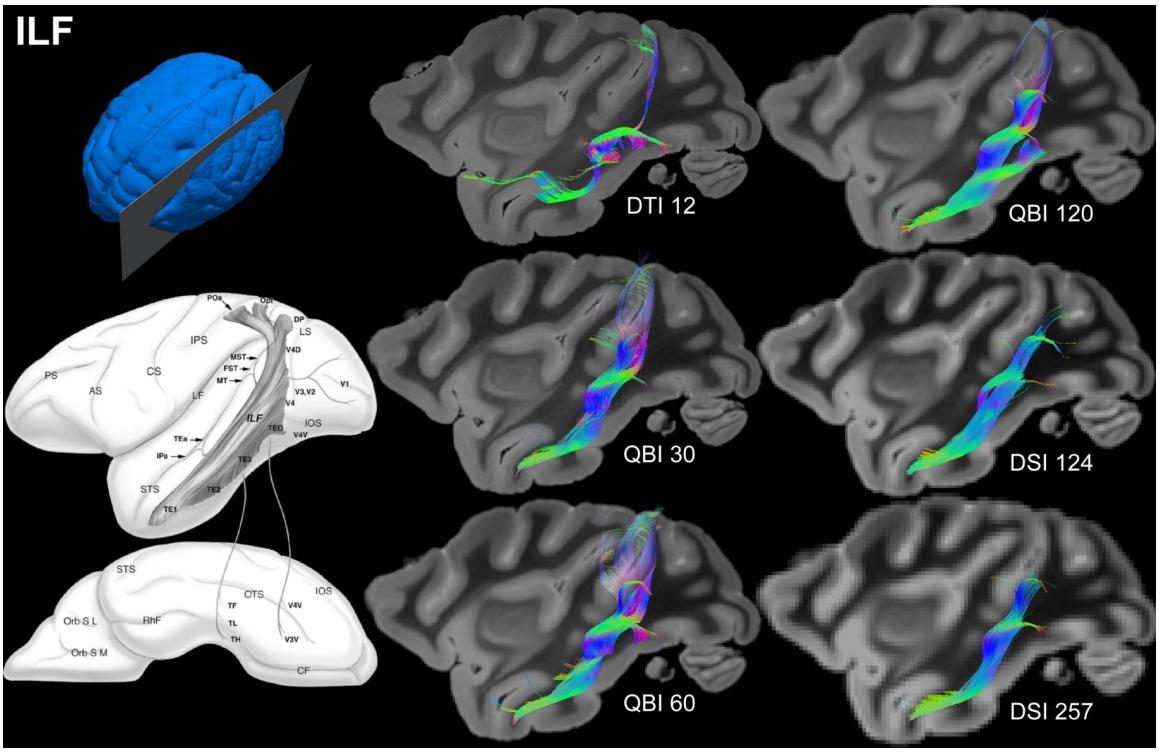

Figure 28 - Inferior longitudinal fasciculus (ILF) tractography results. Directionally colored tractography results from each of the six time-match diffusion imaging protocols are shown on top of a single sagittal slice from the corresponding b0 image. Slice location is shown in the top left of the figure on a blue surface rendering of the brain. The relevant diagram from the Schmahmann and Pandya autoradiography-based fiber pathway atlas is included on the left side of the figure.

3) Uncinate fasciculus (UF, Figure 29)

The UF connects the rostral and ventral temporal regions with the medial and orbital frontal cortices. Tractography results for the UF were quite similar across the six protocols used for this study. The DTI-12 protocol yielded the most stray fibers, but was otherwise similar to other datasets. The major difference

between datasets was the representation of the rostral limb extending into the medial and orbital frontal cortices. Although no tractography dataset extended as far rostrally as autoradiography data indicate, the two DSI protocols extended the farthest medially and rostrally into the frontal lobe.

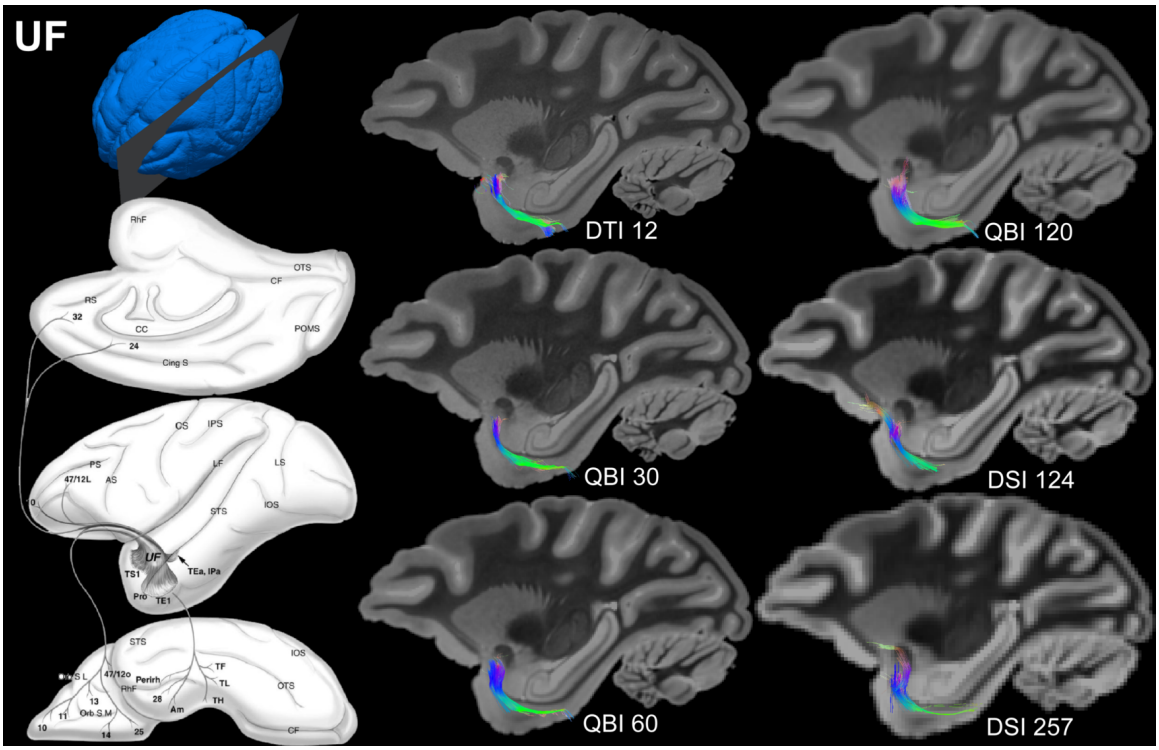

Figure 29 - Uncinate fasciculus (UF) tractography results. Directionally colored tractography results from each of the six time-match diffusion imaging protocols are shown on top of a single sagittal slice from the corresponding b0 image. Slice location is shown in the top left of the figure on a blue surface rendering of the brain. The relevant diagram from the Schmahmann and Pandya autoradiography-based fiber pathway atlas is included on the left side of the figure.

4) Extreme capsule (EmC, Figure 30)

The EmC connects the superior temporal region caudally with the prefrontal and orbital frontal cortices rostrally. Autoradiography data suggest that the rostral portion of this fiber pathway forks into a superior ramus, which courses into the prefrontal cortex, and an inferior ramus that connects to the orbital frontal cortex. The EmC courses very close to sheet-like group of cortical U-fibers in the

frontal cortex, and the resulting aberrant tracking of these U-fibers was a major source of error in these tractography results. The DTI-12 dataset was the worst affected, with virtually all tracks curving laterally into the cortical U-fiber pathway. The three QBI protocols also had significant U-fiber involvement, although in each case at least some tracks continued correctly into the prefrontal cortex. Neither of the two DSI datasets had any significant cortical U-fiber involvement. The rostral branching pattern differed significantly between datasets. The inferior ramus connecting the orbital frontal cortex was not present in any dataset. The larger superior ramus connecting the dorsal prefrontal cortex was present in QBI-60, DSI-124 and DSI-257, but was absent or truncated in the other three datasets.

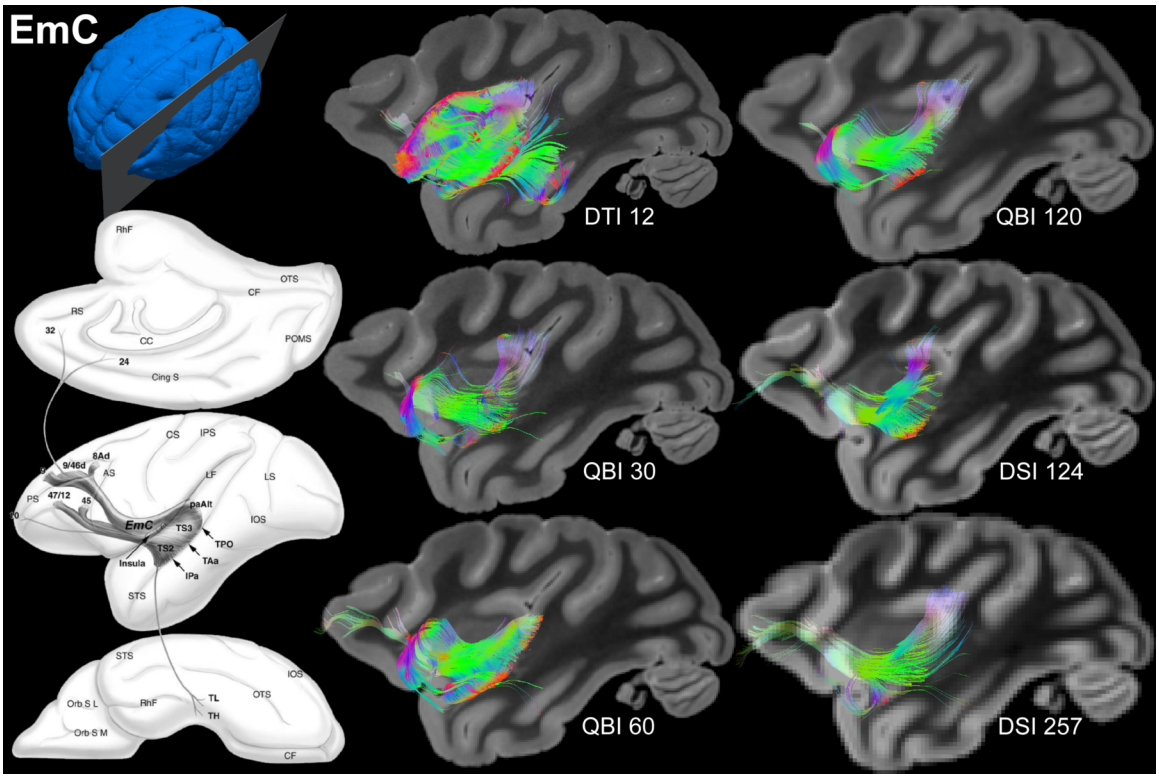

Figure 30 - Extreme capsule (EmC) tractography results. Directionally colored tractography results from each of the six time-match diffusion imaging protocols are shown on top of a single sagittal slice from the corresponding b0 image. Slice location is shown in the top left of the figure on a blue surface rendering of the brain. The relevant diagram from the Schmahmann and Pandya autoradiography-based fiber pathway atlas is included on the left side of the figure.

7.3.6. Quantitative comparisons between tractography datasets

Tractography length and volume statistics are presented in Table 8. In most cases, mean track length was similar for all six acquisition schemes; however, track volume varied by an order of magnitude in some cases. In general, the length and volume statistics from the DTI-12 scheme were most different from other schemes. This observation is supported by the results of the mean track correlation analysis (Figure 31). DTI-12 tractography was, on average, the most different from mean tractography across the eight pathways included in our analysis. There was a general trend toward increasing similarity

with other datasets as q-space sampling increased and spatial resolution decreased. QBI-120, DSI-124 and DSI-257 were, on average, the most consistent with other datasets. Importantly, tractography similarity measurements did not directly correlate with the choice of reconstruction protocol.

Table 8 - Length and volume statistics for tractography data.

		Max length (mm)	Mean length (mm)	Volume (ml)
AC	**DTI-12**	46.37	27.84	0.05
	QBI-30	57.31	41.11	0.15
	QBI-60	58.23	36.30	0.21
	QBI-120	44.12	27.28	0.11
	DSI-124	56.51	38.19	0.09
	DSI-257	41.91	31.22	0.18
CB	**DTI-12**	66.09	26.48	0.17
	QBI-30	43.14	26.20	0.14
	QBI-60	48.35	24.49	0.26
	QBI-120	53.47	29.08	0.28
	DSI-124	50.49	23.43	0.16
	DSI-257	26.40	16.64	0.15
CT	**DTI-12**	67.40	46.08	0.32
	QBI-30	69.06	47.91	0.79
	QBI-60	66.72	45.55	0.78
	QBI-120	65.21	42.13	0.97
	DSI-124	54.05	39.64	0.92
	DSI-257	57.31	41.76	1.11
OT	**DTI-12**	41.04	17.21	0.11
	QBI-30	53.72	24.89	0.21
	QBI-60	43.79	23.14	0.18
	QBI-120	38.59	16.27	0.15
	DSI-124	37.23	16.25	0.28
	DSI-257	40.04	17.13	0.32
MdLF	**DTI-12**	23.17	12.46	0.03
	QBI-30	29.09	17.88	0.06
	QBI-60	31.01	18.86	0.09
	QBI-120	28.28	17.49	0.12
	DSI-124	29.47	16.11	0.15
	DSI-257	18.46	11.25	0.10
ILF	**DTI-12**	53.53	12.30	0.07
	QBI-30	56.82	24.77	0.17
	QBI-60	61.53	27.43	0.30
	QBI-120	47.23	22.34	0.29
	DSI-124	31.87	17.33	0.20
	DSI-257	34.83	21.47	0.26
UF	**DTI-12**	22.03	15.26	0.03
	QBI-30	22.05	15.05	0.02
	QBI-60	18.66	10.59	0.05
	QBI-120	23.63	15.50	0.09
	DSI-124	17.37	11.05	0.06
	DSI-257	38.88	13.12	0.14
EmC	**DTI-12**	66.11	22.62	0.43
	QBI-30	45.04	17.47	0.15
	QBI-60	44.01	19.15	0.32
	QBI-120	45.63	19.95	0.33
	DSI-124	44.04	18.16	0.31
	DSI-257	46.90	22.39	0.63

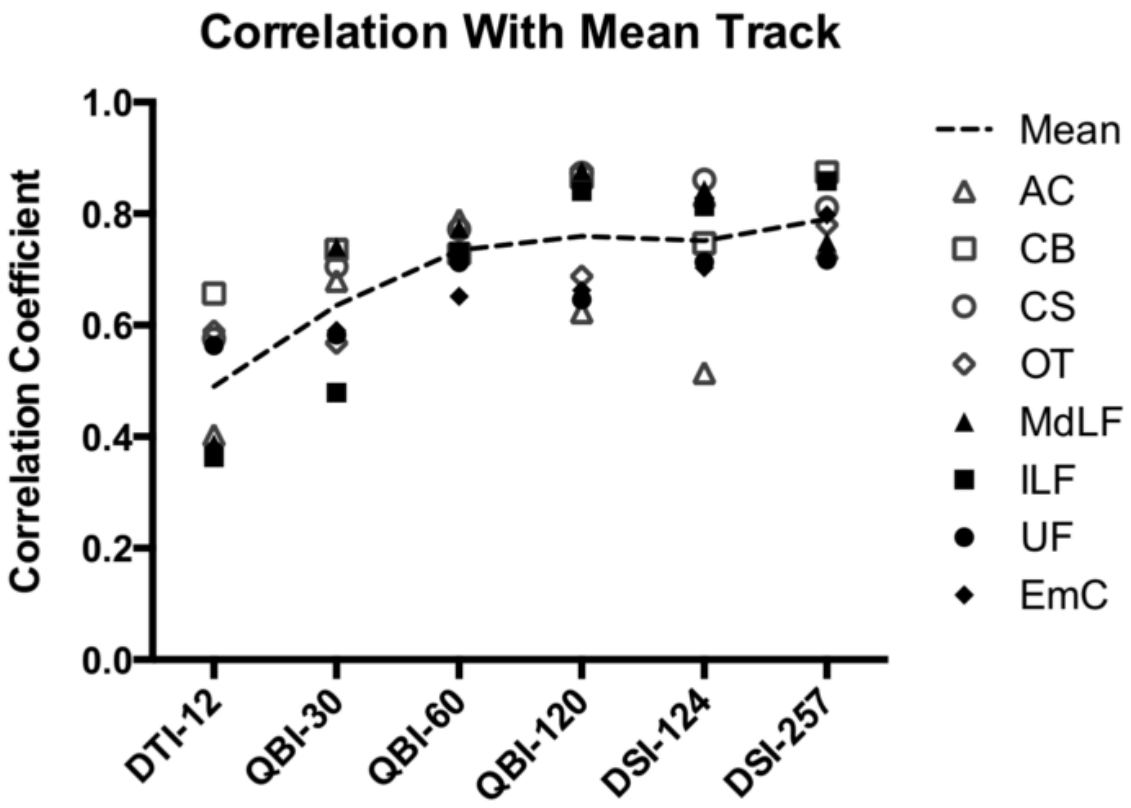

Figure 31 - Track density imaging (TDI) correlation results. A mean track was generated for each of the eight tracks analyzed in this study by averaging TDIs from all six protocols. Individual TDIs were then compared to the mean track using normalized cross correlation. Correlation results for the four "simple" pathways are shown with open points, while results for the four "complex" pathways are shown with closed points. The average correlation coefficient across all eight pathways is indicated with a dotted line.

7.4. Discussion

7.4.1. The effect of acquisition and reconstruction strategies

One of the most interesting, and perhaps concerning, findings to emerge from this study is that tractography results can vary substantially, even with the same subject and total acquisition time. This result is not necessarily surprising when considering the different acquisition and reconstruction strategies that were used. Indeed, each of the three algorithms has strengths and weaknesses, which dictate tractography behavior in areas of fiber complexity. DTI fits the available

data to a single fiber orientation per voxel, which can be as much as 45° off from any true fiber orientation. The result is that virtually any intravoxel fiber complexity leads to stray fibers or premature termination (Jones, 2003), as is evident in the crossing fiber phantom simulation data presented in Figure 21. In contrast, the QBI method used for this study fits data to a high-order spherical harmonic, which can reconstruct many different fiber orientations per voxel, but is nonetheless constrained by the imposed model (Descoteaux et al., 2007). DSI altogether avoids the constraints of a model by attempting to reconstruct the diffusion function of each voxel directly; however, the ability to do so is entirely dependent on the accuracy and density of diffusion sampling (Wedeen et al., 2005). Therefore, our study highlights the problems that can arise when comparing tractography results from different acquisition and reconstruction strategies. Interestingly, tractography results were substantially different even between datasets of the same type (i.e., between the three QBI protocols), suggesting that the reconstruction algorithm was not the only factor dictating these differences.

7.4.2. Recommendations for anatomically accurate tractography

Ensuring anatomic accuracy is essential for the future of diffusion tractography studies. Accurate 3D maps of white matter connectivity could allow researchers to assess architectural differences in a quantitative way, and foster the development of automated approaches for identifying signatures of normal versus diseased white matter connections. Although the results of this study are

insufficient to provide a definitive approach to ensuring anatomically accurate tractography, they do shed light on a number of important considerations. We have attempted to distill our observations into a short list of recommendations for getting the most meaningful tractography out of a given acquisition time.

1) Anatomy matters.

It is well known that certain white matter pathways are easy to reconstruct with tractography, and others are not. Structures that are relatively easy to track, such as the curved fiber phantom and the four “simple” pathways chosen for this study, can be accurately reconstructed using simple models like DTI. In contrast, more complex structures, including the crossing fiber phantom and the four “complex” pathways analyzed in this study, require estimation of fiber crossings. The optimal diffusion acquisition strategy thus depends to some degree on the specific anatomy being imaged. Some simple fiber pathways like the AC and CT were actually more accurately represented by high resolution/low q-space sampling datasets. In these cases, it seems that the reduction in partial volume effects provided by high resolution outweighs the effects of reduced q-space sampling. This effect can be understood intuitively in structures like the anterior limbs of the AC, which are straight and coherent, but small and thus vulnerable to partial volume effects. If the tractography target is relatively simple, high resolution may be preferable to high q-space sampling. Additionally, track volume measurements from high spatial-resolution datasets are more likely to reflect actual volumes (Lebel et al., 2012).

2) Fiber complexity is still present at high spatial resolution.

The spatial resolution of the DTI-12 dataset presented here (130 microns isotropic) is at a much higher resolution than standard clinical diffusion imaging (>10^3 fold), and, to our knowledge, is the highest resolution diffusion imaging ever reported for the primate brain. Despite this unusually high resolution, tractography from the DTI-12 dataset was very inaccurate in complex fiber pathways. It seems that the 12-direction q-space sampling scheme, coupled with the diffusion tensor model that such sparse sampling necessitates, was simply incapable of accurately representing the intravoxel fiber geometry. This outcome suggests that the scale of fiber complexity is far smaller than the scale of currently feasible imaging voxels. Unless diffusion imaging resolution improves dramatically, it seems prudent to assume fiber complexity will always be present in some areas of the primate brain. In other words, it is not effective to use high spatial resolution as a means of globally eliminating intravoxel fiber complexity.

3) High q-space resolution can be insufficient for large voxels.

It seems obvious that increased q-space sampling should lead to improved tractography, but this conclusion is not always true when q-space sampling comes at the cost of decreased spatial resolution. For example, the DSI-257 dataset analyzed in this study was the most extensively sampled in q-space, but was not the most anatomically accurate. In particular, the DSI-257 dataset was prone to premature track termination (e.g., in the ILF and CB). Part

of the issue is that large voxels are more likely to contain multiple different white matter pathways, as well as parts of adjacent gray matter areas and/or fluid spaces. This effect is particularly pronounced when voxel size is large relative to the size of the white matter pathway being reconstructed. For example, the CB was only about four voxels wide in the DSI-257 dataset analyzed here. In this case, even extensive q-space sampling was incapable of accurately resolving underlying fiber geometry. This suggests that, when voxels are large relative to the structure of interest, high q-space sampling may not be sufficient to resolve intravoxel fiber architecture.

4) Balance is best.

In this study, the most anatomically accurate tractography results were achieved with a balance between spatial resolution and q-space sampling. The datasets that came the closest to representing known anatomy (QBI-60, QBI-120, and DSI-124) had small enough voxels to avoid major partial volume effects, and sufficient q-space sampling to resolve at least some degree of intravoxel fiber crossing. Based on these data we suggest > 30 gradient directions for accurate tractography of complex anatomy like the cortical association pathways studied here. This determination concurs with previous investigations on the effects of the number of gradient directions (Jones, 2004; Zhan et al., 2008; 2010), and is supported by our crossing fiber simulation data where errors in the crossing region were largely absent with > 30 gradient directions. The choice of q-space sampling pattern (i.e., single b-value QBI vs.

multi b-value DSI) did not seem to matter as much as the total number of q-space samples; however, it is worth noting that DSI schemes avoid assumptions imposed by diffusion models at the cost of being generally more demanding on imaging hardware.

7.4.3. Relevance to human brain mapping

We chose to image the macaque brain because its encephalization and overall structure provide a good model for the human brain. Previous tractography studies have shown that a many white matter pathways are similar in humans and macaques (Parker et al., 2002; Croxson, 2005), suggesting that the results presented here are directly relevant to human brain mapping. Although the spatial resolutions used for this study are much higher than a typical human dataset, it is important to consider differences in brain volume. The macaque brain is about 17-fold smaller than the human brain by volume (Herculano-Houzel, 2009), so voxels must be 17-fold smaller to achieve comparable structural resolution. Accounting for volumetric differences, the spatial resolutions reported here (0.13 mm – 0.6 mm) are comparable to spatial resolutions of 0.33 mm – 1.5 mm in humans, which has considerable overlap with recent advances in human diffusion imaging resolution (Golay et al., 2002; Jeong et al., 2003; Kamali et al., 2009). With human brain mapping initiatives moving towards higher field, multi-channel receive coils, and stronger imaging gradients (McNab et al., 2013), it seems likely that clinical diffusion imaging resolution will continue to improve in the near future. With increasing resolution

capabilities and ever expanding q-space sampling protocols, consideration of the tradeoffs explored in this manuscript will inevitably play a role in the future of human brain mapping with diffusion tractography.

7.5. Conclusions and future directions

In this study we have shown that diffusion tractography results can vary widely with the choice of q-space sampling and spatial resolution, even when the tissue being imaged and the total acquisition time are held constant. We have also demonstrated that balancing acquisition time between q-space sampling and spatial resolution provides more anatomically accurate results than, for example, focusing solely on spatial resolution. One of the major limitations of our analyses, and of tractography in general, is the fact that it is largely qualitative. Although tractography can be used as a framework for statistical comparisons (Smith et al., 2006), and as a quantitative metric of brain connectivity (Honey et al., 2009), there is currently no quantitative method for assessing anatomic accuracy. Further, even if such a method existed, what would tractography be compared against? The type of data provided by the previously described anatomic methods (i.e., dissection, myelin-stained histology, tracer studies) is complementary with, rather than comparable to, diffusion tractography. Like its predecessors, diffusion tractography will certainly add to rather than replace previous methods. Perhaps the most important contribution of diffusion tractography will be to help integrate previous knowledge into a meaningful 3D map, and allow quantitative assessment of tract morphology and structural

connectivity. We hope that our systematic analysis of different diffusion imaging protocols provides some insight into the best use of acquisition time for future brain mapping studies.

8. Conclusions and Future Work in DT-MRH Brain Atlasing

8.1. DT-MRH brain atlasing of animal models

This dissertation has described the process of building a novel DT-MRH brain atlas of a small animal model, including initial technical considerations, data acquisition and processing, segmentation and labeling, and finally, analysis and database construction. This work highlights many of the unique features of DT-MRH brain atlasing, including the ability to build population averages and track regional changes in brain volume and quantitative contrast across time. The end result is a detailed, quantitative atlas and database of rat brain postnatal neurodevelopment that is unique both in its scope and in its content. This work adds to a growing body of MRH atlases of small animal models, many of which have proven valuable in advancing brain research (Johnson et al., 2010; Chuang et al., 2011; Johnson et al., 2012). As small animal imaging technology continues to improve, it seems likely that the list of species and strains for which an MRH atlas exists will continue to increase. There are still many innovative ways in which this technology could be leveraged to create novel, and informative brain atlases. For example, instead of building a database of normal neurodevelopment, one could build an atlas of the normal brain senescence that occurs with advanced age. It is also possible to capture brain structural dynamics resulting from external sources such as learning or diet. In short, MRH and in

particular DT-MRH have facilitated an entirely new generation of quantitative brain atlasing with ample potential for expansion and innovation.

8.2. Towards a DT-MRH atlas of the human brain

While the value of animal models should not be underestimated, the ultimate goal of most neuroscience research is to better understand the human brain. A DT-MRH atlas of the human brain would be a major contribution to the brain mapping community, and a valuable tool for understanding human neurological disease. Unfortunately, DT-MRH of human specimens is much more difficult than the animal specimen work presented here. First, intact, normal human brain specimens are difficult to obtain, and perfusion fixation is usually not an option. Second, the human brain is much larger, requiring both larger bore MRI machines and larger radiofrequency coils. Third, the array sizes and data volumes of human DT-MRH data would be large (several terabytes) and difficult to process using existing software pipelines. Finally, as discussed in the previous chapter, it is not clear to what extent differences in tissue microstructural complexity will affect diffusion contrast and tractography results. Despite these many challenges, the potential benefits of a DT-MRH atlas of the human brain make it a worthwhile endeavor. Although the generation of such an atlas is beyond the scope of this work, substantial progress has been made in acquiring and processing DT-MRH data from large sections of the human brain, including the human brainstem and diencephalon.

8.3. Initial work in the human brainstem

The human brainstem is a remarkably complex and compact network of important nuclei and white matter pathways. The brainstem also appears to play an important role in human brain diseases; recent advances in deep brain stimulation (DBS) have demonstrated that chronic stimulation of small nuclei and white matter tracts in the brainstem and diencephalon can have profound therapeutic effects on a variety of neurologic disorders including Parkinson's disease, Tourette syndrome, major depression, and chronic pain (Perlmutter and Mink, 2006). Localization of increasingly precise DBS targets requires accurate 3D maps of brainstem architecture. Several atlases of the human brainstem already exist, including both conventional histology atlases (Paxinos and Huang, 1995) and MRI-based atlases (Soria et al., 2011; Edlow et al., 2012; Prats-Galino et al., 2012; Aggarwal et al., 2013; Ford et al., 2013; McNab et al., 2013). Previous MRI-based atlases have highlighted the importance of 3D images and diffusion contrast, but none has approached the spatial resolution and/or contrast resolution that is possible with DT-MRH. A DT-MRH atlas of the human brainstem would not only be a valuable contribution to the brain mapping and DBS fields, but would also be an important step towards generating a DT-MRH atlas of the whole human brain. For these reasons the brainstem is a logical starting point for proving the feasibility of a DT-MRH atlas of the human brain. Preliminary results in the human brainstem are shown in Figure 32 and Figure 33. While these results do not yet amount to a DT-MRH atlas of the human

brainstem, they nonetheless prove feasibility and demonstrate the level of anatomical detail that could be expected of such an atlas.

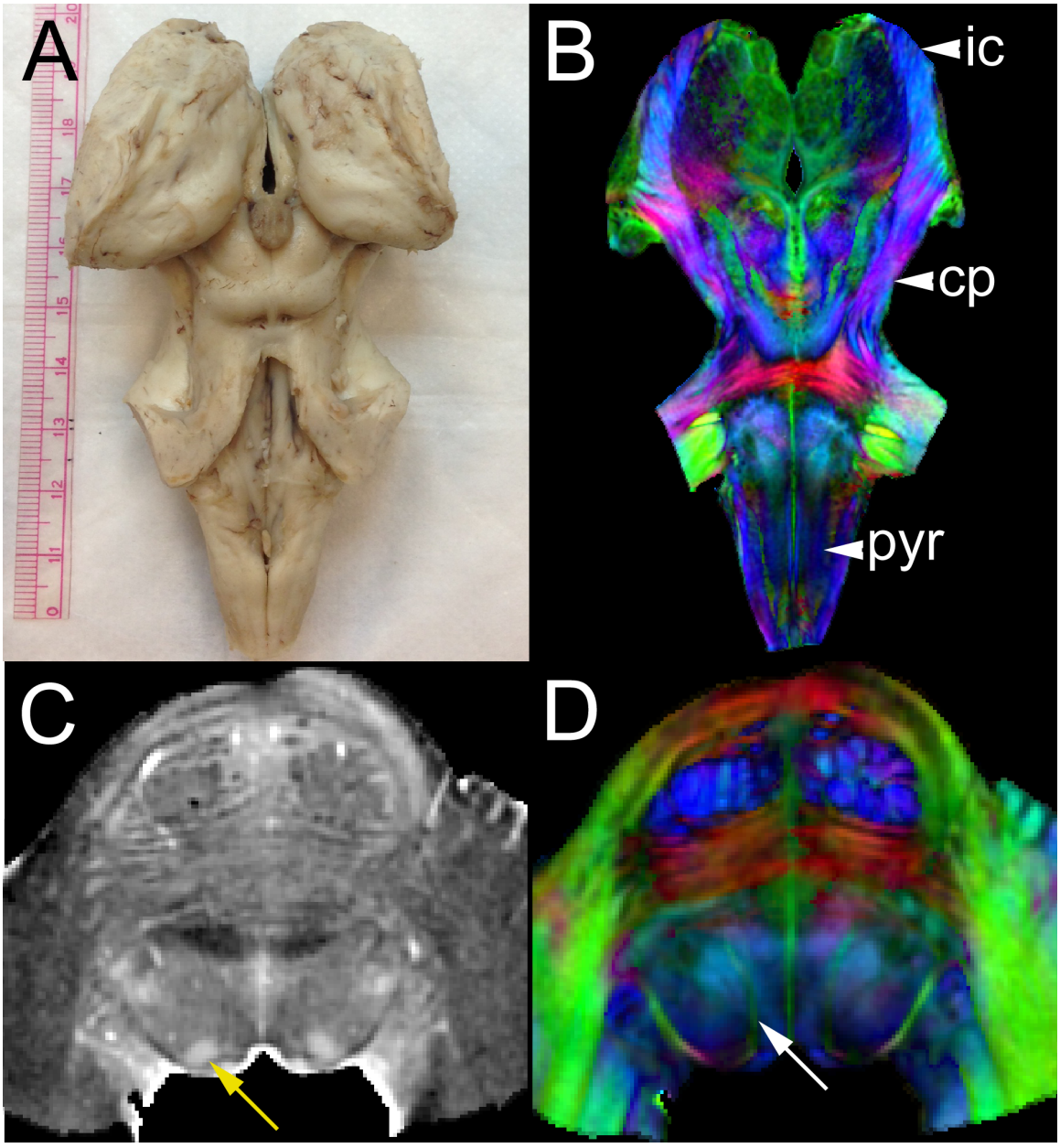

Figure 32 - Anatomic details of the human brainstem revealed by DT-MRH. A) A photograph of the human brainstem specimen. B) A coronal color fractional anisotropy map showing the pyramidal tract (pyr), cerebral peduncle (cp), and internal capsule (ic). C) Diffusion coefficient map highlighting the 6th nerve nucleus (arrow). D) The fractional anisotropy color map at the same level as C showing the 6th nerve itself (arrow).

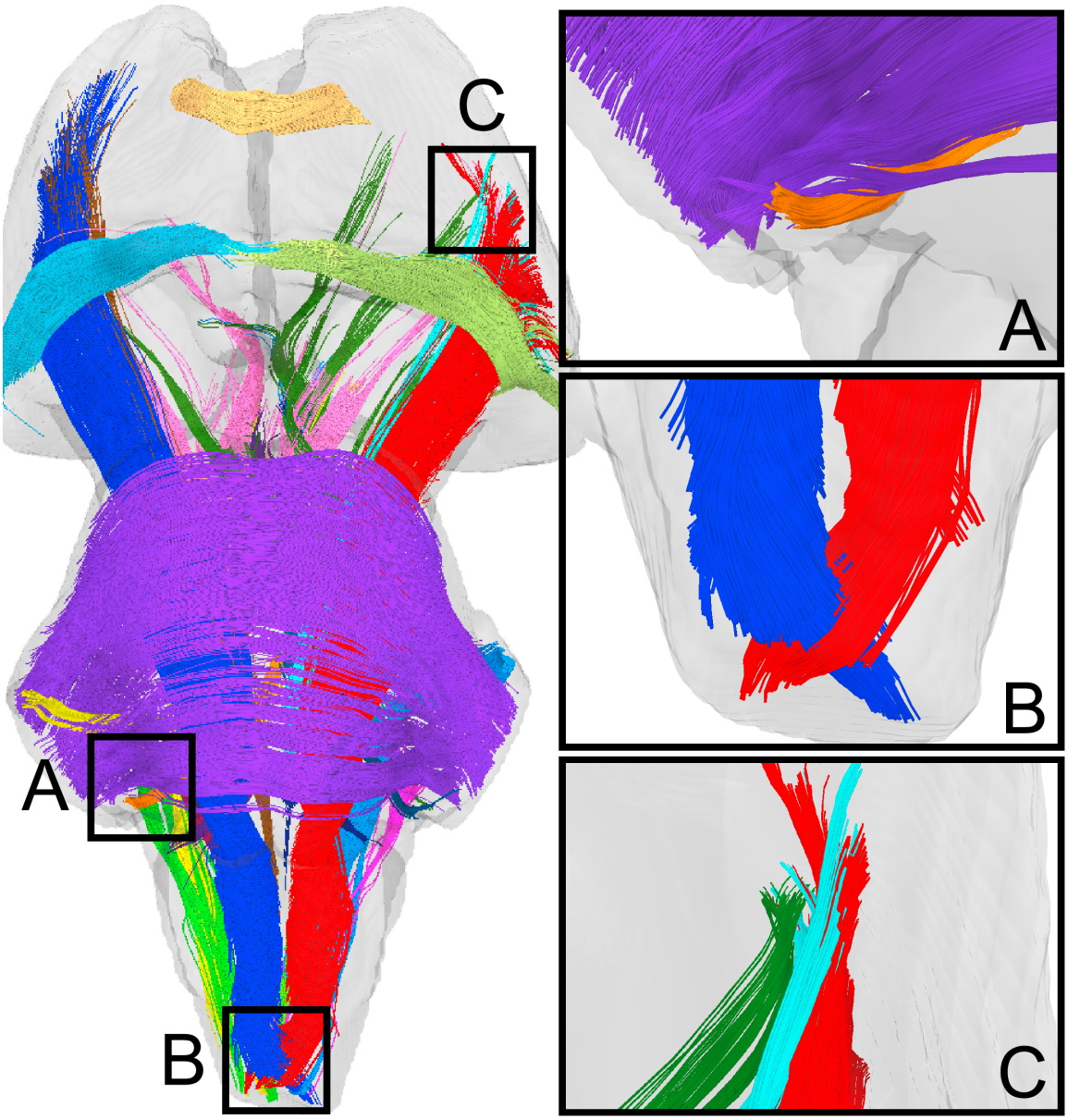

Figure 33 - Diffusion tractography showing 28 tracts in the human brainstem. A) The 7th cranial nerve (orange) emerging beneath the transverse fibers of the pons (purple). B) Interdigitating motor fibers in the pyramidal decussation. C) Multiple fiber populations in the internal capsule including corticobulbar fibers (green), fibers from the somatic sensory radiation (cyan), and corticospinal fibers (red).

These early results draw on the experience gained from the work presented in this dissertation, and prove that many of the valuable features of DT-MRH brain atlasing translate well to the human brain. Specifically, Figure 32

shows the importance of tensor-derived contrasts for highlighting, and eventually segmenting, different anatomical structures. Figure 33 demonstrates that, with careful consideration of the intravoxel complexity issues presented in Chapter 7, DT-MRH can produce anatomically accurate tractography in complex human brain regions. Together these results represent an exciting first step in creating a DT-MRH atlas of the whole human brain, but many challenges still remain. A complete human brain specimen is too large to fit in a majority of small animal imaging systems, and would therefore require the use of lower field clinical systems. Lower field strength, combined with the need to use larger, less sensitive radiofrequency coils presents a potential signal limitation for high spatial resolution diffusion imaging. In addition, the resulting dataset would be extraordinarily large and difficult to process using current tools. One potential solution is to acquire a single high-resolution anatomic scan of a complete human brain specimen in a clinical scanner, then section the specimen into smaller pieces, acquire DT-MRH datasets of those pieces in small animal scanners, and use the whole-brain image as a template for stitching the pieces together. This approach has the advantage of being realizable with current infrastructure; however, sectioning the brain specimen may create unwanted tissue distortions, and stitching together multiple DT-MRH datasets into a single larger image may prove technically difficult. While this approach is the logical extension of current work, the continuing evolution of MRH technology will ultimately drive future attempts to create DT-MRH atlases of the human brain.

8.4. Conclusions

The goal of this work was to explore the use of DT-MRH to study brain structure. In doing so, several important points about this technology have become apparent. First, DT-MRH is well suited for studying brain structure in rodent models. Mice and rats, in addition to being the most widely used model systems for studying brain diseases, are ideal for DT-MRH because of their size, and because of the large body of existing work in ex-vivo rodent MRI. Second, DT-MRH provides novel, quantitative data on brain macrostructure and microstructure. For example, this work has demonstrated the ability to measure accurate regional brain volumes, quantitative diffusion contrast, and population variability. Third, DT-MRH brain atlases can be used to track changes in quantitative parameters across dynamic processes, such as during the course of normal postnatal neurodevelopment. And finally, with careful consideration of the effect of intravoxel diffusion complexity, DT-MRH brain atlasing can be translated to more complex brains, including the human brain. While this work is by no means an exhaustive review of the advantages and limitations of DT-MRH brain atlasing, it does provide a reasonable overview of the technology and a specific example of its application to an important animal model. With ongoing efforts to create DT-MRH brain atlases for other important animal models, and for the human, it is clear that this technology will continue to grow in the future. As DT-MRH technology evolves, so too will the opportunities to create novel MR-based brain atlases that should find widespread use in the neuroscience community.

References

Aggarwal, M., Zhang, J., Pletnikova, O., Crain, B., Troncoso, J., Mori, S., 2013. Feasibility of creating a high-resolution 3D diffusion tensor imaging based atlas of the human brainstem: a case study at 11.7 T. Neuroimage 74, 117–127.

Allendoerfer, K.L., Shatz, C.J., 1994. The subplate, a transient neocortical structure: its role in the development of connections between thalamus and cortex. Annu Rev Neurosci 17, 185–218.

Arsigny, V., Fillard, P., Pennec, X., Ayache, N., 2006. Log-Euclidean metrics for fast and simple calculus on diffusion tensors. Magn Reson Med 56, 411–421.

Asato, M.R., Terwilliger, R., Woo, J., Luna, B., 2010. White matter development in adolescence: a DTI study. Cereb Cortex 20, 2122–2131.

Ashwell, K.W.S., Paxinos, G., 2008. Atlas of the developing rat nervous system. Elsevier Academic Press, San Diego.

Avants, B.B., Epstein, C.L., Grossman, M., Gee, J.C., 2008. Symmetric diffeomorphic image registration with cross-correlation: evaluating automated labeling of elderly and neurodegenerative brain. Med Image Anal 12, 26–41.

Avants, B.B., Tustison, N.J., Song, G., Cook, P.A., Klein, A., Gee, J.C., 2011. A reproducible evaluation of ANTs similarity metric performance in brain image registration. Neuroimage 54, 2033–2044.

Badea, A., Ali-Sharief, A.A., Johnson, G.A., 2007a. Morphometric analysis of the C57BL/6J mouse brain. Neuroimage 37, 683–693.

Badea, A., Nicholls, P.J., Johnson, G.A., Wetsel, W.C., 2007b. Neuroanatomical phenotypes in the reeler mouse. Neuroimage 34, 1363–1374.

Barmpoutis, A., Jian, B., Vemuri, B.C., 2009. Adaptive kernels for multi-fiber reconstruction. Inf Process Med Imaging 21, 338–349.

Basser, P.J., 1995. Inferring microstructural features and the physiological state of tissues from diffusion-weighted images. NMR Biomed 8, 333–344.

Basser, P.J., 2002. Relationships between diffusion tensor and q-space MRI. Magn Reson Med 47, 392–397.

Basser, P.J., Pajevic, S., Pierpaoli, C., Duda, J., Aldroubi, A., 2000. In vivo fiber tractography using DT-MRI data. Magn Reson Med 44, 625–632.

Basser, P.J., Pierpaoli, C., 1996. Microstructural and physiological features of tissues elucidated by quantitative-diffusion-tensor MRI. J Magn Reson B 111, 209–219.

Berman, J.I., Berger, M.S., Mukherjee, P., Henry, R.G., 2004. Diffusion-tensor imaging-guided tracking of fibers of the pyramidal tract combined with intraoperative cortical stimulation mapping in patients with gliomas. J. Neurosurg. 101, 66–72.

Bockhorst, K.H., Narayana, P.A., Liu, R., Ahobila-Vijjula, P., Ramu, J., Kamel, M., Wosik, J., Bockhorst, T., Hahn, K., Hasan, K.M., Perez-Polo, J.R., 2008. Early postnatal development of rat brain: in vivo diffusion tensor imaging. J Neurosci Res 86, 1520–1528.

Bonnier, C., Mesples, B., Gressens, P., 2004. Animal models of shaken baby syndrome: revisiting the pathophysiology of this devastating injury. Pediatr Rehabil 7, 165–171.

Boss, B.D., Turlejski, K., Stanfield, B.B., Cowan, W.M., 1987. On the numbers of neurons in fields CA1 and CA3 of the hippocampus of Sprague-Dawley and Wistar rats. Brain Res 406, 280–287.

Bota, M., Swanson, L.W., 2008. BAMS Neuroanatomical Ontology: Design and Implementation. Frontiers in Neuroinformatics 2, 2.

Bowden, D.M., Martin, R.F., 1995. NeuroNames Brain Hierarchy. Neuroimage 2, 63–83.

Bug, W.J., Ascoli, G.A., Grethe, J.S., Gupta, A., Fennema-Notestine, C., Laird, A.R., Larson, S.D., Rubin, D., Shepherd, G.M., Turner, J.A., Martone, M.E., 2008. The NIFSTD and BIRNLex Vocabularies: Building Comprehensive Ontologies for Neuroscience. Neuroinform 6, 175–194.

Calabrese, E., Badea, A., Watson, C., Johnson, G.A., 2013. A quantitative magnetic resonance histology atlas of postnatal rat brain development with regional estimates of growth and variability. Neuroimage 71C, 196–206.

Calabrese, E., Johnson, G.A., 2013. Diffusion tensor magnetic resonance histology reveals microstructural changes in the developing rat brain. Neuroimage 79, 329–339.

Calabrese, E., Johnson, G.A., Watson, C., 2012. An ontology-based segmentation scheme for tracking postnatal changes in the developing rodent brain with MRI. Neuroimage 67C.

Callaghan, P.T., Eccles, C.D., Xia, Y., 1988. NMR microscopy of dynamic

displacements: k-space and q-space imaging. J Phys E: Sci Instrum 21, 820–822.

Calvo, J., Boya, J., 1984. Postnatal evolution of the rat pineal gland: light microscopy. J Anat 138 (Pt 1), 45–53.

Catani, M., Bodi, I., Dell'Acqua, F., 2012. Comment on "The geometric structure of the brain fiber pathways". Science 337, 1605.

Chahboune, H., Ment, L.R., Stewart, W.B., Ma, X., Rothman, D.L., Hyder, F., 2007. Neurodevelopment of C57B/L6 mouse brain assessed by in vivo diffusion tensor imaging. NMR Biomed 20, 375–382.

Chanas-Sacre, G., Rogister, B., Moonen, G., Leprince, P., 2000. Radial glia phenotype: origin, regulation, and transdifferentiation. J Neurosci Res 61, 357–363.

Charles River Wistar Rat Page, 2013. Charles River Wistar Rat Page. Charles River Laboratories, Inc. URL http://www.criver.com/FR-FR/PRODSERV/BYTYPE/RESMODOVER/RESMOD/Pages/WistarRat.aspx

Chuang, N., Mori, S., Yamamoto, A., Jiang, H., Ye, X., Xu, X., Richards, L.J., Nathans, J., Miller, M.I., Toga, A.W., Sidman, R.L., Zhang, J., 2011. An MRI-based atlas and database of the developing mouse brain. Neuroimage 54, 80–89.

Clancy, B., Finlay, B.L., Darlington, R.B., Anand, K.J.S., 2007. Extrapolating brain development from experimental species to humans. Neurotoxicology 28, 931–937.

Courchesne, E., Karns, C.M., Davis, H.R., Ziccardi, R., Carper, R.A., Tigue, Z.D., Chisum, H.J., Moses, P., Pierce, K., Lord, C., Lincoln, A.J., Pizzo, S., Schreibman, L., Haas, R.H., Akshoomoff, N.A., Courchesne, R.Y., 2001. Unusual brain growth patterns in early life in patients with autistic disorder: an MRI study. Neurology 57, 245–254.

Croxson, P.L., 2005. Quantitative Investigation of Connections of the Prefrontal Cortex in the Human and Macaque using Probabilistic Diffusion Tractography. J Neurosci 25, 8854–8866.

Delnomdedieu, M., Hedlund, L.W., Johnson, G.A., Maronpot, R.R., 1996. Magnetic Resonance Microscopy-A New Tool for the Toxicologic Pathologist. Toxicol Pathol 24, 36–44.

Descoteaux, M., Angelino, E., Fitzgibbons, S., Deriche, R., 2007. Regularized, fast, and robust analytical Q-ball imaging. Magn Reson Med 58, 497–510.

Dong, H.W., 2008. The Allen reference atlas: A digital color brain atlas of the C57Bl/6J male mouse. John Wiley & Sons Inc.

Edelstein, W.A., Glover, G.H., Hardy, C.J., Redington, R.W., 1986. The intrinsic signal-to-noise ratio in NMR imaging. Magn Reson Med 3, 604–618.

Edlow, B.L., Takahashi, E., Wu, O., Benner, T., Dai, G., Bu, L., Grant, P.E., Greer, D.M., Greenberg, S.M., Kinney, H.C., Folkerth, R.D., 2012. Neuroanatomic connectivity of the human ascending arousal system critical to consciousness and its disorders. J Neuropathol Exp Neurol 71, 531–546.

Farrell, J.A.D., Landman, B.A., Jones, C.K., Smith, S.A., Prince, J.L., van Zijl, P.C.M., Mori, S., 2007. Effects of signal-to-noise ratio on the accuracy and reproducibility of diffusion tensor imaging-derived fractional anisotropy, mean diffusivity, and principal eigenvector measurements at 1.5 T. J Magn Reson Imaging 26, 756–767.

Field, E.J., Hughes, D., Raine, C.S., 1969. Electron microscopic observations on the development of myelin in cultures of neonatal rat cerebellum. J Neurol Sci 8, 49–60.

Foran, D.R., Peterson, A.C., 1992. Myelin acquisition in the central nervous system of the mouse revealed by an MBP-Lac Z transgene. J Neurosci 12, 4890–4897.

Ford, A.A., Colon-Perez, L., Triplett, W.T., Gullett, J.M., Mareci, T.H., Fitzgerald, D.B., 2013. Imaging white matter in human brainstem. Front Hum Neurosci 7, 400.

Frederiksen, K., McKay, R.D., 1988. Proliferation and differentiation of rat neuroepithelial precursor cells in vivo. J Neurosci 8, 1144–1151.

Giberson, R.T., Demaree, R.S., 1999. Microwave processing techniques for electron microscopy: a four-hour protocol. Methods Mol Biol 117, 145–158.

Giedd, J.N., Rapoport, J.L., 2010. Structural MRI of pediatric brain development: what have we learned and where are we going? Neuron 67, 728–734.

Giuliani, N.R., Calhoun, V.D., Pearlson, G.D., Francis, A., Buchanan, R.W., 2005. Voxel-based morphometry versus region of interest: a comparison of two methods for analyzing gray matter differences in schizophrenia. Schizophr Res 74, 135–147.

Golay, X., Jiang, H., van Zijl, P.C.M., Mori, S., 2002. High-resolution isotropic 3D diffusion tensor imaging of the human brain. Magn Reson Med 47, 837–843.

Guilfoyle, D.N., Helpern, J.A., Lim, K.O., 2003. Diffusion tensor imaging in fixed

brain tissue at 7.0 T. NMR Biomed 16, 77–81.

Herculano-Houzel, S., 2009. The human brain in numbers: a linearly scaled-up primate brain. Front Hum Neurosci 3, 31.

Hess, C.P., Mukherjee, P., Han, E.T., Xu, D., Vigneron, D.B., 2006. Q-ball reconstruction of multimodal fiber orientations using the spherical harmonic basis. Magn Reson Med 56, 104–117.

Hines, M., Allen, L.S., Gorski, R.A., 1992. Sex differences in subregions of the medial nucleus of the amygdala and the bed nucleus of the stria terminalis of the rat. Brain Res 579, 321–326.

Honey, C.J., Sporns, O., Cammoun, L., Gigandet, X., Thiran, J.P., Meuli, R., Hagmann, P., 2009. Predicting human resting-state functional connectivity from structural connectivity. Proc Natl Acad Sci USA 106, 2035–2040.

Hoult, D.I., Lauterbur, P.C., 1979. The sensitivity of the zeugmatographic experiment involving human samples. Journal of Magnetic Resonance (1969) 34, 425–433.

Hoult, D.I., Richards, R.E., 1976. The signal-to-noise ratio of the nuclear magnetic resonance experiment. J Magn Reson 24, 71–85.

Jahanshad, N., Zhan, L., Bernstein, M.A., Borowski, B.J., Jack, C.R., Toga, A.W., Thompson, P.M., 2010. Diffusion tensor imaging in seven minutes: determining trade-offs between spatial and directional resolution 1161–1164.

Jailer, J.W., 1950. The maturation of the pituitary-adrenal axis in the newborn rat. Endocrinology 46, 420–425.

Jeong, E.-K., Kim, S.-E., Parker, D.L., 2003. High-resolution diffusion-weighted 3D MRI, using diffusion-weighted driven-equilibrium (DW-DE) and multishot segmented 3D-SSFP without navigator echoes. Magn Reson Med 50, 821–829.

Jeurissen, B., Leemans, A., Tournier, J.-D., Jones, D.K., Sijbers, J., 2013. Investigating the prevalence of complex fiber configurations in white matter tissue with diffusion magnetic resonance imaging. Hum Brain Mapp 34, 2747–2766.

Jiang, Y., Johnson, G.A., 2011. Microscopic diffusion tensor atlas of the mouse brain. Neuroimage 56, 1235–1243.

Johnson, G.A., Ali-Sharief, A., Badea, A., Brandenburg, J., Cofer, G., Fubara, B., Gewalt, S., Hedlund, L.W., Upchurch, L., 2007. High-throughput morphologic phenotyping of the mouse brain with magnetic resonance histology.

Neuroimage 37, 82–89.

Johnson, G.A., Badea, A., Brandenburg, J., Cofer, G., Fubara, B., Liu, S., Nissanov, J., 2010. Waxholm space: an image-based reference for coordinating mouse brain research. Neuroimage 53, 365–372.

Johnson, G.A., Benveniste, H., Black, R.D., Hedlund, L.W., Maronpot, R.R., Smith, B.R., 1993. Histology by magnetic resonance microscopy. Magn Reson Q 9, 1–30.

Johnson, G.A., Calabrese, E., Badea, A., Paxinos, G., Watson, C., 2012. A multidimensional magnetic resonance histology atlas of the Wistar rat brain. Neuroimage 62, 1848–1856.

Johnson, G.A., Cofer, G.P., Fubara, B., Gewalt, S.L., Hedlund, L.W., Maronpot, R.R., 2002a. Magnetic resonance histology for morphologic phenotyping. J Magn Reson Imaging 16, 423–429.

Johnson, G.A., Cofer, G.P., Gewalt, S.L., Hedlund, L.W., 2002b. Morphologic phenotyping with MR microscopy: the visible mouse. Radiology 222, 789–793.

Jolicoeur, P., Cabana, T., Ducharme, G., 1992. A four-parameter generalization of the Gompertz curve suitable for somatic growth. Growth Dev Aging 56, 69–74.

Jones, D.K., 2003. Determining and visualizing uncertainty in estimates of fiber orientation from diffusion tensor MRI. Magn Reson Med 49, 7–12.

Jones, D.K., 2004. The effect of gradient sampling schemes on measures derived from diffusion tensor MRI: a Monte Carlo study. Magn Reson Med 51, 807–815.

Kamali, A., Kramer, L.A., Butler, I.J., Hasan, K.M., 2009. Diffusion tensor tractography of the somatosensory system in the human brainstem: initial findings using high isotropic spatial resolution at 3.0 T. Eur Radiol 19, 1480–1488.

Kelly, P.H., Seviour, P.W., Iversen, S.D., 1975. Amphetamine and apomorphine responses in the rat following 6-OHDA lesions of the nucleus accumbens septi and corpus striatum. Brain Res 94, 507–522.

Kim, M., Ronen, I., Ugurbil, K., Kim, D.-S., 2006. Spatial resolution dependence of DTI tractography in human occipito-callosal region. Neuroimage 32, 1243–1249.

Knickmeyer, R.C., Gouttard, S., Kang, C., Evans, D., Wilber, K., Smith, J.K.,

Hamer, R.M., Lin, W., Gerig, G., Gilmore, J.H., 2008. A structural MRI study of human brain development from birth to 2 years. J Neurosci 28, 12176–12182.

Kochunov, P., Lancaster, J.L., Thompson, P., Woods, R., Mazziotta, J., Hardies, J., Fox, P., 2001. Regional spatial normalization: toward an optimal target. J Comput Assist Tomogr 25, 805–816.

Kovacevic, N., Henderson, J.T., Chan, E., Lifshitz, N., Bishop, J., Evans, A.C., Henkelman, R.M., Chen, X.J., 2005. A three-dimensional MRI atlas of the mouse brain with estimates of the average and variability. Cereb Cortex 15, 639–645.

Larvaron, P., Boespflug-Tanguy, O., Renou, J.-P., Bonny, J.-M., 2007. In vivo analysis of the post-natal development of normal mouse brain by DTI. NMR Biomed 20, 413–421.

Lauterbur, P.C., 1973. Image Formation by Induced Local Interactions: Examples Employing Nuclear Magnetic Resonance. Nature 242, 190–191.

Lazar, M., Alexander, A.L., 2003. An error analysis of white matter tractography methods: synthetic diffusion tensor field simulations. Neuroimage 20, 1140–1153.

Lebel, C., Benner, T., Beaulieu, C., 2012. Six is enough? Comparison of diffusion parameters measured using six or more diffusion-encoding gradient directions with deterministic tractography. Magn Reson Med 68, 474–483.

Lo, C.-Y., Wang, P.-N., Chou, K.-H., Wang, J., He, Y., Lin, C.-P., 2010. Diffusion tensor tractography reveals abnormal topological organization in structural cortical networks in Alzheimer's disease. J Neurosci 30, 16876–16885.

Luse, S.A., 1956. Formation of myelin in the central nervous system of mice and rats, as studied with the electron microscope. J Biophys Biochem Cytol 2, 777–784.

Ma, Y., Hof, P.R., Grant, S.C., Blackband, S.J., Bennett, R., Slatest, L., McGuigan, M.D., Benveniste, H., 2005. A three-dimensional digital atlas database of the adult C57BL/6J mouse brain by magnetic resonance microscopy. Neuroscience 135, 1203–1215.

Marín-Padilla, M., 1996. Developmental neuropathology and impact of perinatal brain damage. I: Hemorrhagic lesions of neocortex. J Neuropathol Exp Neurol 55, 758–773.

McNab, J.A., Edlow, B.L., Witzel, T., Huang, S.Y., Bhat, H., Heberlein, K.,

Feiweier, T., Liu, K., Keil, B., Cohen-Adad, J., Tisdall, M.D., Folkerth, R.D., Kinney, H.C., Wald, L.L., 2013. The Human Connectome Project and beyond: Initial applications of 300mT/m gradients. Neuroimage 80, 234–245.

Mehler, C., Warnke, A., 2002. Structural brain abnormalities specific to childhood-onset schizophrenia identified by neuroimaging techniques. J Neural Transm 109, 219–234.

Mori, S., Crain, B.J., Chacko, V.P., van Zijl, P. C., 1999. Three-dimensional tracking of axonal projections in the brain by magnetic resonance imaging. Ann Neurol 45, 265–269.

Mori, S., Itoh, R., Zhang, J., Kaufmann, W.E., van Zijl, P. C., Solaiyappan, M., Yarowsky, P., 2001. Diffusion tensor imaging of the developing mouse brain. Magn Reson Med 46, 18–23.

Moss, M.L., 1954. Growth of the calvaria in the rat; the determination of osseous morphology. Am J Anat 94, 333–361.

Mukherjee, P., Berman, J.I., Chung, S.W., Hess, C.P., Henry, R.G., 2008. Diffusion tensor MR imaging and fiber tractography: theoretic underpinnings. AJNR Am J Neuroradiol 29, 632–641.

Mukherjee, P., McKinstry, R.C., 2006. Diffusion Tensor Imaging and Tractography of Human Brain Development. Neuroimaging Clinics of North America 16, 19–43.

Nagy, Z., Westerberg, H., Klingberg, T., 2004. Maturation of white matter is associated with the development of cognitive functions during childhood. J Cogn Neurosci 16, 1227–1233.

Nie, B., Chen, K., Zhao, S., Liu, J., Gu, X., Yao, Q., Hui, J., Zhang, Z., Teng, G., Zhao, C., Shan, B., 2012. A rat brain MRI template with digital stereotaxic atlas of fine anatomical delineations in paxinos space and its automated application in voxel-wise analysis. Hum Brain Mapp.

Noctor, S.C., Martínez-Cerdeño, V., Ivic, L., Kriegstein, A.R., 2004. Cortical neurons arise in symmetric and asymmetric division zones and migrate through specific phases. Nat Neurosci 7, 136–144.

O'Leary-Moore, S.K., Parnell, S.E., Lipinski, R.J., Sulik, K.K., 2011. Magnetic resonance-based imaging in animal models of fetal alcohol spectrum disorder. Neuropsychol Rev 21, 167–185.

Parker, G.J.M., Stephan, K.E., Barker, G.J., Rowe, J.B., MacManus, D.G., Wheeler-Kingshott, C.A.M., Ciccarelli, O., Passingham, R.E., Spinks, R.L.,

Lemon, R.N., Turner, R., 2002. Initial demonstration of in vivo tracing of axonal projections in the macaque brain and comparison with the human brain using diffusion tensor imaging and fast marching tractography. Neuroimage 15, 797–809.

Paxinos, G., Huang, X.F., 1995. Atlas of the Human Brainstem. Academic Press.

Paxinos, G., Watson, C., 2007. The Rat Brain in Stereotaxic Coordinates, 6 ed. Elsevier Academic Press, San Diego.

Perlmutter, J.S., Mink, J.W., 2006. Deep brain stimulation. Annu Rev Neurosci 29, 229–257.

Petiet, A.E., Kaufman, M.H., Goddeeris, M.M., Brandenburg, J., Elmore, S.A., Johnson, G.A., 2008. High-resolution magnetic resonance histology of the embryonic and neonatal mouse: a 4D atlas and morphologic database. Proc Natl Acad Sci USA 105, 12331–12336.

Prats-Galino, A., Soria, G., de Notaris, M., Puig, J., Pedraza, S., 2012. Functional anatomy of subcortical circuits issuing from or integrating at the human brainstem. Clin Neurophysiol 123, 4–12.

Puelles, E., Martinez-de-la-Torre, M., Watson, C., Puelles, L., 2012a. Midbrain, in: Watson, C., Paxinos, G., Puelles, L. (Eds.), The Mouse Nervous System. Elsevier Academic Press, San Diego, pp. 337–359.

Puelles, L., Martinez-de-la-Torre, M., Bardet, S., Rubenstein, J.L.R., 2012b. Hypothalamus, in: Watson, C., Paxinos, G., Puelles, L. (Eds.), The Mouse Nervous System. Elsevier Academic Press, pp. 221–312.

Puelles, L., Martinez-de-la-Torre, M., Ferran, J.-L., Watson, C., 2012c. Diencephalon, in: Watson, C., Paxinos, G., Puelles, L. (Eds.), The Mouse Nervous System. Elsevier Academic Press, San Diego, pp. 313–336.

Puelles, L., Martinez-de-la-Torre, M., Paxinos, G., Watson, C., Martinez, S., 2007. The Chick Brain in Stereotaxic Coordinates: An Atlas featuring Neuromeric Subdivisions and Mammalian Homologies. Elsevier Academic Press, San Diego.

Puelles, L., Rubenstein, J.L.R., 2003. Forebrain gene expression domains and the evolving prosomeric model. Trends Neurosci 26, 469–476.

Rakic, P., 1972. Mode of cell migration to the superficial layers of fetal monkey neocortex. J Comp Neurol 145, 61–83.

Ramachandra, R., Subramanian, T., 2011. Atlas of the Neonatal Rat Brain. CRC Press.

Richards, K., Watson, C., Buckley, R.F., Kurniawan, N.D., Yang, Z., Keller, M.D., Beare, R., Bartlett, P.F., Egan, G.F., Galloway, G.J., Paxinos, G., Petrou, S., Reutens, D.C., 2011. Segmentation of the mouse hippocampal formation in magnetic resonance images. Neuroimage 58, 732–740.

Schmahmann, J.D., Pandya, D., 2009. Fiber Pathways of the Brain. Oxford University Press, New York.

Schmahmann, J.D., Pandya, D.N., Wang, R., Dai, G., D'Arceuil, H.E., de Crespigny, A.J., Wedeen, V.J., 2007. Association fibre pathways of the brain: parallel observations from diffusion spectrum imaging and autoradiography. Brain 130, 630–653.

Schwarz, A.J., Danckaert, A., Reese, T., Gozzi, A., Paxinos, G., Watson, C., Merlo-Pich, E.V., Bifone, A., 2006. A stereotaxic MRI template set for the rat brain with tissue class distribution maps and co-registered anatomical atlas: application to pharmacological MRI. Neuroimage 32, 538–550.

Sherwood, N., Timiras, P., 1970. A Stereotaxic Atlas of the Developing Rat Brain. University of California Press.

Silbert, L.C., Quinn, J.F., Moore, M.M., Corbridge, E., Ball, M.J., Murdoch, G., Sexton, G., Kaye, J.A., 2003. Changes in premorbid brain volume predict Alzheimer's disease pathology. Neurology 61, 487–492.

Simpson, K.L., Weaver, K.J., de Villers-Sidani, E., Lu, J.Y.-F., Cai, Z., Pang, Y., Rodriguez-Porcel, F., Paul, I.A., Merzenich, M., Lin, R.C.S., 2011. Perinatal antidepressant exposure alters cortical network function in rodents. Proc Natl Acad Sci USA 108, 18465–18470.

Sizonenko, S.V., Camm, E.J., Garbow, J.R., Maier, S.E., Inder, T.E., Williams, C.E., Neil, J.J., Huppi, P.S., 2007. Developmental changes and injury induced disruption of the radial organization of the cortex in the immature rat brain revealed by in vivo diffusion tensor MRI. Cereb Cortex 17, 2609–2617.

Skudlarski, P., Jagannathan, K., Anderson, K., Stevens, M.C., Calhoun, V.D., Skudlarska, B.A., Pearlson, G., 2010. Brain connectivity is not only lower but different in schizophrenia: a combined anatomical and functional approach. Biol. Psychiatry 68, 61–69.

Smith, S.M., Jenkinson, M., Johansen-Berg, H., Rueckert, D., Nichols, T.E., Mackay, C.E., Watkins, K.E., Ciccarelli, O., Cader, M.Z., Matthews, P.M., Behrens, T.E.J., 2006. Tract-based spatial statistics: voxelwise analysis of multi-subject diffusion data. Neuroimage 31, 1487–1505.

Soria, G., de Notaris, M., Tudela, R., Blasco, G., Puig, J., Planas, A.M., Pedraza,

S., Prats-Galino, A., 2011. Improved assessment of ex vivo brainstem neuroanatomy with high-resolution MRI and DTI at 7 Tesla. Anat Rec (Hoboken) 294, 1035–1044.

Sporns, O., Tononi, G., Kötter, R., 2005. The human connectome: A structural description of the human brain. PLoS Comput Biol 1, e42.

Stejskal, E.O., Tanner, J.E., 1965. Spin Diffusion Measurements: Spin Echoes in the Presence of a Time-Dependent Field Gradient. J Chem Phys 42, 288–292.

Sturm, V., Lenartz, D., Koulousakis, A., Treuer, H., Herholz, K., Klein, J.C., Klosterkötter, J., 2003. The nucleus accumbens: a target for deep brain stimulation in obsessive-compulsive- and anxiety-disorders. J Chem Neuroanat 26, 293–299.

Sun, S.-W., Liang, H.-F., Xie, M., Oyoyo, U., Lee, A., 2009. Fixation, not death, reduces sensitivity of DTI in detecting optic nerve damage. Neuroimage 44, 611–619.

Sun, S.-W., Neil, J.J., Liang, H.-F., He, Y.Y., Schmidt, R.E., Hsu, C.Y., Song, S.-K., 2005. Formalin fixation alters water diffusion coefficient magnitude but not anisotropy in infarcted brain. Magn Reson Med 53, 1447–1451.

Sundaram, S.K., Kumar, A., Makki, M.I., Behen, M.E., Chugani, H.T., Chugani, D.C., 2008. Diffusion tensor imaging of frontal lobe in autism spectrum disorder. Cereb Cortex 18, 2659–2665.

Tiemeier, H., Lenroot, R.K., Greenstein, D.K., Tran, L., Pierson, R., Giedd, J.N., 2010. Cerebellum development during childhood and adolescence: a longitudinal morphometric MRI study. Neuroimage 49, 63–70.

Toga, A.W., Thompson, P.M., Sowell, E.R., 2006. Mapping brain maturation. Trends Neurosci 29, 148–159.

Tuch, D.S., 2004. Q-ball imaging. Magn Reson Med 52, 1358–1372.

Tuch, D.S., Reese, T.G., Wiegell, M.R., Makris, N., Belliveau, J.W., Wedeen, V.J., 2002. High angular resolution diffusion imaging reveals intravoxel white matter fiber heterogeneity. Magn Reson Med 48, 577–582.

Tuch, D.S., Reese, T.G., Wiegell, M.R., Wedeen, V.J., 2003. Diffusion MRI of complex neural architecture. Neuron 40, 885–895.

Veraart, J., Leergaard, T.B., Antonsen, B.T., Van Hecke, W., Blockx, I., Jeurissen, B., Jiang, Y., Van der Linden, A., Johnson, G.A., Verhoye, M., Sijbers, J., 2011. Population-averaged diffusion tensor imaging atlas of the

Sprague Dawley rat brain. Neuroimage 58, 975–983.

Verma, R., Mori, S., Shen, D., Yarowsky, P., Zhang, J., Davatzikos, C., 2005. Spatiotemporal maturation patterns of murine brain quantified by diffusion tensor MRI and deformation-based morphometry. Proc Natl Acad Sci USA 102, 6978–6983.

Walker, D.L., Toufexis, D.J., Davis, M., 2003. Role of the bed nucleus of the stria terminalis versus the amygdala in fear, stress, and anxiety. Eur J Pharmacol 463, 199–216.

Wang, S., Wu, E.X., Cai, K., Lau, H.-F., Cheung, P.-T., Khong, P.-L., 2009. Mild hypoxic-ischemic injury in the neonatal rat brain: longitudinal evaluation of white matter using diffusion tensor MR imaging. American Journal of Neuroradiology 30, 1907–1913.

Watson, C., 2012. Hindbrain, in: Watson, C., Paxinos, G., Puelles, L. (Eds.), The Mouse Nervous System. Elsevier Academic Press, San Diego, pp. 397–422.

Watson, C., Paxinos, G., Puelles, L., 2012. The Mouse Nervous System. Academic Press, San Diego.

Wedeen, V.J., Hagmann, P., Tseng, W.-Y.I., Reese, T.G., Weisskoff, R.M., 2005. Mapping complex tissue architecture with diffusion spectrum magnetic resonance imaging. Magn Reson Med 54, 1377–1386.

Wedeen, V.J., Rosene, D.L., Wang, R., Dai, G., Mortazavi, F., Hagmann, P., Kaas, J.H., Tseng, W.-Y.I., 2012. The geometric structure of the brain fiber pathways. Science 335, 1628–1634.

White, J.J., Sillitoe, R.V., 2012. Development of the cerebellum: from gene expression patterns to circuit maps. WIREs Dev Biol.

Wise, S.P., Jones, E.G., 1976. The organization and postnatal development of the commissural projection of the rat somatic sensory cortex. J Comp Neurol 168, 313–343.

Yamamoto, A., Miki, Y., Urayama, S., Fushimi, Y., Okada, T., Hanakawa, T., Fukuyama, H., Togashi, K., 2007. Diffusion tensor fiber tractography of the optic radiation: analysis with 6-, 12-, 40-, and 81-directional motion-probing gradients, a preliminary study. AJNR Am J Neuroradiol 28, 92–96.

Yu, C.S., Li, K.C., Xuan, Y., Ji, X.M., Qin, W., 2005. Diffusion tensor tractography in patients with cerebral tumors: a helpful technique for neurosurgical planning and postoperative assessment. Eur J Radiol 56, 197–204.

Zhan, L., Chiang, M.C., Barysheva, M., Toga, A.W., de Zubicaray, G.I., Meredith,

M., Wright, M.J., Thompson, P.M., 2008. How Many Gradients are Sufficient in High-Angular Resolution Diffusion Imaging (HARDI)? 13th Annual Meeting of the Organization for Human Brain Mapping (OHBM).

Zhan, L., Franc, D., Patel, V., Jahanshad, N., Jin, Y., Mueller, B.A., Bernstein, M.A., Borowski, B.J., Jack, C.R., Toga, A.W., Lim, K.O., Thompson, P.M., 2012a. HOW DO SPATIAL AND ANGULAR RESOLUTION AFFECT BRAIN CONNECTIVITY MAPS FROM DIFFUSION MRI? Proc IEEE Int Symp Biomed Imaging 1–6.

Zhan, L., Jahanshad, N., Ennis, D.B., Jin, Y., Bernstein, M.A., Borowski, B.J., Jack, C.R., Toga, A.W., Leow, A.D., Thompson, P.M., 2012b. Angular versus spatial resolution trade-offs for diffusion imaging under time constraints. Hum Brain Mapp.

Zhan, L., Leow, A.D., Jahanshad, N., Chiang, M.-C., Barysheva, M., Lee, A.D., Toga, A.W., McMahon, K.L., de Zubicaray, G.I., Wright, M.J., Thompson, P.M., 2010. How does angular resolution affect diffusion imaging measures? Neuroimage 49, 1357–1371.

Zhang, J., Miller, M.I., Plachez, C., Richards, L.J., Yarowsky, P., van Zijl, P., Mori, S., 2005. Mapping postnatal mouse brain development with diffusion tensor microimaging. Neuroimage 26, 1042–1051.

Zhang, J., Richards, L.J., Miller, M.I., Yarowsky, P., van Zijl, P., Mori, S., 2006. Characterization of mouse brain and its development using diffusion tensor imaging and computational techniques. Conf Proc IEEE Eng Med Biol Soc 1, 2252–2255.

Biography

Evan Calabrese was born on April 23, 1986 in Cambridge, Massachusetts to his father Ronald Calabrese and mother Christine Cozzens. Shortly after birth, the Cozzens/Calabrese family moved to Atlanta, Georgia, where Ronald accepted a position as professor of biology at Emory University, and Christine accepted a position as professor of English and Agnes Scott University. Evan's education started at Paideia School, an independent K-12 private school in Atlanta. Evan Graduated from Paideia School in May of 2004 and started his baccalaureate education at Emory University in August of the same year. During his time at Emory, Evan completed the degree requirements for a Bachelor of Science degree in Biology, and a Bachelor of Arts degree in Spanish language. He received full tuition support from the Emory Courtesy Scholarship program and the state of Georgia's HOPE scholarship program. He made the Dean's List in seven of his eight semesters at Emory, and was accepted into the Phi Sigma Iota National Foreign Language Honor Society and Phi Beta Kappa in 2008. Evan received his Bachelor of Science degree with Highest Honors from the Emory University Department of Biology in May of 2008. Evan matriculated to the Duke University Medical Scientist Training Program in August of 2008, and began his graduate training in the Duke University Department of Biomedical Engineering in November of 2010.